STUDIES OF MAGNETIC FIELD INDUCED DOMAIN WALL DYNAMICS IN POLYCRYSTALLINE IRON AND IRON BASED ALLOYS USING MAGNETIC FORCE MICROSCOPY

By

ABUTHAHIR J

PHYS 02 2012 04 007

Indira Gandhi Centre for Atomic Research, Kalpakkam

A thesis submitted to the

Board of Studies in Physical Sciences

In partial fulfillment of requirements

for the Degree of

DOCTOR OF PHILOSOPHY

of

HOMI BHABHA NATIONAL INSTITUTE

April, 2018

Homi Bhabha National Institute

Recommendations of the Viva Voce Committee

As members of the Viva Voce Committee, we certify that we have read the dissertation prepared by J. Abuthahir entitled "**Studies of magnetic field induced domain wall dynamics in polycrystalline iron and iron based alloys using magnetic force microscopy**" and recommend that it may be accepted as fulfilling the thesis requirement for the award of Degree of Doctor of Philosophy.

Chairman - Dr. G. Amarendra	**Date:** Oct 17, 2018
Guide / Convener – Dr. Anish Kumar	**Date:** 17/10/18
Examiner – Dr. Jyoti Ranjan Mohanty	**Date:** 17/10/2018
Member 1 - Dr. B. Purna Chandra Rao For R. Dr. R. Rajaraman, Dean	**Date:** 17/10/18
Member 2- Dr. C. K. Mukhopadhyay	**Date:** 17/10/2018

Final approval and acceptance of this thesis is contingent upon the candidate's submission of the final copies of the thesis to HBNI.

I/We hereby certify that I/we have read this thesis prepared under my/our direction and recommend that it may be accepted as fulfilling the thesis requirement.

Date: 17/10/18

Place: Kalpakkam

Guide

STATEMENT BY AUTHOR

This dissertation has been submitted in partial fulfillment of requirements for an advanced degree at Homi Bhabha National Institute (HBNI) and is deposited in the Library to be made available to borrowers under rules of the HBNI.

Brief quotations from this dissertation are allowable without special permission, provided that accurate acknowledgement of source is made. Requests for permission for extended quotation from or reproduction of this manuscript in whole or in part may be granted by the Competent Authority of HBNI when in his or her judgment the proposed use of the material is in the interests of scholarship. In all other instances, however, permission must be obtained from the author.

Abuthahir J

DECLARATION

I, hereby declare that the investigation presented in the thesis has been carried out by me. The work is original and has not been submitted earlier as a whole or in part for a degree / diploma at this or any other Institution / University.

Abuthahir J

List of publications arising from the Thesis

Journals

1. Magnetic force microscopy studies in bulk polycrystalline iron
   J. Abuthahir and Anish Kumar
   Journal of Magnetism and Magnetic Materials 448 (2018) 107-116.

2. Influence of crystallographic orientation and applied magnetic field on domain structure in duplex stainless steel studied using magnetic force microscopy
   J. Abuthahir, Anish Kumar and Vani Shankar
   Materials Characterization (2018) 144: 368.

3. Magnetic force microscopy studies in cold worked 304 austenitic stainless steel
   J. Abuthahir and Anish Kumar
   J. Mater. Science (2018) Submitted.

Conference presentations

1. "Visualization of magnetic domain dynamics on surface of polycrystalline iron using magnetic force microscopy" (Oral Presentation)
   J. Abuthahir and Anish Kumar, *International Conference on Magnetic Materials and Applications*, ICMAGMA-2017, Feb 1-3 (2017). Hyderabad, India

2. "Visualization of magnetic domain dynamics in martensitic phase of cold worked AISI 304 stainless steel using magnetic force microscopy" (Oral Presentation), **J. Abuthahir** and Anish Kumar, *National Metallurgy Day and Annual Technical Meeting* of IIM, NMD-ATM'16, Nov 11-14 (2016). IIT-Kanpur, India.

3. "Visualization of magnetic domain motion through Monte Carlo simulation and magnetic force microscopy" (Poster Presentation)

   J. Abuthahir and Anish Kumar, *International conference on magnetic materials and Application*, ICMAGMA-2015, Dec 2-4 (2015), VIT, Vellore, India

Abuthahir J

DEDICATED TO

MY PARENTS

Jabarullah & Asarafunisha

&

MY MENTORS

DR. Anish Kumar

DR. S V M Satyanarayana

Acknowledgements

In the name of Allah, most gracious and most merciful. All the praise to Allah. I need to thank him throughout my life, for giving me this life with such great accomplishments.

I would like to express my deep sense of gratitude to my beloved supervisor Dr. Anish Kumar, Head, Ultrasonic Measurements Section, Non-Destructive Evaluation Division (NDED), Metallurgy and Materials Group (MMG), Indira Gandhi Centre for Atomic Research (IGCAR) for his guidance, constant support and for keeping faith in me for all this complete period of research. I am grateful to him for shaping my career and showing the path to flourish. I thank him for allowing me to learn by mistakes and for inspiring me to be a better version of myself.

I express my sincere gratitude to Dr. G. Amarendra, Director, MMG, IGCAR and Chairman of my doctoral committee, for his inspiration, encouragement and most importantly providing direction during the course of thesis work. I thank eminent members of the doctoral committee Dr. B.P.C. Rao and Dr. C. K. Mukhopadhyay for their regular appraisal, kind advice and suggestions to improve the quality of this work. I would like to extend my heartfelt thanks to the former directors of IGCAR, Shri S. C. Chetal, Dr. P. R. Vasudeva Rao and Dr. S. A. V. Satyamurthy, and the present director Dr. A. K. Bhaduri for permitting me to pursue research in this reputed centre. I am grateful to Dr. M. Saibaba for the wonderful hospitality during my stay at kalpakkam.

Special thanks to Dr. Vani Shankar for the SEM and EBSD measurements, Dr. Awadhesh Mani Tiwari and Dr. John Philip, for the SQUID and VSM measurements and also fruitful discussions.

I would like to express my whole-hearted thanks to Dr. M. Kalyan Phani, Mr. M. M. Narayanan, Mr. G. V. K. Kishore, Mr. G. M. S. K. Chaitanya, Dr. Samba Siva Rao, Mr. A. Viswanath and Mr. S. Ponseenivasan for their support and encouragement.

The strong co-operation and kind support of all the members of NDE Division are deeply acknowledged.

I thank my friends Thirukumaran, Balakrishnan, Sumana, Naveen, Balasundaram, Gopi, as well as my batch mates JRF 2012, for their encouragement and support. I would also thank other friends and juniors in JRF enclave for making my stay memorable, especially in the shuttle court.

I deeply express my heart-felt thanks to Dr. S V M Satyanarayana, Dr. G Rajasekaran, Dr. H. S. Mani, Dr. Naina Mohammed, Mr. Joseph Prabhakar and my friends in the Sunday class for their selfless service in teaching of physics. Thanks to my PG classmates in University of Madras and my colleagues in GCES for their support.

I take this opportunity to remember the care and affection of my family members who are the backbone for all my endeavors. My deepest sincere thanks to my lovable Asarafunisha (Amma), Jabarullah (Athaa) and my brothers Mansoor Ali, Askar Ali and Jawahar Ali for their unconditional love.

TABLE OF CONTENTS

Page No

LIST OF FIGURES

LIST OF TABLES

SYNOPSIS

The thesis focuses at studying the structure of magnetic domains and field induced domain wall dynamics on the surface of bulk polycrystalline iron and iron base alloy steels viz. duplex stainless steel (DSS) and cold worked AISI type 304 austenitic stainless steel (AUSS). Magnetic Force Microscopy (MFM) has been employed in imaging the magnetic domains in the three materials, which were selected in view of their varied microstructure such as volume fraction, size and shape of ferromagnetic phase. The magneto crystalline anisotropic effect on the domain structure is analyzed with the support of Electron Backscatter Diffraction (EBSD) study. The local micro-magnetization behaviour is studied in-situ by MFM in presence of in-plane external magnetic field in the range of ±2000 Oe.

In bulk polycrystalline iron, the effects of crystallographic orientation and external magnetic field on magnetic microstructure have been studied with the MFM technique. A distinct variation in magnetic domain structure is observed based on the crystallographic orientation of the grain surface normal with respect to the cube axis *i.e.* the easy axis of magnetization. With MFM studies in presence of in-plane external magnetic field, various micro-magnetization phenomena such as reversible and irreversible domain wall movements, expansion and contraction of domains, Barkhausen jump, bowing of a pinned domain wall and nucleation of a spike domain have been visualized. The respective changes in the magnetic microstructure are compared with the bulk magnetization obtained using vibrating sample magnetometer. Bowing of a domain wall, pinned at two points, upon application of magnetic field has been used to estimate the domain wall energy density. The MFM studies in presence of external field applied in two orthogonal directions

of the in-plane sample surface have been used to reveal the influence of the crystalline anisotropy on the local micro-magnetization.

In the DSS specimen, the MFM imaging could clearly differentiate ferrite phase (ferromagnetic) from the austenite phase (paramagnetic) due to the maze type magnetic domains present in the ferrite phase. The DSS contains equal proportions of ferrite and austenite phases. The ferrite phase exhibited presence of out of plane domain magnetization. The difference in the domain structure in different grains is analysed with the support of EBSD measurements. The MFM phase contrast and domain width are correlated with the orientation of surface normal with respect to the easy axis of magnetization (<100>). The influence of application of external magnetic field (±1600 Oe) on the domain structure is studied as a function of the grain orientation and the leakage field at the grain boundaries is analyzed in view of the mis-orientation between the grains. MFM imaging in presence of in-plane external magnetic field in the two orthogonal directions revealed the magnetocrystalline anisotropy influence in the magnetization phenomena.

In cold worked AUSS, magnetic domains in very fine martensitic (ferromagnetic) precipitates in an austenitic matrix have been studied by MFM. The martensite phases of thin lamellar and small dot shapes could be clearly identified due to the presence of magnetic domains. The average area fraction of the martensite phase estimated by MFM imaging at different locations over the sample is found to be in good agreement with that obtained by X-ray diffraction technique. Both in-plane and out-of-plane magnetized domains have been observed for the precipitates with the same crystallographic orientations indicating strong effect of size or the shape anisotropy. MFM imaging in presence of external field provided local observation of field induced domain wall dynamics in the fine ferromagnetic phases. The micro-magnetization loop of two oppositely rotated vortex

domains has also been studied. The study demonstrated that the shape anisotropy influences the magnetic domain structure in fine isolated ferromagnetic phases whereas the magnetocrystalline anisotropy governs the domain structure and its orientation in polycrystalline ferromagnetic materials with larger grains.

1 INTRODUCTION

1.1 BACKGROUND CONTEXT

Magnetism is one of the important fields of physics for fundamental research and industrial applications. Even though the utilization of permanent magnets has been known since olden days, the origin of ferromagnetism is complex and requires the knowledge of advanced physics involving quantum mechanics to understand such phenomenon. During the last century, tremendous improvements have been made in this field causing significant progress in the modern day technologies. Exploration of fundamental phenomena in magnetic nanostructures enables a remarkable development in data storage industry, particularly in the last few decades, that has had an immeasurable influence in our way of life.

The magnetic domain theory provides explanation for the presence of domain structure in a ferromagnetic material, which is the result of different energy contributions such as quantum exchange energy, magnetostatic energy, magneto anisotropy energy, magnetostriction energy and Zeeman energy. Essentially, the magnetic domain imaging techniques made it possible to access direct information about magnetization and anisotropy distributions as well as advance details about the micro-magnetization processes. Various techniques have been employed for the visualization of magnetic micro and nanostructures on the surface of ultra-thin films to the bulk materials. These techniques have their own advantages and limitations making them suitable for specific applications. A few of the frequently used techniques are magneto-optical Kerr microscopy, Bitter method, Scanning Electron Microscopy with Polarization Analysis

(SEMPA), Lorentz Transmission Electron Microscopy (LTEM) and Magnetic Force Microscopy (MFM). Figure 1.1 depicts the maximum lateral dimension of the imaging area and corresponding lateral resolution for various techniques mentioned above. Among these techniques, MFM is one of the most powerful tools for studying magnetic domains on the surface of a ferromagnetic material with a minimal requirement of surface preparation. It can detect magnetic stray fields from the surface using a magnetically coated very sharp tip of the radius of curvature of about 20-40 nm. Magnetic force microscope has lateral resolution of about a few tens of nanometers and it can perform in the ambient atmospheric conditions.

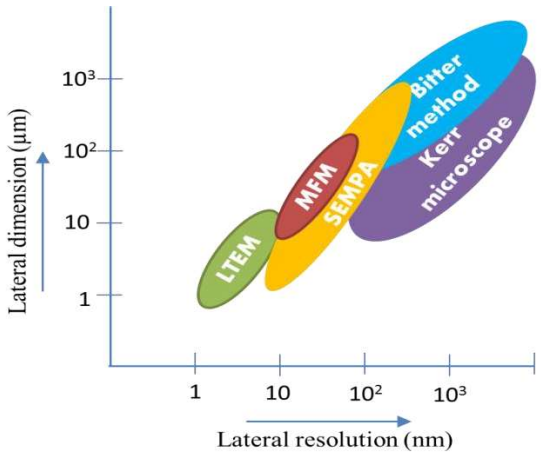

Figure 1.1: Comparison between different magnetic domain imaging techniques

Several studies have been reported on high resolution magnetic domain imaging in thin films and fabricated nanostructures. However, high resolution studies of magnetic domain structures in bulk polycrystalline samples are relatively less. Detailed characterization of magnetic microstructure in a bulk polycrystalline material can provide a better understanding of the micro-magnetization events, which is important for development of magnetic techniques for non-destructive characterization of the material. In the present thesis, the structure and field induced domain wall dynamics of magnetic domains in presence of in-plane magnetic field have been studied using high resolution

MFM technique in bulk polycrystalline materials having different sizes, shapes and volume fractions of magnetic phases.

1.2 OUTLINE OF THE THESIS

Chapter 1 discusses the background context of the work carried out in the thesis. A brief introduction is given for the basic understanding of magnetic domain and their imaging techniques.

Chapter 2 deals with the origin of magnetic domain structure in ferromagnetic materials and discusses the importance of studying the field induced magnetic domain wall dynamics at micro/nano scale. Visualization of magnetic domains with various techniques has been discussed. Introduction to MFM and its emergence as an advanced scanning probe microscopy technique for studies of magnetic domains have been presented. The last section deals with the background of the materials studied in the dissertation. Finally, motivation and objective of the thesis are given.

Chapter 3 deals with the experimental setup of MFM in presence of external magnetic field, used in the present study. The NOVA© software and associated features used for acquisition and analysis of MFM images are described. Optimization of experimental parameters, the details of the MFM cantilever used in the present work and magnetic stability of its tip are also described. The specimen preparation procedures for the materials used in the study and details of Electron Backscatter Diffraction (EBSD) measurement are also presented.

Chapter 4 presents the applicability of MFM in combination with EBSD technique to study the influence of crystallographic orientation on the magnetic domain structure and field induced domain wall dynamics on the surface of a polycrystalline iron specimen. Various micro-magnetization phenomena such as reversible and irreversible

domain wall movements, expansion and contraction of domains, Barkhausen jumps, bowing of a pinned domain wall and nucleation of a spike domain are visualized. The MFM studies in the presence of external field in two perpendicular directions are used to reveal the influence of the crystalline anisotropy on the local micro-magnetization.

Chapter 5 presents the investigation of local micro-magnetization behaviour in a duplex stainless steel (DSS) having almost equal fractions of ferrite and austenite phases. The MFM imaging clearly differentiates ferrite phases (ferromagnetic) from the austenite phases (paramagnetic) due to the maze type magnetic domains present in the ferrite phases. The magneto crystalline anisotropic effect on the domain structure is discussed with the support of EBSD measurements. The MFM phase contrast and domain width are correlated with the orientation of surface normal with respect to the easy axis of magnetization (<100>). The influence of external magnetic field application on the domain structure is studied as a function of the grain orientation and the leakage field at the grain boundaries is analyzed based on the mis-orientation between the grains.

Chapter 6 investigates magnetic domains and micromagnetic events in fine lamellae and dot precipitates of the strain induced martensite (SIM) phases of austenitic stainless steel (AUSS). The distribution of SIM phase could be studied due to the presence of magnetic domain structure in martensite. MFM study on the SIM phases in presence of external magnetic field has been used for understanding the micro-magnetization behaviour in very small ferromagnetic phases in a non-magnetic matrix. A comparison of magnetic characteristics of the materials of different types studied in the thesis is deliberated in the final part of the chapter.

Chapter 7 summarizes the results obtained, conclusions drawn and the scope for future work.

LITERATURE REVIEW 2

2.1 INTRODUCTION

This chapter deals with the origin of magnetic domains in the ferromagnetic materials and discusses the importance of studying field induced domain wall dynamics of the magnetic domain at micro/nano scale. Visualization of magnetic domains with various techniques has been discussed. Introduction to MFM and its emergence as an advanced scanning probe microscopy technique for the studies of magnetic domains has been presented. The last section deals with the background of the materials studied in the dissertation. Finally, motivation and objective of the thesis is given.

2.2 QUANTUM ORIGIN OF FERROMAGNETISM

The bulk magnetic behaviour of the material originates from the individual magnetic moment of atoms. The magnetic moment of an atom in the absence of a magnetic field consists of two contributions. The first is from orbital motion of the electron based on the Ampere's circulating currents.

$$\boldsymbol{m_l} = -\frac{e}{2m_e}\boldsymbol{l} \tag{2.1}$$

where, $\boldsymbol{m_l}$ is the magnetic moment due to orbital motion of an electron, e is the electron charge, $\boldsymbol{l}$ is the orbital angular momentum and m_e is the electron mass. The second contribution is from the intrinsic magnetic moment ($\boldsymbol{m_s}$) of the electron which is known as spin.

$$\boldsymbol{m_s} = -\frac{e}{m_e}\boldsymbol{S} \qquad (2.2)$$

where, $\boldsymbol{S}$ is the spin angular momentum. The orbital and spin magnetic moments are coupled together to produce the total magnetic moment of the atoms.

According to the Pauli's exclusion principle, two electrons cannot have same combination of the four quantum numbers such as $\boldsymbol{n}$, $\boldsymbol{l}$, $\boldsymbol{m_l}$ and $\boldsymbol{m_s}$. The energy states are admitted in the first three quantum numbers. The spin quantum number $\boldsymbol{m_s}$ can only take the values ±1/2 (spin up or down). Therefore, only two electrons can be filled in each energy states with opposite spin quantum number. If one individual electron is present in the energy state, then the overall magnetic moment is contributed by the spin magnetic moment of that electron. When two electrons occupy the same energy state but spins antiparallel to each other, the magnetic moment of one electron cancels out the other. On the other hand, if the atom contains unpaired spins, then there will be a net magnetic moment in the atom which results in magnetic properties of the elements.

The paramagnetic material consists of the atoms with uncompensated electron spins. In the absence of external magnetic field the magnetic moments of individual atoms are randomly oriented in paramagnetic materials (Fig. 2.1a) and with the magnetization process the atoms are aligned in the field direction. When the temperature is lowered to a specific value, the paramagnetic materials go through a phase transition to an ordered state. In that state, there is a local alignment within the atomic magnetic moment. The ordered state is known as 'ferromagnetic' in which atomic magnetic moments are aligned parallel to each other. The respective phase transition temperature of the ferro-para or para-ferro is known as Curie temperature [1, 2].

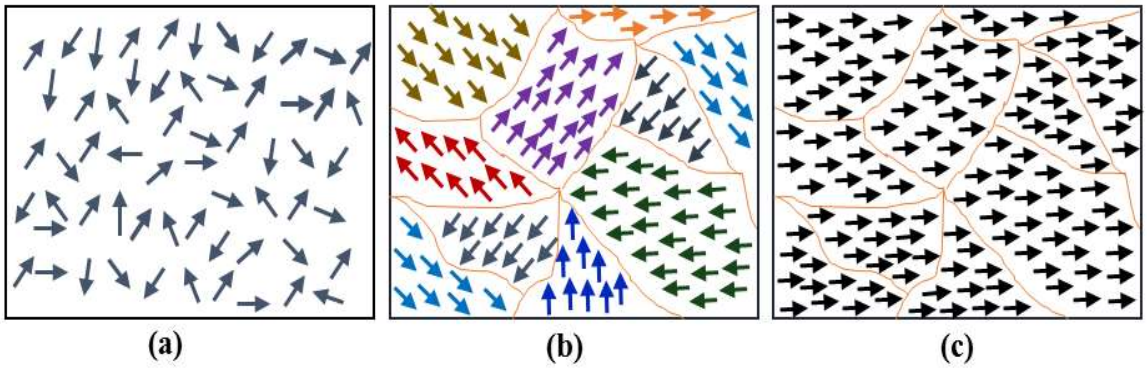

Figure 2.1: Schematic of magnetic structures: (a) paramagnetic, (b) and (c) are ferromagnetic material in demagnetized and uniformly magnetized states, respectively.

A complete ferromagnetic material is subdivided into regions, having different magnetization directions, known as magnetic domains (Fig 2.1b) [3, 4]. The well-known room temperature ferromagnetic materials are iron, cobalt and nickel. These materials play important roles in various magnetic applications and technologies [5, 6].

2.3 HISTORY OF MAGNETIC DOMAIN CONCEPT

In the beginning of twentieth century, the real understanding of magnetic phenomena came with the Langevin theory of paramagnetism [7]. He showed that elementary magnets in a material (analogous to the atoms and molecules as elementary particles of a matter) lead to weak magnetic phenomena only at room temperature and concluded that the strong magnetism arises due to some interaction between the elementary magnets. Further, Pierre Weiss in 1906 [8] stated his hypothesis of the molecular field which elaborated the interaction between the elementary magnets. He proposed that a ferromagnetic in the demagnetized state is divided into small regions of domains which are unidirectionally magnetized. However, the directions of magnetization of the various domains are different such that the specimen as a whole has no net magnetization. Within the framework of Weiss theory, ferromagnetic materials can be

spontaneously magnetized even without an external magnetic field. Conversely, this theory in itself did not provide an explanation for the fact of having a zero average magnetization state in most of the ferromagnetic materials. This difficulty was also overcome by Weiss, as he considered that the magnetization vector is only fixed in magnitude and its direction remains a variable. The demagnetized state of a ferromagnetic material like iron at room temperature (far below the ferromagnetic transition temperature) could be explained by considering that the magnetization vectors in different parts of the magnetic sample which are magnetized in opposite directions cancel each other. Weiss' famous theory was successful in explaining the general behaviour of the temperature dependence of saturation magnetization and the dependence of interaction strength on the Curie temperature. In this case, nature of the interaction field is a quantum mechanical exchange effect which was identified later by Heisenberg in 1927 [9]. It is worth mentioning that, at first, notion of ferromagnetic domains presented by Weiss remained without any experimental verification. Later, the first experimental confirmation of the magnetic domain concept was provided by Barkhausen in 1919, as a coincidence with the noise heard in a speaker when made audible by an amplifier [10]. From these results, Barkhausen revealed that the magnetization is often a discontinuous process (Barkhausen jumps). Analyzing the dynamics of Barkhausen jumps, Langmuir [11] concluded that such jumps could occur only by a spatially inhomogeneous process, such as by the propagation of a boundary between domains of opposite magnetization. This was confirmed with the experiments of Sixtus and Tonks [12, 13] who followed propagation of the domain boundary along the stressed wire by electronic means. In 1933, Bloch became interested in analyzing the transition region between domains magnetized in opposite directions and he explained that walls must have few hundreds of lattice constant of width due to the Heisenberg exchange effect [14]. At the same time, other

properties of magnetic domains were also studied such as anisotropy effect, magnetostriction and internal stress effect on the magnetic microstructure [15-18]. Meanwhile, Bitter [19] provided the first observation of magnetic domains in 1932. In 1935, Landau and Lifshitz [20] proposed the theory for the magnetostatic energy which causes the magnetic domain formation and explained that it happens due to global minimization of the energy. The major improvement in the experimental approach of magnetic domains provided convincing demonstration of the domain theory [21]. Kittel's review on magnetic domains and experiments served as a significant reference in the magnetic domains research [22-24]. The extensive background of the magnetic domains can be found in the book by Hubert and Schafer [25].

2.4 THEORY OF MAGNETIC DOMAIN STRUCTURE

2.4.1 Internal energies of magnetic domains

The magnetic domains in ferromagnetic material are a consequence of minimization of total energy of the system. The magnetic domain formation is occurring, based on the intrinsic magnetism to balance the following energy terms: exchange energy (E_{ex}), magnetostatic energy (E_{ms}), magnetocrystalline anisotropy energy (E_{aniso}), magnetostriction or magneto elastic energy (E_{me}) and domain wall energy (E_{wall}) [26]. The combined total energy is given by:

$$E_{tot} = E_{ex} + E_{ms} + E_{aniso} + E_{me} + E_{wall} \tag{2.3}$$

2.4.1.1 Exchange energy

The exchange energy is basically coming from the quantum mechanical effect which was identified by the Heisenberg in 1928 [9] as an exchange effect due to

overlapping wave function of neighbouring atoms. The exchange energy term can be described as follows:

$$E_{ex} = -\sum_{i,j} J_{i,j}\, \boldsymbol{S}_i . \boldsymbol{S}_j \qquad (2.4)$$

where, $J_{i,j}$ is the exchange constant, indices i, j refer to the position of the atoms in the lattice site and $\boldsymbol{S}_i$ is the spin angular momentum of the site i. If $J_{i,j} > 0$, the energy will be minimum which favors the spins alignment to be parallel to each other. Hence, complete alignment of all atomic moments in the specimen (magnetic saturation) is favoured by this term. The exchange interaction is short range, so the sum can be reduced to one over nearby atoms in the equation 2.4. For the simplified case, the value $J_{i,j}$ can be kept as a single constant and also $J_{i,j}$ has linear dependence with the Curie temperature [27].

The exchange energy form can be modified from discrete atom basics to the continuous magnetization $\mathbf{M}(\mathrm{r})$, then equation 2.4 is deliberated in the integral form like,

$$E_{ex} = \int_V \frac{A}{M_s^2} (\boldsymbol{\nabla M})^2 d^3 r \qquad (2.5)$$

where, M_s is the saturation magnetization and A is the stiffness constant or exchange constant. The value of A depends on the material's crystalline structure and it is also proportional to the integral exchange constant J. If the exchange energy term favours the complete alignment of the magnetic moment in the material, then the explanation is required for the demagnetized state.

2.4.1.2 Magnetostatic energy

Magnetostatic or stray field energy is the principle driving force for the formation of magnetic domains [20, 24]. When the magnetization field is applied on a material, an

internal opposite field termed as demagnetization field, is created. Its effect is to eliminate the emergence of stray field from the surface of the material. Magnetostatic energy is the energy associated with the existence of a demagnetizing field induced on the surface of a material caused by the free magnetic poles when the domain magnetization is directed out of the material [28]. It causes the shape-anisotropy effect. Magnetostatic energy (E_{ms}) arises from the interaction of the magnetization $\boldsymbol{M}$ and the magnetic field **H.**

$$E_{ms} = -\mu_0 \int \boldsymbol{H}.\partial \boldsymbol{M} \tag{2.6}$$

where, μ_0 is the permeability of the free space. At any external or internal surface of a uniformly magnetized specimen, there is a discontinuous change in the component of $\boldsymbol{M}$ normal to the surface, which can be envisioned as a source of `free poles'. A finite body has free poles on its outer surfaces, causing a demagnetizing field $\boldsymbol{H}_d$ antiparallel to magnetization vector $\boldsymbol{M}$. This field is given by:

$$\boldsymbol{H}_d = N_d \boldsymbol{M} \tag{2.7}$$

where N_d is the demagnetizing factor, which depends on the specimen geometry. In the absence of the any field, the E_{ms} depends only on $\boldsymbol{M}$ and N_d.

$$E_{ms} = \frac{\mu_0}{2} N_d {M_s}^2 \tag{2.8}$$

The minimum in magnetostatic energy occurs when the net magnetization is zero (closure domain structures). In domain structure, E_{ms} plays a vital role in subdivision of domains and produce a maximum possible finer domains to eliminate the stray field out of the surface [4].

2.4.1.3 Magnetocrystalline anisotropy energy

Magnetocrystalline anisotropy is the alignment of atomic magnetic moments along preferred axes of the crystal, known as easy axes of magnetization or magnetic easy

axes. On the other hand, magnetic hard directions are particularly unfavourable to the magnetization direction. The orbital moments are constrained in particular directions by the crystal lattice, so the crystal symmetry influences the behaviour of spin magnetic moments through this interaction. The energy required for the spins to align in that preferred direction is termed as anisotropy energy or magnetocrystalline anisotropy energy. The anisotropy energy per unit volume can be written as

$$E_{aniso} = K \,.\, f(\theta_1, \theta_2, \theta_3) \tag{2.9}$$

where, θ_1, θ_2 and θ_3 are the direction cosines of magnetization vector with respect to the lattice primitive vectors, the function f depends on the spatial symmetry of the lattice. The magnetic easy axes are well established for different crystal structures, such as; in iron with body center cubic (BCC) crystal structure, the anisotropy constant K is positive and the three distinct directions of cube edges $< 100 >$ are the easy magnetization directions. In nickel having face centered cubic (FCC) crystal structure; the magnetic easy axes are $< 111 >$ cube diagonals. Whereas, in cobalt having hexagonal closed pack (HCP) crystal structure, the hexagonal axis is the only magnetic easy axis. In NdFeB (hard magnet) having tetragonal crystal structure, the tetragonal axis is the only easy axis. The one easy axis crystals are referred to as uniaxial. The hard magnetic materials (rare earth metals) are hard to demagnetize due to the high magnetic anisotropy [29]. On the other hand low magnetic anisotropy materials are termed as soft magnetic material [30].

2.4.1.4 Magnetostriction or magnetoelastic energy

Magnetostriction is a property of ferromagnetic materials that causes them to change their shape or dimensions during the process of magnetization. It is a dimensional variant associated to the magnetic polarization [1]. It is the elastic energy associated with the deformation and stresses originating on the material. The magnetostriction value is positive for the specimens that elongates in the magnetization direction and negative for

the specimen that contract in the direction of magnetization. This additional energy comes as an inverse effect to the anisotropy and it is also referred to as the magnetoelastic energy. Magnetostriction depends on the magnetic history of the material and the thermo mechanical treatment to which it has been exposed [25].

2.4.1.5 Magnetic domain wall energy

The explicit region between two oppositely magnetized domains which is involved in rotation of the magnetic moments from one direction to the other direction of magnetization is known as 'domain wall'. The domain walls are characterized by the direction of the spin rotation axis with respect to the specimen surface. The typical two cases of domain walls are Bloch and Néel wall. In 1932, Bloch [14] studied about the domain walls in which the rotation of spins occurred along the perpendicular to the surface (Fig. 2.2). In the other case, the spin rotation of the Néel wall occurs within the plane of the sample surface [31]. The energy and width of different types of domain walls have been calculated [4, 32, 33].

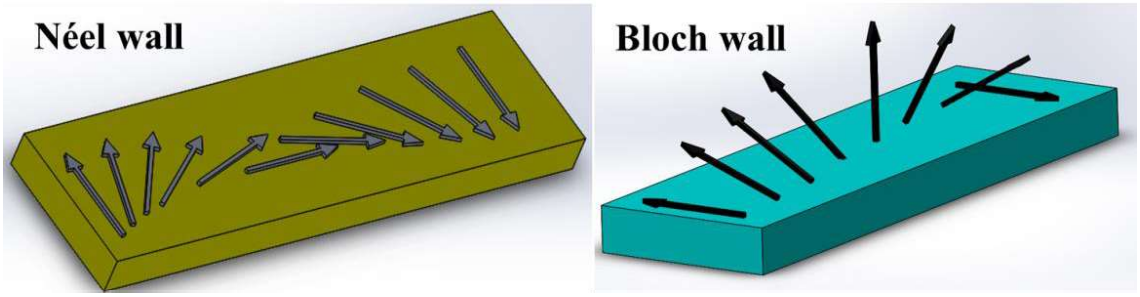

Figure 2.2: Schematic of Néel wall and Bloch Wall.

The width of the domain wall depends upon the exchange and the anisotropy energy contributions which are involved in rotation of the spins. The exchange energy contribution favours to keep all the spins aligned parallel to each other, which results in moderating the rotation angle between two adjacent spins by spreading the width of the boundary. In contrast, the magnetocrystalline anisotropy term favours to keep all the spins aligned along the direction of the easy axis. This contribution neutralizes the effect of the

exchange energy and tends to reduce the width of the boundary in which the spin direction is deviating from the direction of easy axis. Hence, the arrangement of a magnetic domain wall is an assessment between the exchange interactions which tend to make a wide wall and the anisotropy effect which tend to make a thin wall.

2.4.2 Formation of domain structure

Naturally, domains occur when a domain structure has a lower total energy compared with the uniformly magnetized state or single domain state as shown in Figure 2.3a. The single domain structure (Fig. 2.3a) will divide into multiple domains (Fig. 2.3b) of opposite magnetization in order to reduce the large magnetic stray field. Figures 2.3 c and d demonstrate the possible closure domain structures along two perpendicular easy axes in a cubic crystal. These structures will completely eliminate the magnetostatic energy or the magnetic stray field component out of the surface (Fig. 2.3 c and d). Even though the anisotropy energy favours both the domain structures shown in Figs. 2.3 c and d, the domain structure shown in Fig 2.3c has lower domain wall energy due to fewer domain walls. However, domain structure shown in Fig 2.3d occurs more frequently due to magnetostriction effects. In demagnetized condition, domains are magnetized in different directions, and the domains are distorted in different directions because of the magnetostriction.

The specimen with domain structure shown in Fig. 2.3d can be easily deformed over most of its length because the distortion produced by magnetization in opposite directions is the same. Some magnetoelastic energy is required to hold the small spike triangular domains or closure domains to the rest of the specimen, but this energy is much less than that required for the large domains of Figure 2.3c. As a result, the size of the

domains in materials with cubic crystal structure is generally limited by the magnetoelastic energy.

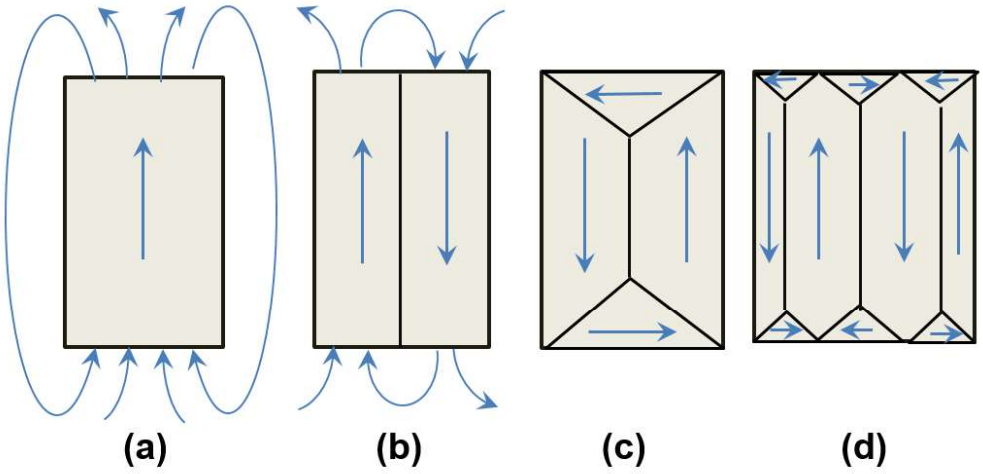

Figure 2.3: Schematic of (a) a uniformly magnetized single domain, (b) parallel domains with opposite magnetization and (c) and (d) closure domain structures.

Generally, thin films exhibit in-plane magnetization with the film surface for uniaxial or bi-axial anisotropy, as shown in Figs. 2.4 a and b, respectively. In case of a strong uniaxial perpendicular anisotropy, the material will have magnetization along the normal to the film and favours an out-of-plane magnetization as shown in Figs. 2.4 c and d with stripe or bubble type domains, respectively. The trend of the magnetization to rotate out-of-plane, however, is hindered by the presence of the magnetic charges on the surface of the film which contribute to the magnetostatic energy. The ratio (Q_a) between the anisotropy and the stray field energy is a material parameter. It is a dimensionless quantity defined by $Q_a = {}^{K}/_{K_d}$, where K is the first-order constant of any kind of anisotropy constant and K_d is the stray field energy density *i.e.* $K_d = \frac{\mu_0 {M_s}^2}{2}$. A soft magnetic material has $Q_a \ll 1$ and the domains are in-plane magnetized. In hard magnetic

material ($Q_a \gg 1$) with high perpendicular anisotropy, out-of-plane magnetization is favoured [34].

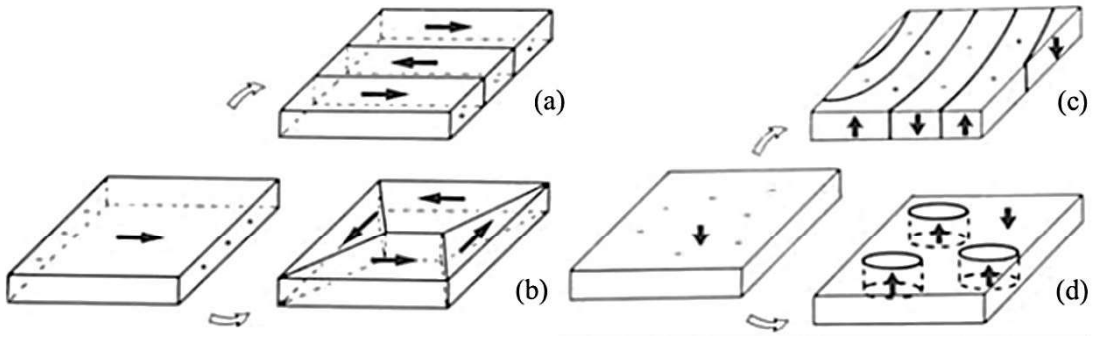

Figure 2.4: Schematic of magnetic domains in thin films with (a and b),in-plane and (c and d) perpendicular magnetization, termed as stripes (a and c), closure domain (b) and pattern magnetic bubbles (d) [35].

The magnetic domains may occur to moderate the magnetostatic energy or to favour the local magnetocrystalline anisotropies or to the specimen shape depending on the material constants, the size of the specimen, and external parameters (*e.g.*, magnetic field, stress). Basically, the domain theory provides in-depth understanding of the magnetic domains and is indispensable for micromagnetic calculations.

2.5 MAGNETIC DOMAIN IMAGING TECHNIQUES

The integral bulk magnetometry techniques; such as Vibrating Sample Magnetometer (VSM) [36], Superconducting QUantum Interference Device (SQUID) magnetometer [37], Alternating Gradient Magnetometer (AGM) [38] and Magneto-Optical Kerr Effect (MOKE) magnetometer [39] are used to obtain averaged information about the bulk magnetization and become highly beneficial when dealing with macroscopic samples or very large numbers of identical nanostructures. However, in the case of micro-magnetism, a precise understanding of the properties of magnetic nanostructures is vital for application on technological implications. Hence, experimental

techniques with adequate resolution and sensitivity are essential for the detailed study of magnetic phenomena at the nanoscale [40].

Imaging of magnetic domains and their dynamics provides the most direct access to the effective magnetic properties of materials at various ranges from macro to the nanoscale [41]. The knowledge of the magnetic domain behaviour with external influence gives unrivaled insight into the origin of micro-magnetization reversal mechanisms. Magnetic domains are visualized by various techniques which are developed in the 20th century [42-44]. Currently, a number of techniques involving various physical mechanisms of magnetic contrast formation is used consistently for imaging of magnetic micro/ nanostructures. Based on the requirements, different imaging methods were adopted in various studies. The numerous techniques available for magnetic domain imaging include:

- Bitter pattern technique
- Magneto-optical Kerr Effect Microscopy (MOKE)
- Type I and Type II Scanning Electron Microscopy (SEM Type I and Type II)
- Scanning Electron Microscopy with Polarization Analysis (SEMPA)
- Lorentz Transmission Electron Microscopy (LTEM)
- Electron Holography
- X-ray Magnetic Circular Dichroism (XMCD)
- Spin Polarized Low Energy Electron Microscopy (SPLEEM)
- Magnetic Force Microscopy (MFM)
- Scanning Hall Probe Microscopy (SHPM)
- Scanning Superconducting Quantum Interference Device (SQUID) Microscopy
- Spin Polarized Scanning Tunneling Microscopy (SP-STM)

- Neutron grating interferometry techniques

In general, there are a few common facts that apply to every domain imaging method. At first, each method is related to the sample's magnetization or to the magnetic field generated by that magnetization. The former is very useful in understanding or developing new materials and the latter is of practical significance in devices. Second, most of the methods are limited to the topmost few micrometres and are therefore dominated by surface magnetic structure. Third, every technique desires to have smooth, clean, damage-free surfaces. In general, the surfaces need to have at least the equivalent of a mirror polish. Otherwise, topography and surface stress may influence the measurement to varying extents [43].

Bitter pattern technique is the earliest method of domain observation [45, 46], developed by Bitter [47], which is based on the observation of stray field configurations in the domain structures by fine colloidal suspension of magnetic particles coated on the surface. Still, Bitter is the simplest technique for the applications which quickly provide the information of size and shape of the domains present in the material [48]. This method reveals domain walls which intersect the surface because the resulting stray fields interact with the magnetic particles stronger than the surrounding regions. In conventional form, the optical microscope was used to capture decorated sample with magnetic colloids on the sample surface and the higher resolution is attained with the scanning electron microscope.

In ***Magneto optic imaging***, the contrast is obtained with the interaction between polarized light and a sample's magnetization, which leads to several useful optical domain imaging applications [21, 41, 49] Although the physics of the magneto optic interactions can be rather complicated [25], the basic level of magneto-optic imaging is

only based on the rotation of the plane of polarization of linearly polarized light upon reflection from, or transmission through a magnetic material. In transmission mode, magneto optic effect is basically referred to as “Faraday effect”, which is applied rarely and also only in transparent materials. In reflection mode, the technique is known as ‘Kerr effect’. In both methods, domain contrast in the image is directly related to the magnitude and direction of magnetization in the sample. Moreover, MOKE also provides the possibility of measuring local magnetization curves. The scanning Kerr microscopy can record images very fast within the nanosecond scale, providing to study the dynamics of domain pattern formation (micro-magnetization). However, the resolution of the MOKE technique is limited to the optical source used (few hundred nanometers). The recent review of optical imaging has been given in [41].

In principle, conventional ***SEM*** can also be used to image the magnetic domain with the two distinct contrast mechanism such as ***Type I*** and ***Type II*** magnetic contrast [50, 51]. In both cases, the electrons in the magnetic field get deflected by the Lorentz force. However, in former mechanism the contrast arises from deflection of the low energy secondary electrons by the stray field out of the surface [29]. In the latter case, the contrast arises from the high energy backscattered electrons deflected by the magnetic field within the material. The resolution in both the cases is of the order of ~300 nm and is roughly determined by the penetration depth for the incident electron.

Scanning Electron Microscopy with Polarization Analysis observes surface magnetization distribution by measuring the spin polarization of secondary electrons ejected from a magnetic sample due to the high energy electron beam incident on the material [52, 53]. SEMPA can directly detect the sample magnetization component with a high spatial resolution of about 20 nm [43]. The main constraint in application of SEMPA

is the fact that the measurements must be carried out in ultra-high vacuum on a well prepared clean conducting surface.

Lorentz transmission electron microscopy can produce high spatial resolution magnetic domain images [54, 55]. Similar to the SEM Type I and Type II methods, Lorentz force causes the deflection of the electron beam transmitting through the thin magnetic specimen. Contrast in regions with different magnetization can be obtained due to the electron beam trajectory deflects when it passes through a region of magnetic induction. In general, two different variants of Lorentz microscopy such as Fresnel and Foucault modes can be used. Using the Fresnel mode, domain walls can be visualized and distinguished from other features such as dislocations. Adopting the new aberration-corrected microscopes, spatial resolution in the order of 1 nm can be achieved. However, the applications of LTEM technique is limited due to the high cost of the TEM instrument, involvement of very special specimen preparation such as flat, very thin and also electron transparent, and it is hard to apply magnetic fields to the sample as this often changes the electron beam trajectory.

Electron holography, uses a high energy field emission transmission electron microscope (FE-TEM) to form an interference pattern from electrons that can reach the detector via two alternative paths, the lines in the interference pattern can be directly interpreted as flux lines. This technique makes possible both direct observation and quantitative measurement of magnetic flux and a resolution of 10 nm has been achieved [56]. Since it is a transmission technique, same constrained as TEM is applicable here also such as the thin transparent and conductive specimen.

X-ray magnetic circular dichroism is made possible by the availability of variable, high intense synchrotron radiation source. The method is based on the relative

orientation of the x-ray photon angular momentum and the sample magnetization [57, 58]. The difference in the absorption of x-rays, termed as x-ray dichroism, is maximum when magnetization of the material and the photon polarization or helicity, are parallel and antiparallel. Magnetization images of a monolayer thick magnetic film can be observed.

Neutron grating interferometer technique utilizes the interaction of the polarised neutron beam with the spins of the electrons and nuclei, while passing through the magnetic material [59, 60]. This technique allows a wide field observation by taking projections at diverse angles which facilitates a 3D visualization of the domain structure, but the spatial resolution is low. The main drawback is very expensive and requires access to a nuclear reactor.

Scanning probe microscopy based magnetic domain imaging utilizes various types of stray field detection methods for visualization of magnetic microstructure [42]. The semiconductor Hall and SQUID sensors are used for obtaining the magnetic stray field out of the sample surface with very high sensitivity [61, 62], but relatively low resolution. In that, MFM is one of the dynamic modes scanning probe techniques which detects magnetic stray field of the material surface by the magnetostatic interaction between sample surface and the cantilever tip coated with thin layer of a magnetic material. Due to the long range magnetostatic interaction, MFM needs minimal sample preparations and can be used in ambient conditions to provide a spatial resolution down to 10 nm [63]. MFM is well suitable to study multi-phase and relatively large thick (bulk) materials by measuring simultaneously the topography and the magnetic microstructure [64].

The above mentioned techniques have their own limits and advantages, and are complimentary to each other. The summary of a few most important techniques has been given in Table 1. In the present thesis, MFM has been employed to study the magnetic domain dynamics in the polycrystalline bulk structural materials due to its easy implementation, good spatial resolution and possibility of domain imaging with in-situ external field application.

Table 2.1: Comparison of magnetic domain imaging methods [25, 42, 43]

Imaging techniques	**Sensitivity for small variations in magnetization**	**Evaluation of the magnetization vector**	**Spatial Resolution best/typical (nm)**	**Depth Information (nm)**	**Acquisition time**	**Sample quality preparation**	**Maximum applied external Field (Oe)**	**Capital investment**
Bitter	Good	Indirect	100/500	500	0.3 s	Moderate low	No limit	Low
Magneto – optic Kerr	Fair	Direct	200/500	20	10^{-8} – 1 s	High	No limit	Moderate
SEM Type I and Type II	Poor	Indirect	500/1000	2	1 – 100 min	Moderate low	~100	High
SEMPA	Good	Quantitative	20/200	2	1 – 100 min	Very high	None	Very High
Lorentz TEM	Very good	Indirect	10/50	Sample thickness	0.03 – 30 s	High	10000	High
Electron Holography	Good	Quantitative	5/20	Sample thickness	0.03 – 10 s	Very High	1000	Very High
SPLEEM	Good	Quantitative	20/40	1	1 s	High	None	Very High
XMCD	Poor	Indirect	300/500	2 - 20	0.03 – 10 s	Moderate	None	High
MFM	Good	Indirect	30/100	20-500	5 – 30 min	Moderate low	3000	Moderate
Neutron	Poor	Indirect	1000/5000	No limit	1 – 30 s	low	No limit	Extremely High

2.6 MAGNETIC FORCE MICROSCOPY

The first probe microscope, scanning tunnelling microscope, was invented in 1981 [65]. It is based on the quantum tunnelling effect to investigate the surface morphology with the atomic resolution. A few years later, the same group developed comparatively simple approach, which can sense the forces between the probe and the surface, famously known as atomic force microscopy (AFM) [66]. This force microscope can detect all short / long range of tip-sample interactions such as electrostatic, magnetostatic, Van der Waals, adhesive, friction, elastic modulus, chemical and magnetic exchange. Schematic of a macroscopically uniform surface probed by a sharp tip and tip-sample interaction are shown in Figs. 2.5 a and b, respectively. The different interatomic and electromagnetic forces as a function of distance of tip from the sample surface are shown in Fig. 2.5c [69].

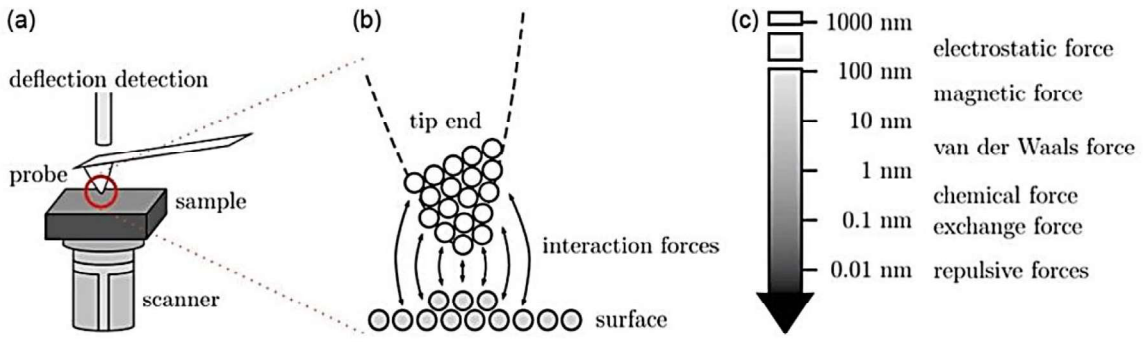

Figure 2.5: Schematic of (a) a macroscopically uniform surface probed by a sharp tip. (b) the tip-sample interaction at the atomic scale and (c) Different forces as a function of distance of tip from the sample surface [67]

Hence, AFM has been adapted to the various methods in which a handful of different properties in the material can be measured, such as force modulation microscopy, electrostatic force microscopy, Kelvin Probe force microscopy, magnetic resonance force microscopy, contact resonance AFM, liquid AFM and chemical AFM.

MFM is one of the two-pass dynamic methods in atomic force microscope. It has great acceptance as a powerful magnetic imaging technique for studying and analyzing the magnetic structure on the surface of ferromagnetic materials with the resolution of few tens of nanometers [68]. It has been commonly employed for imaging magnetic domain structures on a wide variety of magnetic materials, such as high-density recording media [69, 70], ultrathin films [71], nanoparticles [72], patterned elements[73, 74], template-mediated assembly of nanoclusters, nanowires [75], multilayers [76], magnets, and biological samples [77] as well as other magnetic features and nanostructures.

2.6.1 Basics of magnetic force microscopy

The first magnetic force microscope was developed by Y. Martin and H.K. Wickramasinghe in 1987 for studying local magnetic properties [78]. The working principle of MFM is similar to that of an AFM except for using a cantilever tip coated with a thin layer of ferromagnetic material with specific magnetization. Here, the description of the interaction between sample magnetic field $\vec{H}$(r) and the tip magnetization is quite complicated. However, due to the shape of the tip, the tip moment is more stable and stronger for the axial magnetization. The tips are magnetized along their axes and the fields are highly localized to the tip. The cantilever deflection senses the force mostly in the direction normal to the sample surface. The magnetic tip can be considered as a single point magnetic dipole having the magnetic moment $\vec{\boldsymbol{m}}$ and the respective magnetostatic energy of the tip-sample is the scalar product of the $\vec{H}$ and $\vec{m}$.

$$E_{ms} = -\left(\vec{H}.\ \vec{m}\right) \tag{2.10}$$

Figure 2.5 shows the schematic of the magnetostatic interaction between the tip and the sample. In general, the magnetic moment of the MFM tip can be written as a

superposition of the dipoles as a form of $\vec{M}dV$, where $\vec{M}$ is the magnetization of the tip coating and dV is the elementary volume of the coating layer.

The total energy of the interaction of the tip-sample can be obtained by integrating over the complete layer of the tip.

$$E_{layer} = -\int_{layer} \vec{M}(\vec{r}') \,.\, \vec{H}(\vec{r}' + \vec{r}\,)\, dV' \tag{2.11}$$

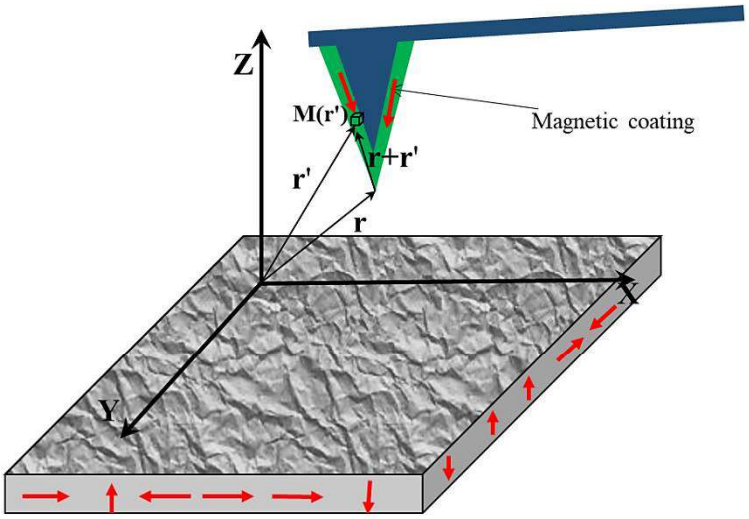

Figure 2.6: Schematic of the magnetostatic interaction of tip and sample.

Then, the interaction force of the tip with the magnetic field of the sample is given as

$$\vec{F} = -grad\left(E_{layer}\right) = \int_{layer} \nabla\left(\vec{M} \,.\, \vec{H}\right) dV' \tag{2.12}$$

Hence, the vertical (Z) component of the force is

$$F_z = \int_{layer} \left[M_x \frac{\partial H_x}{\partial z} + M_y \frac{\partial H_y}{\partial z} + M_z \frac{\partial H_z}{\partial z} \right] dV' \tag{2.13}$$

and the force gradient of the z- component is

$$F'_z = \int_{layer} \left[M_x \frac{\partial^2 H_x}{\partial z^2} + M_y \frac{\partial^2 H_y}{\partial z^2} + M_z \frac{\partial^2 H_z}{\partial z^2} \right] dV' \tag{2.14}$$

In general, MFM operates in the non-contact mode or attractive force region. There are presently two main approaches in MFM imaging:

- Force mode MFM
- Force gradient mode MFM

In force mode MFM imaging, a magnetically active tip maps the surface by maintaining a constant height (10-100 nm) above the sample of interest. The magnetostatic interaction between the stray field from the sample and the known magnetization of the probe produces a force *F(x,y)* that deflects the tip and the associated cantilever from its nominal position. The cantilever deflection (δ) is measured by the standard AFM laser photo-diode optical system and an image of the magnetic structure of the sample is thus obtained. This mode of operation is also known as static or DC mode MFM. The interaction force F is measured through the detection of the cantilever deflection δ from the equilibrium position which is given by

$$\delta \approx \frac{F}{k} \tag{2.15}$$

where, k is the cantilever spring constant. However, in order to perform the scanning at certain constant height, a two-pass technique is considered for the specimen with evident roughness. In the first pass, topography of the surface is obtained in tapping mode or semi-contact mode which is influenced only by the short range (<10 nm) Van der Waals force between the sample surface and the probe. In the second pass, the probe is lifted by a particular height (z-offset) to circumvent the influence of van der Waals force and the probe traces the topography obtained in the first pass to sense the long range magnetic interaction.

The other operating mode is force gradient or dynamic or AC mode MFM. The dynamic MFM mode is also a two pass technique. With the help of a piezo-vibrator cantilever oscillations are excited at a frequency close to resonance. During the first pass in semi-contact mode the surface topography is recorded. On the second pass, the tip goes above the sample with a trajectory corresponding to the first pass so that the average lift off (z-offset) separation is kept at a constant value h, as shown schematically in Fig. 2.7.

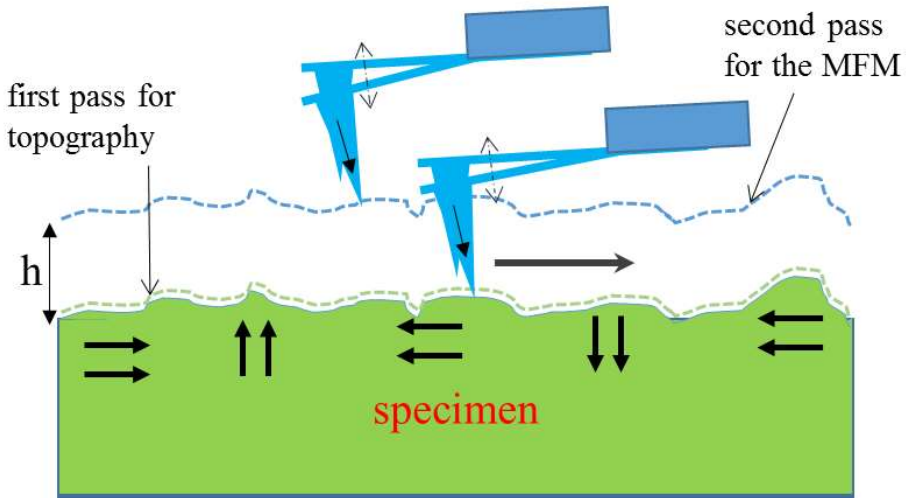

Figure 2.7: Schematic of the two pass approach of MFM imaging.

here, MFM tip interacts with the magnetic stray field emanating from the sample surface, which changes the resonance frequency of the cantilever. The resonance frequency shifts in the range of 1-50 Hz for cantilevers having a resonance frequency f_0 ~ 100 kHz. The frequency shift (∇f_0) of the cantilever is proportional to the vertical gradient of the magnetic force on the tip, which can be detected in one of the following ways: phase detection, which measures the cantilever's phase of oscillation relative to the piezo drive; amplitude detection, which tracks variation in oscillation amplitude; and frequency modulation, which detects shift in resonant frequency directly. The MFM image can be formed by monitoring changes in the phase (φ), amplitude (A) or resonant frequency (f_0) of the tip oscillations. If the force gradient acts on the cantilever in the vibration direction

z, then the above mentioned parameters can be expressed in terms of force gradient as follows,

$$\nabla\varphi \approx \frac{Q}{k}\frac{\partial F}{\partial z} \tag{2.16}$$

$$\nabla A \approx \frac{2A_0 Q}{3\sqrt{3k}}\frac{\partial F}{\partial z} \tag{2.17}$$

$$\nabla f_0 \approx -\frac{1}{2k}\frac{\partial F}{\partial z} f_0 \tag{2.18}$$

where, Q is the quality factor of vibrating cantilever, A_0 is the amplitude of cantilever oscillation at resonant frequency (f_0) in the absence of external force gradient. It can be seen in the above equations that all the experimentally determinant variables are linear functions of the force derivative. Phase map can provide the qualitative information and more regularly opted due to its ease of use, greater signal-to-noise ratio, and reduced artifacts content. The variations in the magnetic interaction force between the cantilever tip and the sample surface can be measured by a position-sensitive optical deflection sensor, which is used to detect the cantilever motion and hence to measure the force gradient due to the tip-sample magnetostatic interactions. The force gradient, as low as 10^{-6} N/m, can be easily detected.

2.6.2 Interpretation of MFM images

MFM images do not correspond to the sample magnetization directly, but depict the force gradient of tip-sample magnetostatic interaction due to the stray field over the surface. Moreover, magnetic interaction between a sample and a magnetic tip is highly complicated due to the long range magnetic forces and their complex sources, along with the potential field interaction between tip-sample and also the interaction of the stray field of the tip may influence the sample magnetization in soft magnetic samples. A magnetic

material such as Co, CoCr, CoPt, or NiFe of thickness around (20 - 40 nm) is coated on the flexible micro fabricated cantilever based on the application. The resolution of the MFM image depends on the tip radius and also on the Z-offset (lift scan height) in the second pass [79, 80]. The tip is most often magnetized vertically to make it sensitive to the vertical components of the sample stray field. In MFM images, the magnetic domain variations appear as either dark or bright contrast, depending on the attractive or repulsive force gradient, respectively.

MFM images, obtained with the tip magnetized vertically, do not differentiate direction of the in-plane magnetized domains. Figure 2.8a shows the MFM imaging of a thin film with in-plane magnetization of the two domains aligned opposite to each other which are separated with a Néel domain wall. When the tip is scanned over the sample, the attractive region at the edges of the domain walls appear with a dark contrast and next to that the repulsive region appear with a bright contrast as shown in the MFM image along with the Fig. 2.8a. In case of a sample with out-of-plane magnetization, flux is closed outside the sample at the domain boundaries, as indicated in Fig. 2.8b. The perpendicular component of this force changes signal at the center of the domain wall, resulting in an image as shown on the right. In case of out-of-plane domains this is relatively easy due to the image contrast, but in case of in-plane domains, only the domain wall is observed and have a difficulty in identify the different magnetization directions. The pattern of MFM images of different domain states were properly illustrated in [81], as shown schematically in self-explanatory images of Fig. 2.9.

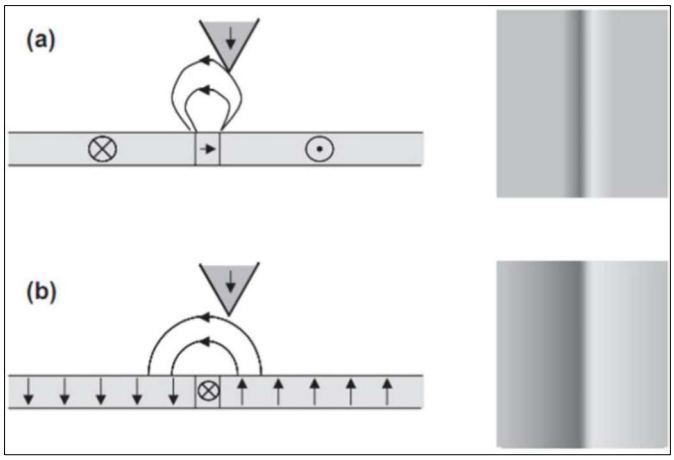

Figure 2.8: Representation of the contrast in MFM: (a) a thin film with in-plane magneitzation exhibits contrast only at the domain wall (b) an out-of-plane magnetization exhibits domain contrast due to the stray field emananting from the domains [42].

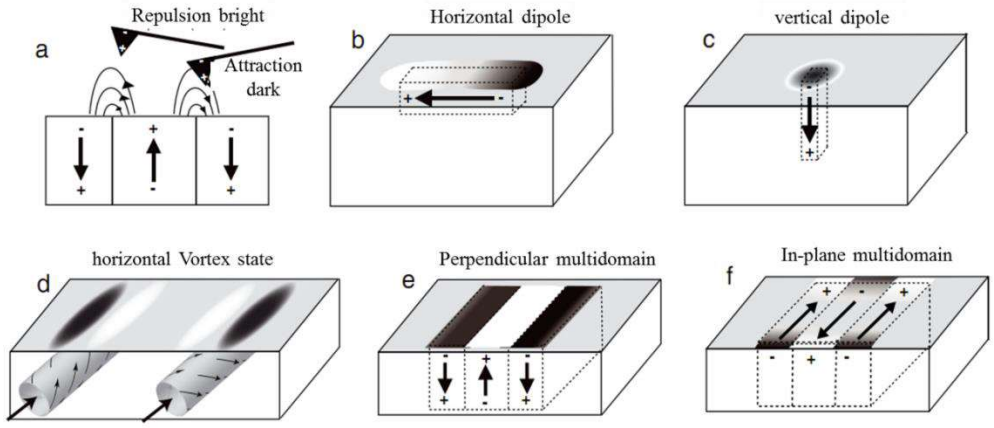

Figure 2.9: Illustration of the MFM principle: (a) a vibrating cantilever scanning across a sample with out-of-plane domain magnetization and (b) – (f) patterns of MFM phase contrast in different domain states [81].

2.6.3 MFM applications

In the early 1990s, MFM got acceptance as one of the widely applicable method for studies in magnetic materials and in the development of magnetic logic devices. Especially, the magnetic storage industry became an important field of industrial

application to produce high density magnetic recording media [63], which led to more commercial availability of the instrument. Nowadays, most of the AFM manufactures provide the multimode equipped instruments which can be used as an MFM. In the past three decades, MFM has been used for almost all types of ferromagnetic materials from the bulk samples to the ultra-thin films [82, 83] and imaging of soft magnetic materials to hard magnets [84, 85]. Notice the importance of the MFM not only because of its capability for imaging the domain structure, but also for its usefulness as a powerful tool to understand the magnetization process in the submicrometer scale [86, 87]. Numerous works have been performed with the variable field MFM to study the magnetization reversal phenomenon [74, 86, 88-92]. For example, Asenjo et.al [86] demonstrated the effect of the stress on the magnetization process by visualizing the evolution of the weak perpendicular out-of-plane domain structure in thin film of Fe-B/Co-Si-B multilayer with an external magnetic field as shown in Fig.2.10.

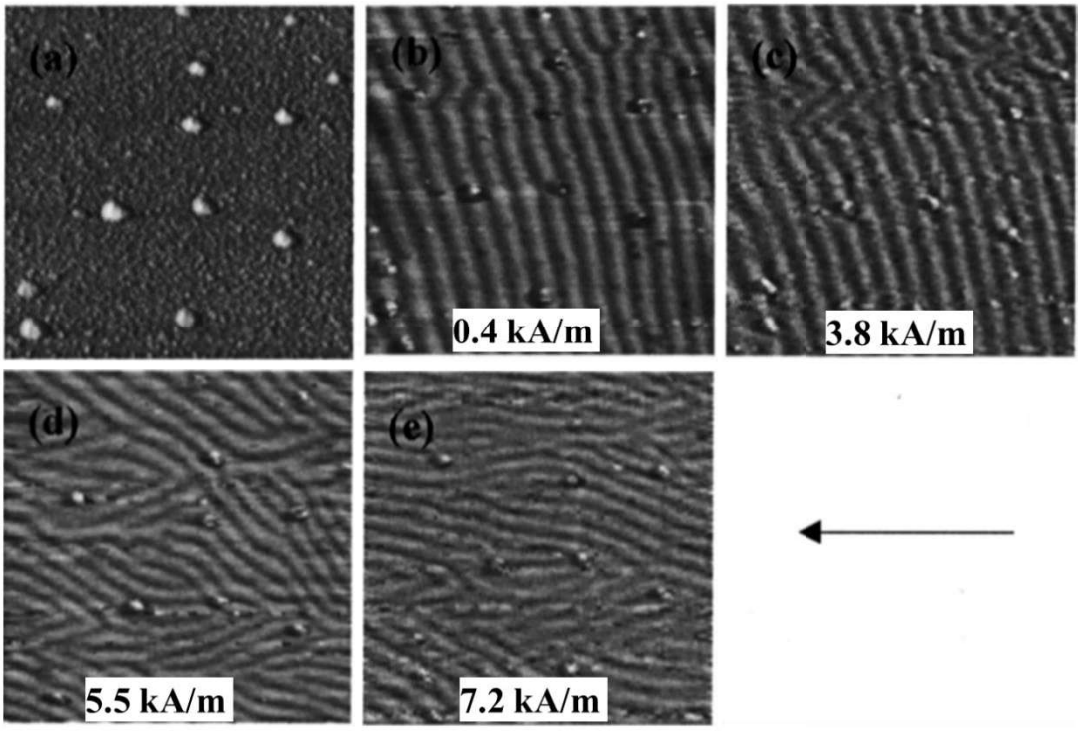

Figure 2.10: (a) Topography of the Fe-B/Co-Si-B multilayer (b)-(e) MFM image at different external field applied along the arrow mark direction [86].

Low temperature MFM measurements have also provided fundamental understanding of magnetic properties [71, 93]

In the past, quite a few bulk polycrystalline materials were studied using MFM imaging such as duplex stainless steel [94-97], pearlitic steel [98], Ni-Cr hard face alloy deposited on 316LN stainless steel [99], chromium depleted regions in metastable Fe-Cr-C alloy [100], aged 321 stainless steel [101], maraging steel [102] and austenitic stainless steel [103, 104]. However, imaging the field induced domain wall dynamics with external field in the polycrystalline materials have been very limited [98, 105].

2.7 BACKGROUND OF THE SELECTED MATERIALS

The present thesis mainly focuses on the studies of different types of magnetic domains in bulk polycrystalline ferromagnetic materials using MFM. Three different structure of ferromagnetic materials are selected: (i) a polycrystalline pure iron having average grain size of about 80 μm containing only ferromagnetic phase, (ii) a duplex stainless steel consisting of equal proportions of elongated ferromagnetic and paramagnetic phases of ~5 μm width and ~ 100 μm length, and (iii) a cold worked AISI type 304 stainless steel with very fine particles (<1 μm diameter) and lamellae shaped (~1 μm width and ~ 5 μm length) martensite (ferromagnetic) phases in the austenite matrix.

2.7.1 Studies of magnetic domians in iron

Iron is a very well-known ferromagnetic material over many centuries and abundantly available metal in the earth crust [2]. The iron-silicon alloys (electrical steel magnetically equivalent to pure iron) are commonly termed as soft magnetic materials, which are used mainly in the electrical machines, inductive devices and electronic

industries [106]. Iron has body center cubic crystal structure. Hence, the easy and hard axes of magnetization are <100> and <111>, respectively as shown in Fig. 2.11.

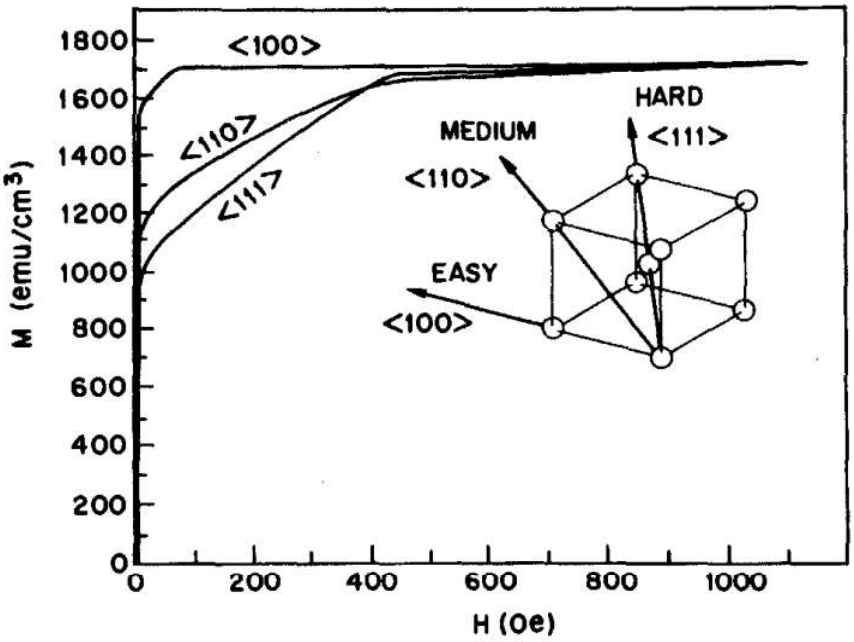

Figure 2.11: Magnetization curve of an iron single crystal [30].

Generally, multi easy axes materials have low perpendicular anisotropy which prefers domain alignment parallel to the surface [25]. The magnetic domains in the different planes of grain oriented silicon iron (3% silicon) were observed with the specific grain orientation [107-109]. In case of {100} grain orientation, closure domain structure with the 90^0 domain walls were observed using optical Kerr microscope as shown in Fig 2.12a. In case of {110} planes, domain structures with 180^0 walls were observed and lancet type reverse domains were also observed (Fig 2.12b). The iron-silicon crystal with surface parallel to {111} exhibit a complicated domain structure (Fig. 2.12c) as it does not have any easy axis of magnetization in the plane. Similar results were reported by Gallaugher et. al [110] in a sheet electrical steel with randomly oriented grains, using forescatter detector and electron backscatter diffraction. The changes in domain structure with the external field and stress effect were also studied [111]. The soft iron alloys have been

exploited in the design of magnetic materials of commercial importance, *e.g.* conducting losses are reduced by the grain oriented electrical steels.

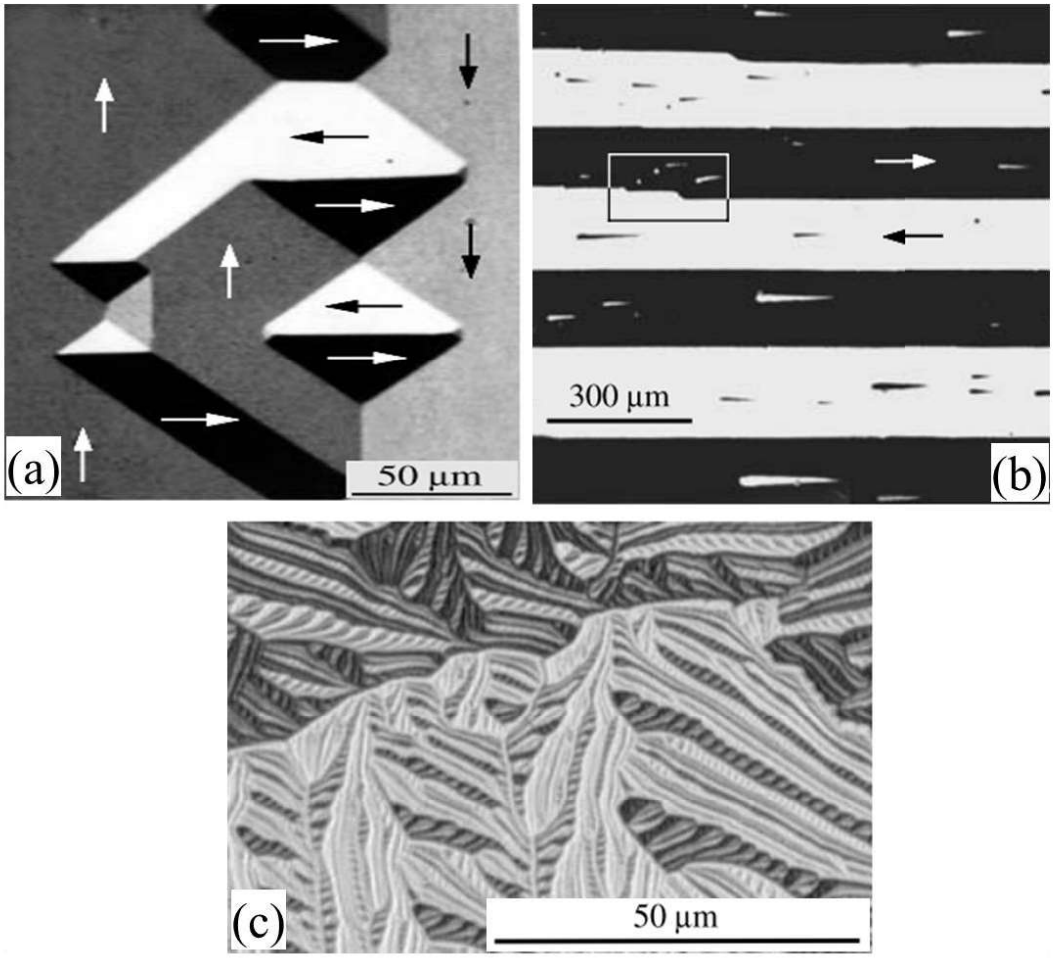

Figure 2.12: Magnetic domain images of iron silicon single crystals having planes orientation along (a) {100} (b) {110} (Magneto optical Kerr image) and (c) {111} (high resolution MFM image) [25].

Batista et al. [105] have recently studied the influence of external magnetic field on the domain structures in polycrystalline pure iron and unalloyed steels using MFM cantilevers with tips coated with CoCr alloy with a coercivity of ~400 Oe. In the range of the magnetic field (±250 Oe) applied in their study, reversible movement of a few domain walls have been visualized on the surface of pure iron specimen (marked as 3 with arrow

in Fig. 2.13). However, as the applied field was too low as compared to the saturation field of iron (~10000 Oe), different magnetization phenomena could not be visualized.

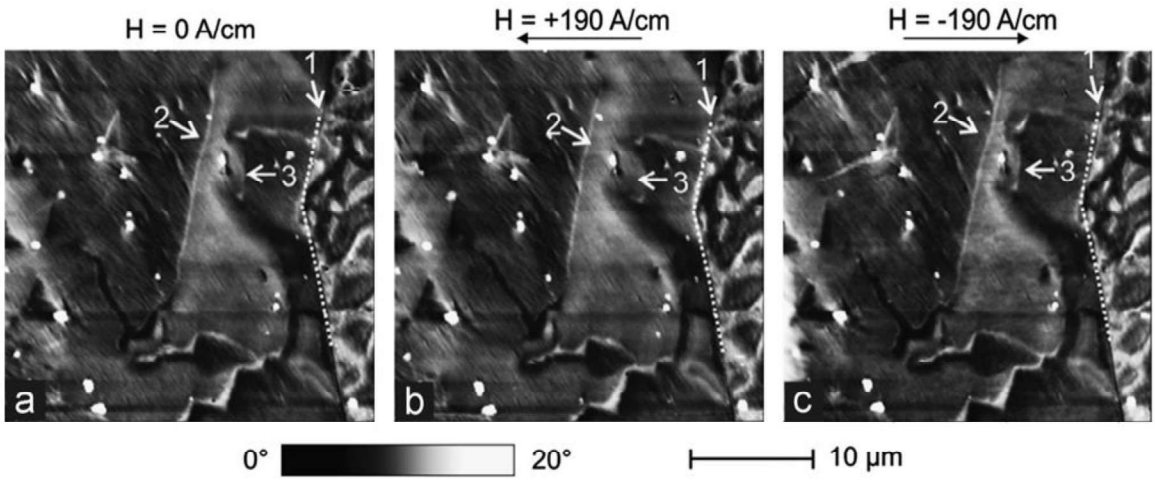

Figure 2.13: MFM images of a bulk polycrystalline iron with in-plane magnetic field [105].

2.7.2 Duplex stainless steel

Duplex stainless steel (DSS) is a significant and expanding class of stainless steel in industrial and technical applications. The microstructure of DSS consists of nearly equal proportions of γ-austenite (face center cubic) and δ-ferrite (body center cubic) phases, which contribute to high mechanical strength and excellent corrosion resistance properties [112-114]. DSS microstructure can be described as islands of austenite (paramagnetic) in ferrite (ferromagnetic) matrix. Several studies have been reported on the non-destructive characterization of DSS using magnetic techniques, which are sensitive to the structure of ferromagnetic phase [115-118]. In addition to the conventional methods, magnetic domain visualization methods have also been used for characterization of DSS. Earlier, magnetic domain structure of the DSS was visualized using TEM [119]. In the last two decades, several studies have been reported on microstructural characterization in DSS through the visualization of magnetic domains

using MFM [94-97, 120-124]. In DSS, MFM can easily differentiate ferrite from the austenite phase because of the presence of distinct maze type and stripe magnetic domains in the ferrite phase [97]. MFM has been used for microstructural characterization, secondary sigma phase identification [94, 122] and to study the effect of heat treatments [123, 124] in DSS. Domain patterns with different contrast and widths were observed in DSS samples annealed at different temperatures [123]. These observations were attributed to various orientations of the grains. However, quantitative correlations of crystallographic orientation with contrast/width of domains were not attempted. Even though, various MFM studies have been carried out in DSS, the micro-magnetization behaviour of DSS in the presence of external field has not been reported so far through direct domain visualization using MFM or any other domain imaging technique.

2.7.3 Cold worked AISI 304 austenitic stainless steel

Austenitic stainless steels are used in a wide variety of technological and commercial applications as a structural material, especially in nuclear power plants and chemical and petrochemical industries. It has good corrosion resistance combined with their relatively high toughness, formability and weldability. However, it has relatively low yield strength in the annealed state [125-127]. The conventional AUSSs consist of γ-austenite phase whose stability decreases with reduction in the austenite stabilizing element (usually nickel). When the austenitic stainless steels are subject to thermo-mechanical treatment, dislocations and twins are generated which cause the transformation of the metastable γ-austenite phase (paramagnetic) to the α'-martensite phase (ferromagnetic) by strain induced martensite transformation. The martensitic transformation in austenitic steels have also been reported during sub-zero deformation,

hydrogen charging and ion implantation [128-130]. The amount of martensite formation depends on the chemical composition and working temperature [131, 132]. An increase in the volume fraction of the martensite increases the strength as well as magnetic moment of the stainless steel [133, 134].

MFM has been used to detect the magnetic phases in the stress corrosion regions [102] and tip of fatigue crack regions of AUSS [103, 104]. The observed magnetic region around the grain boundaries of the chromium depleted sensitized AUSS are shown in Fig. 2.14.

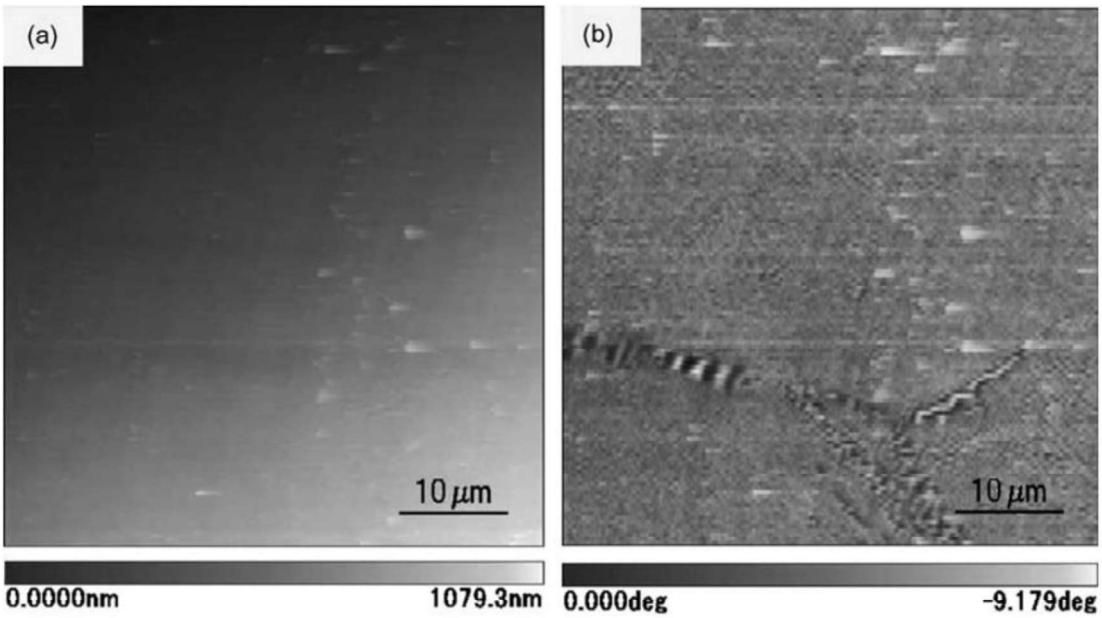

Figure 2.14: The chromium depleted region in an AISI type 304 AUSS specimen (a) AFM topography and (b) MFM phase image (revealing magnetic domains at the grain boundaries) [103].

Interestingly, Sort et. al. [135] generated local martensite phases with nano-indentation method and studied them with MFM. Such controlled and localized martensite transformation in AUSS can be used to generate controlled ferromagnetism in a non-magnetic matrix, which can be used for micro-magnetization studies in the structural materials

2.8 MOTIVATION AND OBJECTIVES

MFM is a powerful tool for studying the magnetic domain structure in magnetic materials with high resolution. It has found very wide applicability in all types of magnetic materials due to the minimal sample preparation requirement and good performance of the system in the ambient atmospheric condition. Hence, MFM is a suitable technique to get high resolution magnetic domain imaging in steels. In additional to that, MFM superposed with the external magnetic field enables visualization and interpretation of the magnetic domain dynamics and micro-magnetization events.

In the present dissertation, external field value of ±2000 Oe has been used to investigate the micromagnetic phenomena in polycrystalline iron and iron based alloys with different microstructure such as complete ferromagnetic polycrystalline pure iron, partially ferromagnetic duplex stainless steel consisting of equal proportion of ferrite/austenite phases and cold worked AISI 304 stainless steel with very low amount of fine ferromagnetic martensite phase distributed in the austenite matrix.

The main objectives of the present thesis are thus:

- To explore the magnetic properties in bulk ferromagnetic materials at micro/nano scale using MFM technique.
- To understand the influence of crystallographic orientation on magnetic domain structure in bulk polycrystalline ferromagnetic materials.
- To study the field dependent domain wall dynamics *in-situ* by MFM in presence of external magnetic field in the range of ± 2000 Oe to understand various micro-magnetic phenomena
- To study the size effect on magnetic domain structure and field induced domain wall dynamics.

EXPERIMENTAL SETUP 3

3.1 INTRODUCTION

This chapter deals with the experimental setup of MFM in presence of external magnetic field, used in the present dissertation. The NOVA© software and associated features used for acquisition and analysis of MFM images are described. Optimization of experimental parameters, the details of the MFM cantilever used in the present study and magnetic stability of its tip are also described. The specimen preparation procedures for the materials used in the study and details of EBSD measurement are also presented.

3.2 MFM EXPERIMENTAL SETUP

The MFM experiments have been carried out using an NTEGRA AFM/MFM system supplied by M/s. NT-MDT. Co., Zelogonard, Russia. Photograph of the experimental setup is shown in Figure 3.1a. In Figure 3.1a, one of the monitors displays the GUI of NOVA software and the topography and MFM phase maps. The other monitor shows the live optical photograph of the cantilever over the sample surface, as obtained by the optical microscope shown in Fig. 3.1a. NTEGRA system is furnished with a SMENA head (shown in Figure 3.1b) which consists of a cantilever holder, a laser source and a four quadrant photodiode to detect and measure the deflection of the laser. The wavelength of the laser is 650 nm which is class 2R type laser with the maximum output less than 1 mW. The signals from the photodiode are sensed by the controller, which is furnished with a lock in amplifier. The processed data by the controller is then sent to the computer for further processing and analysis. A typical cantilever box with 15 MFM

cantilevers is shown in Fig. 3.1c. In-plane external magnetic field in the range of ±2000 Oe can be generated by the electromagnetic coil, as shown in Figure 3.1d. A hall probe sensor is attached close to one of the pole shoes to measure the field. The maximum field generated by the electromagnet increases with reducing the gap between the shoe poles. The schematic representation of the MFM system equipped with in-plane magnetic field setup is shown in Figure 3.2. MFM setup within the range of ±2000 Oe was used to demagnetizing the specimen by applying cyclic alternative magnetic field of reducing field strength. No remnant magnetization could be observed (using a Hall probe) in the specimen after the demagnetization sequence.

Commonly, two kinds of scanning are possible in AFM, *i.e.*, scan by specimen or scan by probe. The system used in the present study is of the latter type. As MFM is one of the two pass modes of AFM, the detection principle of MFM is same as in AFM.

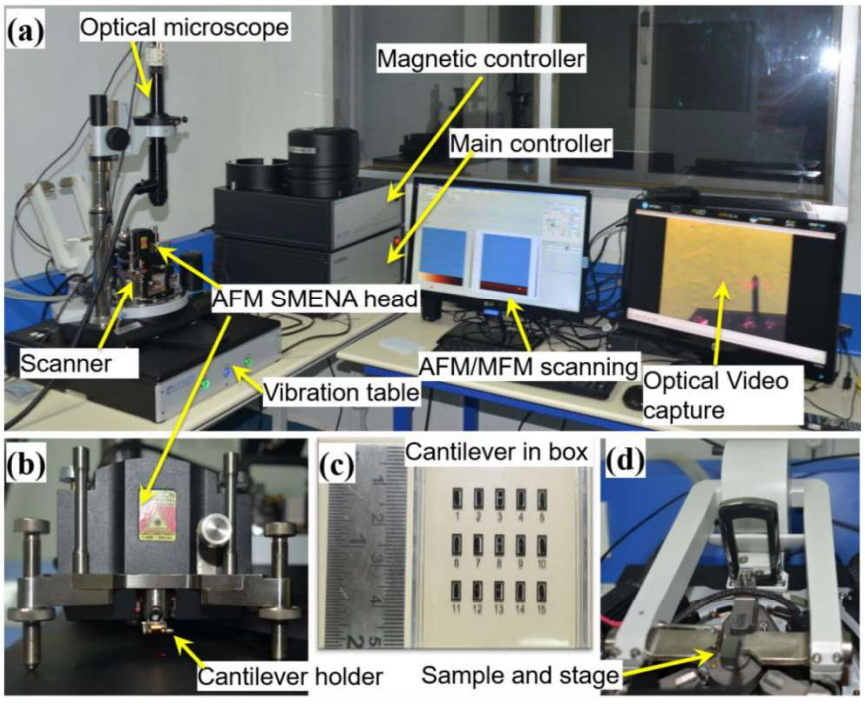

Figure 3.1: Photographs showing (a) the AFM/MFM experimental setup, (b) SMENA head, (c) cantilevers in a box and (d) specimen stage and external in-plane electromagnet setup.

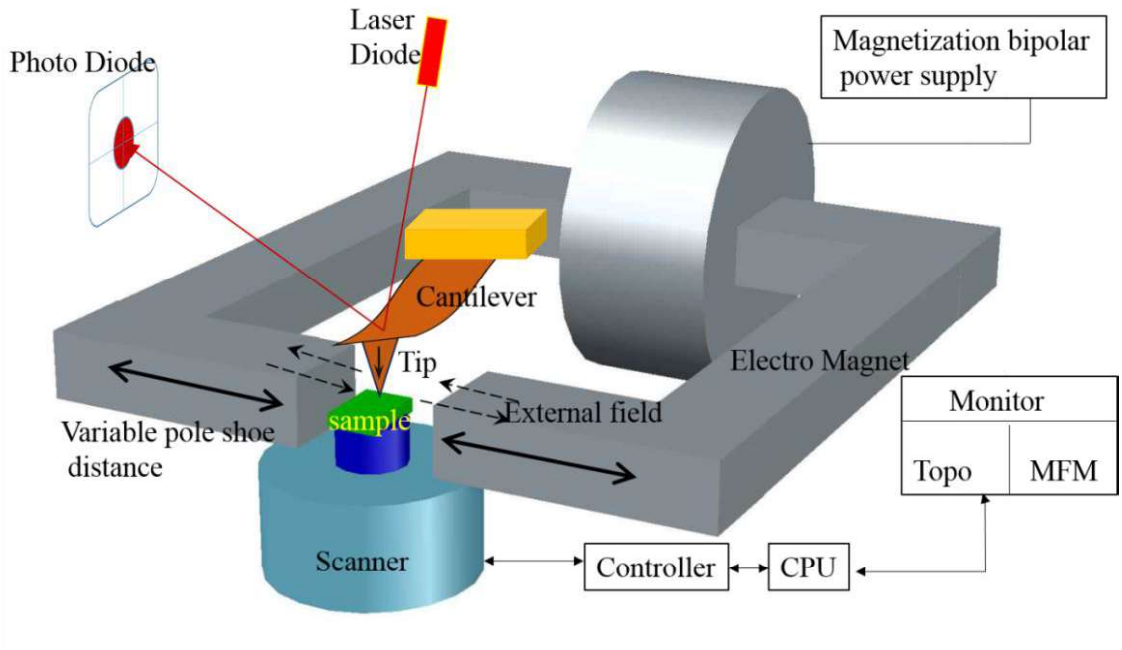

Figure 3.2: Schematic of the experimental setup for MFM imaging in presence of externally applied in-plane magnetic field.

3.2.1 Cantilevers used in the present study

It is well known that ferromagnetic coated cantilevers are used for MFM studies because of their ability to interact with the stray field of the magnetic specimens. The tip radius is slightly larger than that of the normal AFM probes due to the additional magnetic coating. MFM studies in presence of high external magnetic field strength demand MFM tips to be coated with corresponding higher coercivity magnetic material to assure reliable magnetic imaging of the specimen surface [80]. The MFM cantilevers having spring constant of about 2-3 N/m and tips coated with high coercivity Co-alloy (~2 kOe) were used. The first free resonance frequencies were in the range of 60-65 kHz, the tip radius was about 40 nm and the cantilever dimensions were 225 × 35 × 2.5 μm^3, as mentioned by the manufacturer (NT-MDT).

3.2.2 NOVA© software

NOVA© control program is intended to operate instruments manufactured by NT-MDT. It can be used to perform various tasks such as adjusting the optical systems (aiming), control the approach mechanism (landing), acquire and process the frequency responses, acquisition of AFM topography and MFM phase maps, process the images obtained from the instrument, obtain Force–Distance curves, perform lithography operations and control over electromagnetic operations. Figure 3.3 shows the screenshot of the NOVA© software. NOVA© also provides possibility of writing own scripts for performing specific tasks using NOVA© power script. A few important parameters in AFM control are given below:

Magnitude (Mag): It is the magnitude of vibration of the cantilever.

Deflection (DFL): It is the deflection signal of the cantilever.

Setpoint (SP): It is actually a measure of the force that is applied by the tip on to the sample surface and maintained by the feedback loop during measurement in contact mode. SP for semi contact AFM topography imaging is approximately kept as half of the magnitude of the cantilever vibration before landing.

Feedback: The deflection of the cantilever and magnitude of the cantilever oscillations are maintained by the Feedback in contact and semi-contact modes, respectively. Feedback aids to obtain images with uniform tip-sample surface distance during the AFM imaging. Feedback loop consists of a tube scanner which monitors the height of the tip and the optical lever. For a good AFM system, a very well-constructed feedback loop is vital.

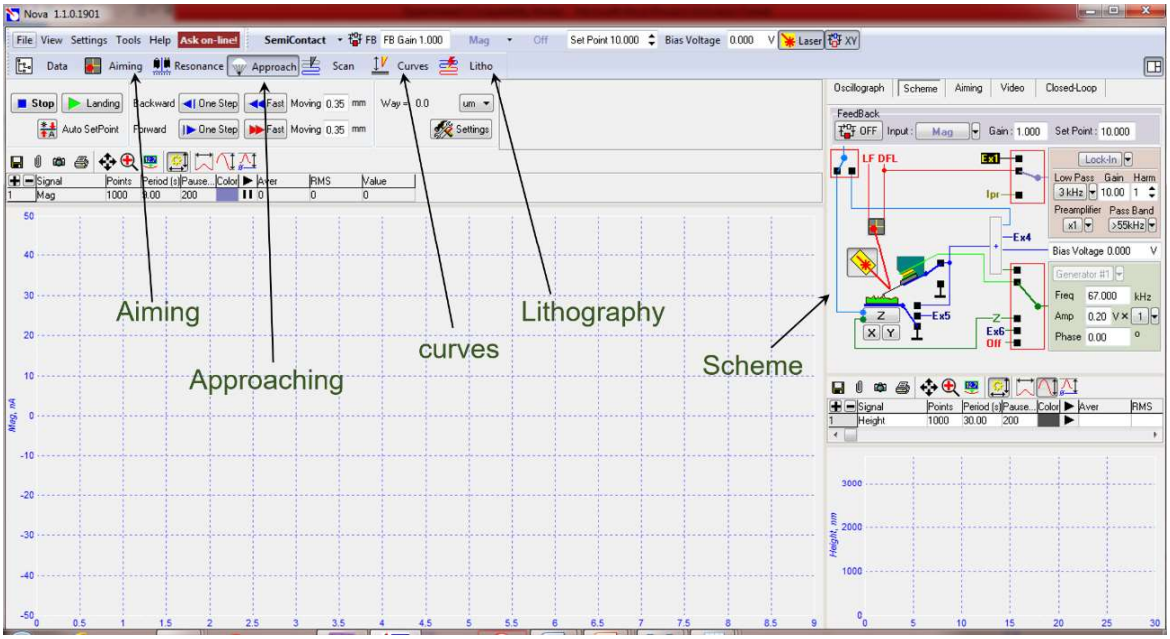

Figure 3.3: Screenshot of NOVA© software

3.2.2.1 Image processing in NOVA© software.

Along with the useful information, AFM/MFM images also contain a lot of artifacts affecting the data and leading to image distortions. Probable distortions in AFM/MFM images are caused by imperfection of the equipment and by external parasitic influences such as constant components, constant inclination, hardware noises, scanner imperfection, instability in tip sample contact and external vibrational noises [136]. The artifacts can be removed by the image processing options in the NOVA© software such as peak removal to eliminate spurious peaks, line correction to eliminate the variation in the line by line data and average plane subtraction to eliminate the inclination. Figure 3.4 illustrates the different processes of eliminating distortions and final quarter shows the appropriate AFM image. Various image correction tools are also indicated on the right-side column in Fig. 3.4

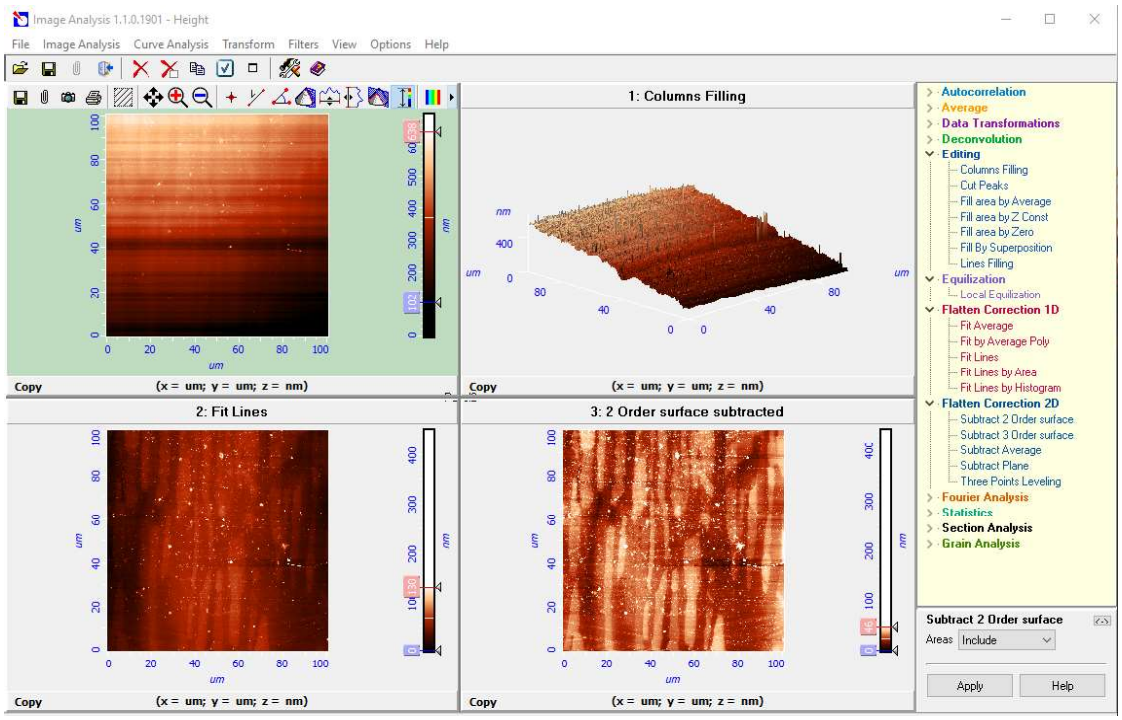

Figure 3.4: Screenshot of processing of topography image in NOVA© at different stages.

3.2.3 MFM imaging

MFM is a semi-contact mode two pass technique in the scanning probe microscopy (SPM) methods. In the first pass, topography of the surface is acquired in tapping mode raster scanning, where the short range (less than 10 nm) Van der Waals interaction acts between the specimen surface and the probe. In the second pass, the probe in resonance, traces the identical path as first pass, with a small z-offset (lift scan) to sense the long range magnetic interaction with very low or no effect of Van der Waals force. The resonance frequency and phase of the cantilever vibration are influenced by the interaction between the out-of-plane magnetic stray field of the sample surface and the tip magnetization. This interaction is effective in the range of 10 to 100 nm [97].

The resonance frequency map can provide quantitative information about the out-of-plane stray field on the surface of the specimen, if the magnetic moment of the tip is known. The phase map can provide qualitative information about the variations in the

out-of-plane stray field along the specimen surface and hence can also be used effectively to map the different domains magnetized differently in the surface microstructure. In the present investigation, the phase change is used to study the local magnetic microstructure in the specimens.

The change in phase (ϕ) of an oscillating cantilever is related to the rate of change in magneto static force (F) with the space between the sample surface and the cantilever tip (z) as given below [77]

$$\Delta\phi \approx \frac{Q}{k}\frac{\partial F}{\partial z} \tag{3.1}$$

where, Q and k are quality factor and spring constant of the cantilever, respectively. The magneto static force F is given as [137]

$$F = m_z \frac{\partial H_{sam}}{\partial z} \tag{3.2}$$

where, m_z and H_{sam} are magnetic moment of the cantilever tip and the magnetic stray field of the sample, respectively. It can be seen in equation 1 that with increasing repulsion between the tip and the sample, the phase value increases and vice versa. The increase in the repulsion indicates the increase in stray field out of sample surface in the present tip magnetization (downwards) condition.

3.2.3.1 Optimization of lift-off height in MFM imaging

Magnetic imaging resolution is affected by the combination of many factors, such as the properties of the tip including mechanical geometry and magnetic structure, tip-sample distance (lift-off), instrument sensitivity and the background noise level. In general, the system and environmental conditions including mechanical, electrical and acoustic noises are related to the vertical resolution; while the tip shape and tip-sample distance affect the lateral resolution mostly. Sharper tips provide better spatial resolution.

The lift-off distance during the second pass imaging drastically affects the image quality. Figure 3.5 shows the effect of lift-off distance on the image quality of phase map obtained on the cold worked 304 stainless steel specimen. A continuous reduction in the phase range can be observed with increasing lift-off distance from 30 to 100 nm in Figs. 3.5 a-d, respectively. The reduction in the phase range indicates the loss of sensitivity. This can be quantitatively seen in Fig. 3.6 as decreasing phase contrast with increasing lift-off distance. However, at small lift-off distances of 30 and 40 nm (Figs. 3.5 a and b), intermittent streaking are observed in presence of any sharp topography feature. Hence, an optimum lift-off distance of 50 nm has been used for MFM imaging on 304 stainless steel specimens with 10 x 10 μm^2 scan area. The optimum lift-off distance is also influenced by the scanning speed. Faster the speed, more should be the lift-off distance to avoid streaking. In case of larger scan area, the linear scan speed is usually higher. Hence, higher value of lift-off of about 80 nm was found to be optimum for MFM imaging on iron and DSS samples with about 50 x 50 μm^2 scan area.

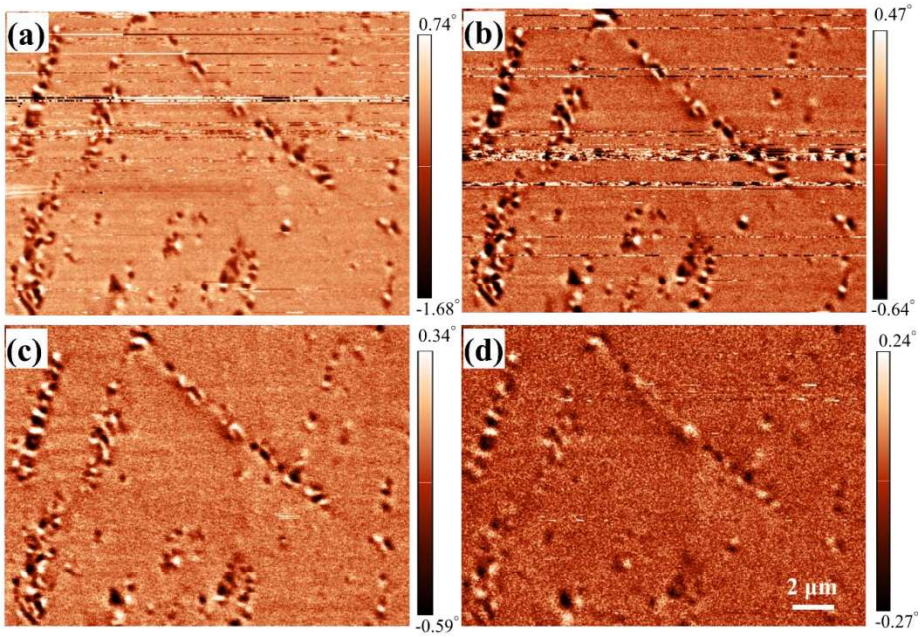

Figure 3.5: MFM phase maps of AISI type 304 austenitic stainless steel obtained with different offset heights of (a) 30 nm, (b) 40 nm, (c) 50 nm and (d) 100 nm.

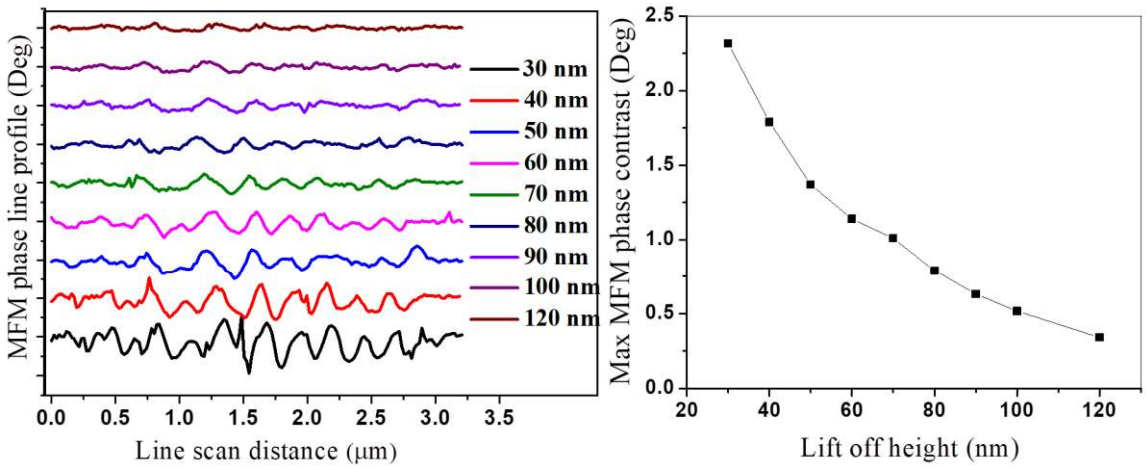

Figure 3.6: Influence of lift-off height on MFM phase contrast (a) MFM phase signal obtained for the same scan line at different lift off height and (b) Variation in MFM phase contrast with lift off height.

3.2.4 *MFM imaging in presence of external magnetic field and stability of the cantilever*

Before performing the detailed study on the influence of external magnetic field on the domain structure, it is required to ensure the stability of the tip in the range of magnetic field being studied. While scanning the tip-sample distance was fixed and the feedback kept ON. Typical magnetic domain structures in the iron specimen obtained in presence of decreasing external magnetic field from +2000 Oe to -1800 Oe are shown in Figs. 3.7 a-c, respectively. The spike magnetic domain with the phase contrast of about 1° was observed in presence of +2000 Oe external field. The phase contrast reduced to about 0.7° upon removal of the field (Fig. 3.7b) and increased again with increasing field value in the negative direction (Fig. 3.7c). A gradual systematic increase / decrease in the domains sizes can be observed in Fig. 3.7 during the magnetization reversal process. However, no specific change in the domain contrast is observed during the complete magnetization cycle indicating the stability of the tip's magnetization in the range of the applied field.

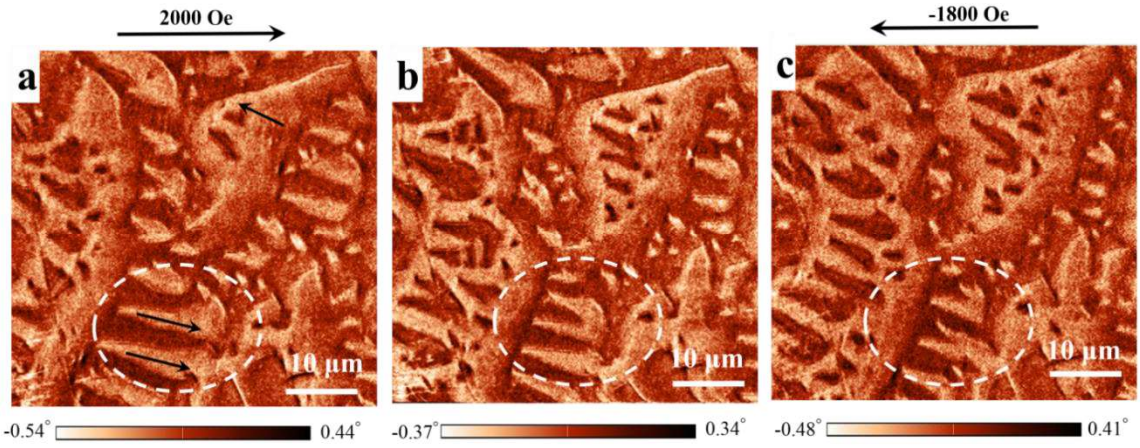

Figure 3.7: MFM phase map in bulk iron specimen (a) in presence of 2000 Oe in-plane magnetic field (b) without field and (c) with field of -1800 Oe. (arrow marks denotes the field directions).

3.3 MATERIALS AND SAMPLE PREPARATION

Figure 3.8 shows the typical microstructures of the samples selected for the present study. They are having distinct structure of magnetic phases and precipitates. The bulk iron is a complete ferromagnetic material. The sample was heat treated at 1373 K for 4 hours followed by furnace cooling to relieve internal stresses. It has an average grain size of around 80 µm. The DSS 2205 sample contains almost equal amount of austenite phase in the ferrite matrix. The cold worked AISI 304 stainless steel contains strain induced fine lamellae and dot shaped martensite phases on the specimen surface. Table 3.1 shows the chemical compositions of the three samples used in the present study.

Table 3.1: Chemical composition of the materials selected in the present study in wt %.

Elements	Cr	Ni	Mn	Mo	Si	P	V	Cu	Fe
Pure Fe	-	-	-	-	-	-	-	-	99.99
DSS 2205	21.79	5.17	1.49	2.91	0.42	0.15	0.16	0.22	Bal
304 AUSS	18.32	9.26	1.63	0.25	0.35	0.34	0.1	0.21	Bal

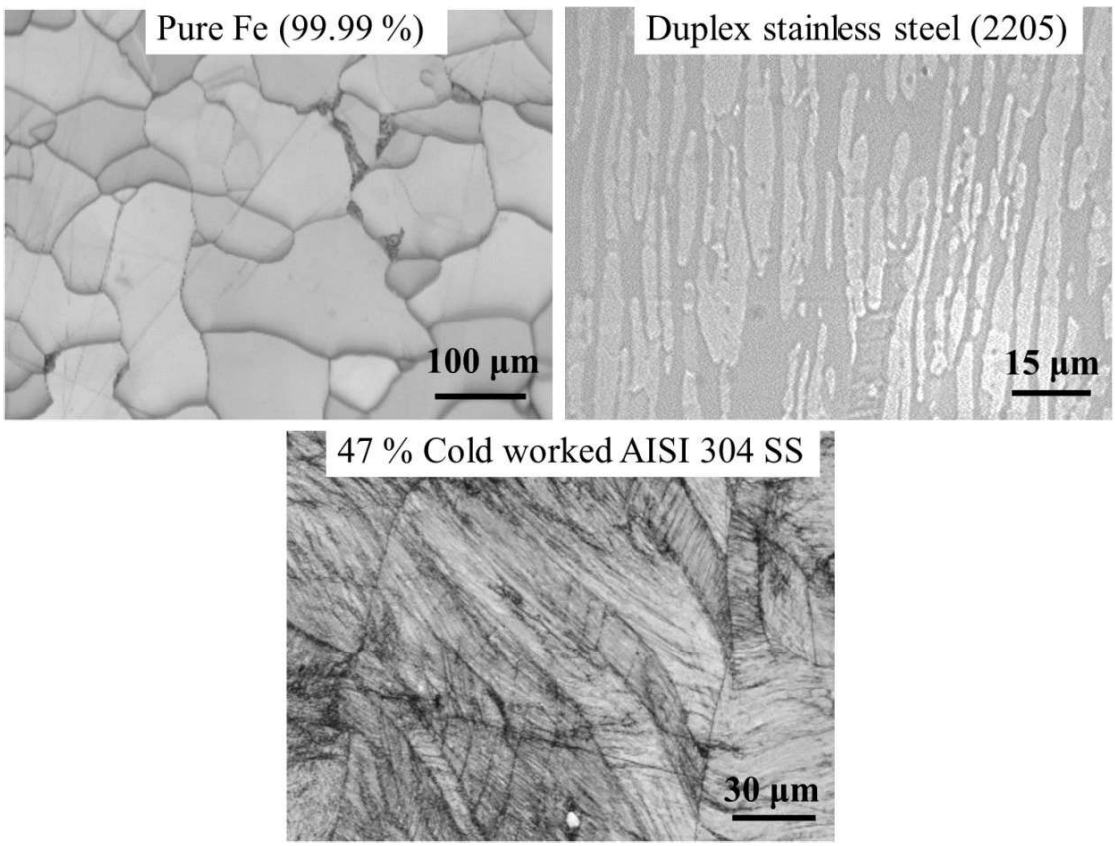

Figure 3.8: Microstructure of the three samples studied in the dissertation.

The samples used in the thesis were first polished up to 1000 grit size SiC emery paper using an automatic polishing machine. Then diamond suspensions of 6, 3, 1 and 0.25 micron were used systematically to obtain a decent mirror polish. In order to remove the debris from the preceding polish, the samples were cleaned thoroughly after each and every polish. Polishing time was about 300 to 1000 seconds at every stage. To obtain, fine mirror finish and to maintain surface roughness below 5 nm, colloidal silica polishing (a combination of mechanical and chemical polishing) was used. It also helps to produce strain free surfaces after polishing. Colloidal silica contains typical particle sizes of < 70 nm which can maintain a surface roughness < 5 nm depending on the polishing time. Durations of 1000 to 2000 seconds for colloidal silica polishing was used depending on

the material. Micro-hardness indents, as shown in Figure 3.9, were intentionally made on the specimen surface to enable easy identification of reference locations.

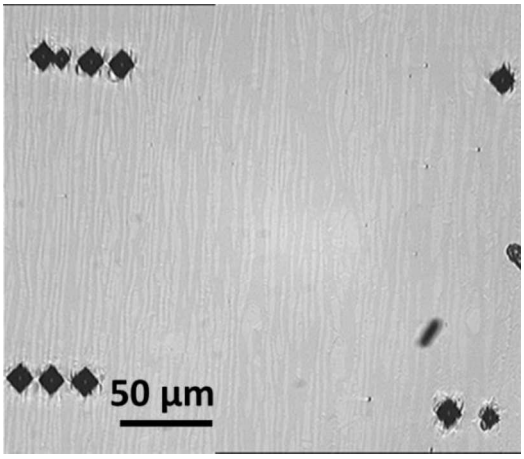

Figure 3.9: Optical micrograph of the DSS 2205 specimen with micro indents for location identification.

3.4 ELECTRON BACKSCATTER DIFFRACTION (EBSD)

EBSD study was performed using a Zeiss SUPRA 55 Gemini field emission gun SEM at an accelerating voltage of 20 kV, an aperture of 60 µm and a working distance of 12 mm, to obtain the crystallographic orientations to correlate with the magnetic microstructure obtained with MFM.

3.5 SUMMARY

The details of MFM experimental setup equipped with externally applied magnetic field is presented. The optimization of lift-off distance for the second pass during MFM imaging is discussed for the specimens used in the present study. The magnetic stability of the tip in the range of external applied field (±1800 Oe) used in the present study is demonstrated. The chemical composition and details of thermo-mechanical treatment and microstructure of the specimens used in the present study are also presented.

MFM STUDIES IN BULK POLYCRYSTALLINE IRON

4

4.1 INTRODUCTION

The magnetization behaviour of a ferromagnetic material is governed by the characteristics of the magnetic domains and their dynamics. Magnetic domain imaging provides the most direct access to the effective magnetic properties from macro to nano scale for fundamental and application point of views [25, 41]. Various studies have been performed to directly visualize the magnetic domains and their dynamics in different materials using magnetic imaging techniques as discussed in Chapter 2. In the present chapter, MFM has been employed to image the domain structure in a pure iron specimen. The bulk polycrystalline iron contains grains oriented in arbitrary crystallographic directions. Hence, magnetocrystalline anisotropic effect on the domain structure can be characterized with the support of electron backscatter diffraction (EBSD) technique. The distinct variations in magnetic domain structure are expected based on the crystallographic orientation of the grain surface normal with respect to the cube axis *i.e.* the easy axis of magnetization.

Further, the chapter discuss the visualization of the local magnetization behaviour *in-situ* by MFM in presence of external magnetic field in the range of -2000 to 2000 Oe. Various micro-magnetization phenomena such as reversible and irreversible domain wall movements, expansion and contraction of domains, Barkhausen jump, bowing of a pinned domain wall and nucleation of a spike domain are visualized. The respective changes in the magnetic microstructure are compared with the bulk magnetization obtained using

vibrating sample magnetometer. Bowing of a domain wall, pinned at two points, upon application of magnetic field is used to estimate the domain wall energy density. The external field applied in two perpendicular directions is used to reveal the influence of the crystalline anisotropy on the local micro-magnetization.

4.2 RESULTS AND DISCUSSION

At first, MFM has been used to image magnetic domains on the surface of randomly oriented grains in the polycrystalline iron sample. The obtained MFM phase maps show clear differences in the domain patterns in different grains as shown in Fig. 4.1 a-d. However, the crystallographic orientations of the grains are required to be known to properly understand the features in the MFM phase maps. Further the direction of in-plane magnetization of the domains can only be revealed by studying its response against the application of external in-plane magnetic field. Hence, both MFM in presence of in-plane magnetic field and EBSD studies have been performed at the same locations of the sample and the results are discussed in this section.

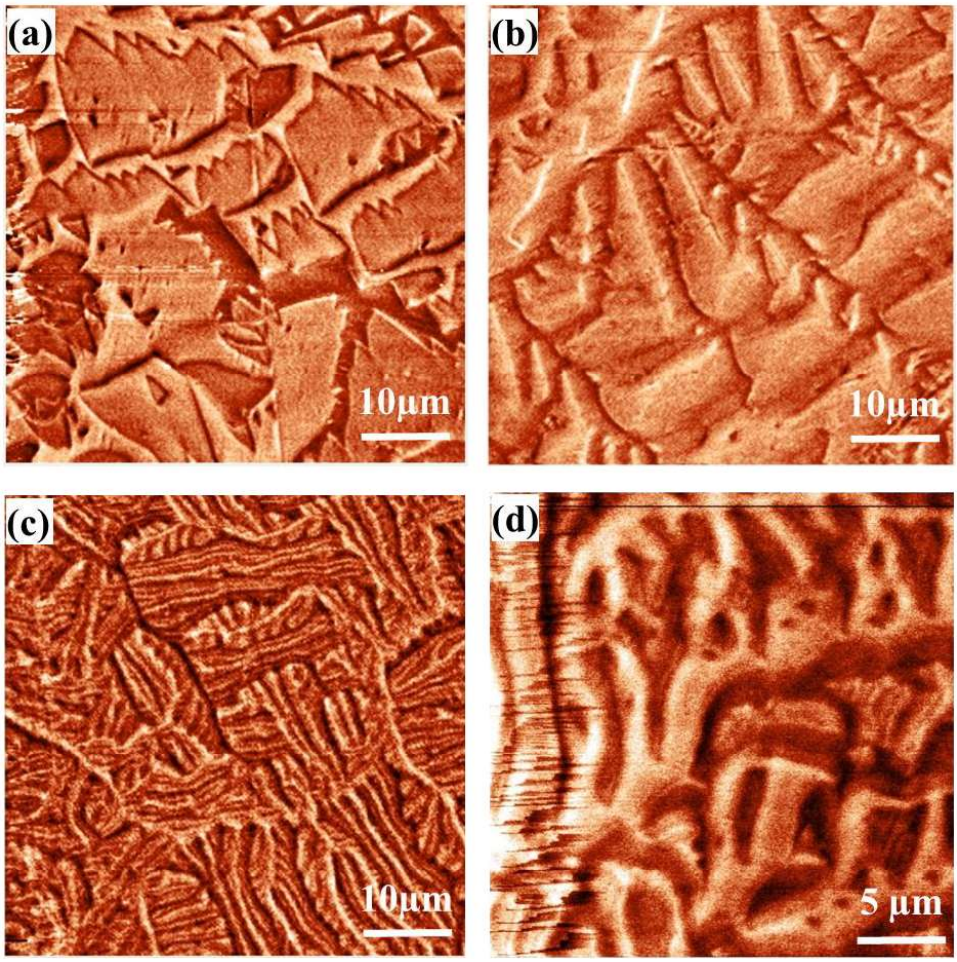

Figure 4.1: MFM phase maps obtained in different grains of bulk polycrystalline iron. The MFM phase ranges for (a) – (d) are [0.81°], [0.84°], [0.85°] and [0.61°] respectively.

4.2.1 Role of crystalline anisotropy on magnetic domain structure

In this section, the influence of crystallographic orientation on the magnetic structure is studied in the polycrystalline iron specimen in the demagnetized state.

4.2.1.1 Grain orientation in the selected region

Figures 4.2 a-c show the inverse pole figure (IPF) maps of an area of 600 x 450 μm^2 on the surface of the iron specimen for X_0, Y_0 and Z_0 directions, respectively. The directions are shown schematically in Fig. 4.2d. About 30 grains with random orientations can be seen in the selected area with the average grain size of about 80 μm.

The grains with orientations close to {100}, {110} and {111} planes parallel to the sample surface were selected to study the effect of crystallographic orientation on the domain structure.

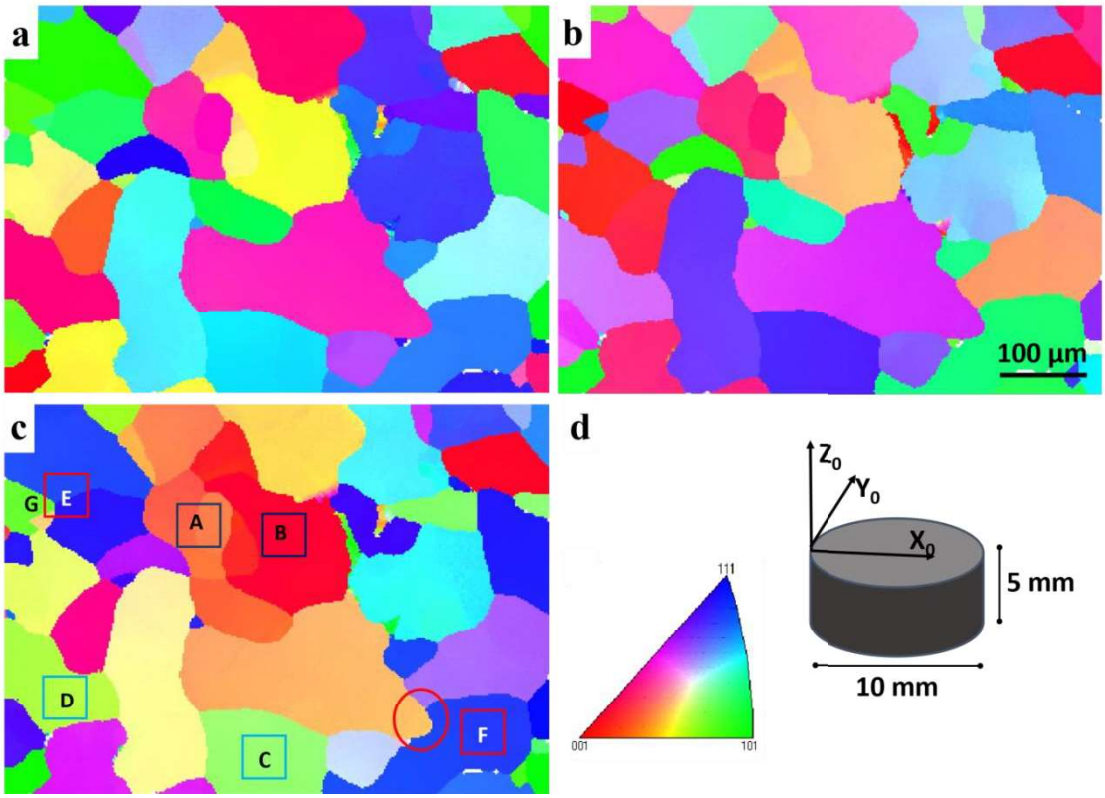

Figure 4.2: Inverse pole figure maps of the polycrystalline iron specimen in (a) X_0, (b) Y_0 and (c) Z_0 directions of the sample as shown schematically in (d).

4.2.1.2 Influence of grain orientation on the domain strucuture

The MFM images were obtained after demagnetization within the minor loops in the range of ±2000 Oe. The domain structures in the grains marked as *A*-*F* in Fig. 4.2c are shown in Figs. 4.3 a-f, respectively and the inset shows 3D grain orientation. The surface of the grains indicated as *A* and *B*, *C* and *D*, and *E* and *F* are oriented close to {100}, {110} and {111}, respectively, as shown in the IPF map corresponding to the normal (Z_0) direction (Fig. 4.2c). The MFM images exhibit contrast corresponding to the domain walls and a feable contrast is only observed between different domains. This indicates that the domains are essentially aligned parallel to the surface plane.

The grains with surface parallel close to {100} (Figs. 4.3 a and b) exhibited domains aligned in two perpendicular directions. The grains with surface parallel to {110} (Figs. 4.3 c and d) exhibited domains essentially aligned in one direction. This is in line with the domain structures reported in grain-oriented and non-oriented electric steels [110, 111]. However, the grains with surface parallel to {111} crystallographic plane exhibited fine and complex maze type domains. These observations can be explained based on the magneto crystallographic anisotropy in iron with body centered cubic (BCC) structure. The easy magnetization direction of the BCC iron is <100>, both the opposite directions are magnetically equivalent in the easy magnetization direction. In order to have at least one easy magnetization direction lying in a plane, by the Weiss zone law, any one of the plane indices {*hkl*} should be zero; and for two perpendicular easy directions to be present, two of the indices must be zero. Hence, the grains with surface parllel to {100} and {110} are expected to have two and one easy magnetization directions [25], respectively, lying on the surface plane. With two easy magnetization directions lying on the {100} plane, domains aligned in two perpendicular directions are expected, as observed in Figs. 4.3 a and b. For the grains with surface parallel to {110}, domains aligned in only one direction parallel to the easy axis are expected, as seen in Figs. 4.3 c and d. In the grains with surface parallel to {111}, no easy magnetization direction can lie on the surface. In this case, a fine complex maze type domain is observed. due to branching of the surface domains to minimize the magnetostatic energy [2], as observed in Figs. 4.3 e and f. The study cleary indicates that the grains with specific orientations exhibit particular domain structure on the surface depending upon its orientation with respect to the easy magnetization direction.

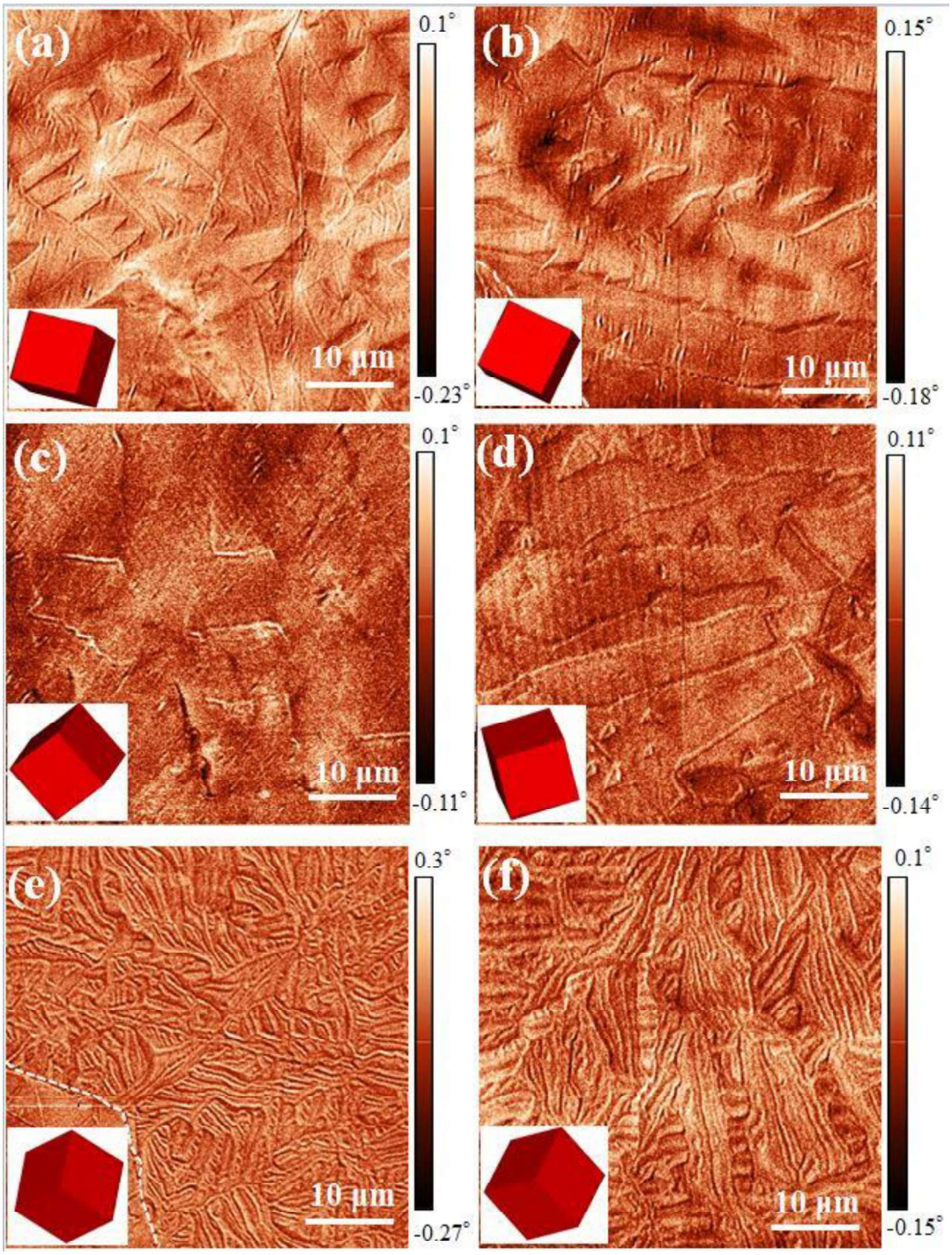

Figure 4.3: MFM phase maps obtained in iron specimen for grains with surface parallel to (a) and (b) {100};(c) and (d) {110}; and (e) and (f) {111}. The grains are marked as A-F in Fig. 4.2c, respectively. Insets indicates the respective grain orientations.

4.2.2 MFM imaging of evolution of magnetic microstructure with applied field

4.2.2.1 Magnetization curve of the bulk polycrystalline iron

Figure 4.4 shows the hysteresis curve obtained for the polycrystalline iron specimen. The field required for complete saturation is ~ 15 kOe and the saturation magnetization is about 2 T. The bulk magnetization measurement has shown negligible value of coercivity as the pure bulk polycrystalline iron specimen is magnetically very soft. The low coercivity (around 20 Oe) value of the iron values are in excellent agreement with those reported in literature for pure iron [33, 105, 138].

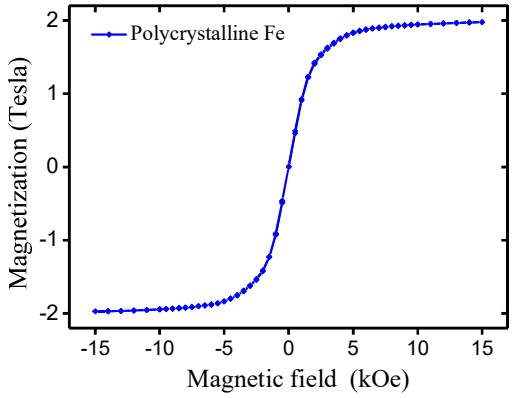

Figure 4.4: Magnetization curve for polycrystalline iron.

Before performing the detailed study on the influence of applied magnetic field on the domain structure, it is required to ensure the stability of the tip in the range of magnetic field being studied. The details of the tip stability and the MFM phase image reliability were discussed in the section 3.2.6. Figure 3.7 depicts the lancet type domain structure which shows the particular grain may have two easy axes of magnetization. The orientations of all the lancet type spike domains are observed to be almost parallel to the horizontal direction indicating the easy axis <100> to be aligned in this direction. With decreasing magnetic field from +2000 Oe to -1800 Oe, the length of the domains in the white encircled region (Fig. 3.7) decreased. Based on this, the spin orientations within the domain are indicated by black arrows in Fig. 3.7.

A systematic increase/ decrease in the size and nucleation/ annihilation of domains can be visualized with decreasing field. However, no sudden change in the phase contrast was observed for any domain confirming the magnetic stability of the tip in the range of external magnetic field applied in the present investigation. Even though a systematic change in the domain structure is observed with changing field, the complete magnetic saturation is not observed in the MFM images at the maximum field applied in the present study. This is in agreement with the bulk average magnetization curve obtained by the vibrating sample magnetometer, which indicates that the field required for complete saturation is about 1 Tesla (Fig. 4.4). Further, as each grain is big in size, the local MH loop measurements with magneto-optic Kerr effect can also provide qualitative information about the magnetic anisotropy.

4.2.2.2 Observation of micro-magnetization events

A detailed analysis of the evolution of magnetic structure with applied field is studied for the area encircled in Fig. 4.2c. Figure 4.5a shows the MFM phase map in the demagnetized condition. The selected area comprises of three grains marked as (I)-(III) in Fig. 4.5a. The grain boundaries are highlighted as white dotted lines for clear visualization. It can be seen in the IPF map corresponding to Z_0 (sample normal) direction (Fig. 4.2c) that the surface normal of grain I has orientation between <100> and <110>. The surface normal of grain II is oriented between <100> and <111>, whereas, grain III is oriented parallel to {111} plane. This is clearly reflected in terms of increasing complexity of the magnetic microstructure from grain I to grain III, as seen in Fig. 4.5a. These observations are in line with those described in the earlier section.

Figures 4.5 b-k show the changes in the magnetic microstructure during a minor magnetization loop. The magnetic field is applied along the vertical direction (Y_0 in Fig.4. 2d). The direction of positive field is upwards and the negative field is downwards in the

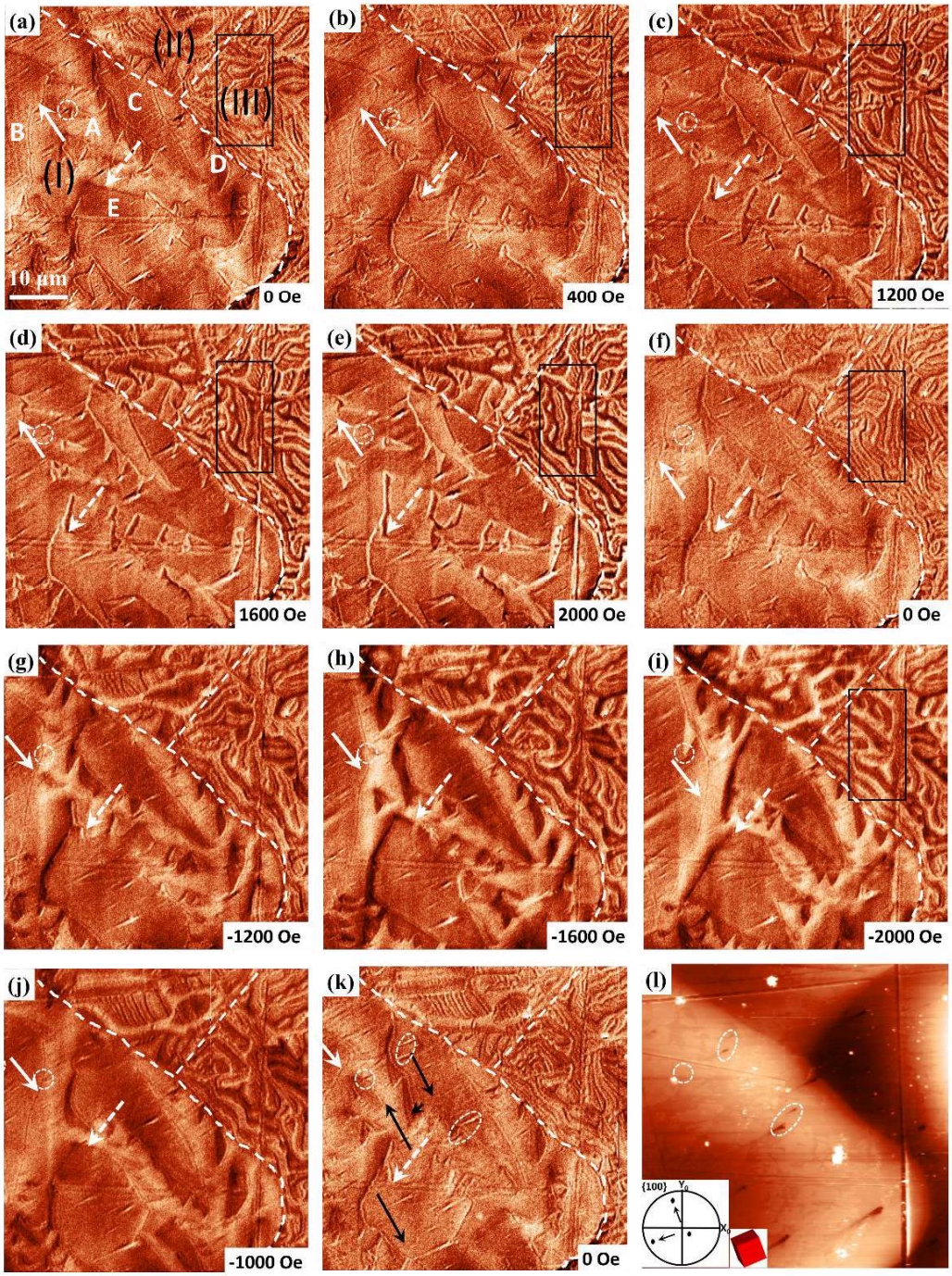

Figure 4.5: MFM phase maps obtained in presence of in-plane magnetic field of (a) 0 Oe [0.27°], (b) 400 Oe [0.27°], (c) 1200 Oe [0.26°], (d) 1600 Oe [0.27°], (e) 2000 Oe [0.28°], (f) 0 Oe [0.3°], (g) -1200 Oe [0.32°], (h) -1600 Oe [0.34°], (i) -2000 Oe [0.36°], (j) -1000 Oe [0.37°] and (k) 0 Oe [0.28°]. Contact mode AFM topography image is shown in (l) and the insets show the pole figure and 3D cube orientation of grain I obtained from EBSD study. The positive direction field is upwards and the negative direction is downwards.

images shown in Fig. 4.5. In spite of the complex domain structure, the influence of the applied field can be visualized is grain III. The fine domains in the area denoted by a rectangle in grain III got aligned in the direction of applied field with increasing field.

Grain I exhibited small phase contrast between different domains, however, the domain walls are associated with sudden phase variations and hence can be clearly identified. This indicate in-plane magnetization in the grain. The contact mode AFM topography image is shown in Fig. 4.5*l*. The insets in Fig. 4.5*l* show the pole figure of grain I and 3D orientation obtained by EBSD. As the orientation of the grain surface is between {100} and {110}, one to two easy magnetization directions are expected to lie close to the plane surface in directions parallel to the arrows shown in Fig. 4.5*l*. These are also indicated by the directions of white arrows in Figs. 4.5 a-k. Different domains exhibiting significant changes are denoted by *A*-*E* in Fig. 4.5a. Several lancet domains oriented parallel to one of the two easy axes can be seen on the boundaries between domains *A* and *C*, domains *A* and *E*, and at the grain boundary. A few lancet domains are also observed within domain *A*. The MFM imaging with application of ± 2000 Oe external field demonstrates various micro-magnetization phenomena in the iron specimen as described below.

The growth of domain *A*, at the expanse of domains *B, C, D* and *E*, with increasing applied field up to +2000 Oe can be clearly visualized in MFM phase maps shown in Figs. 4.5 a-e. Based on the above, the possible magnetization directions of the domains are indicated in Fig. 4.5k. The field dependent domain wall dynamics can be visualized clearly by the movement of domain wall between domains *A* and *B* (indicated by white arrow). The domain wall returned almost to the original position upon the removal of the external field (Fig. 4.5f). With further application of the external field in the negative direction, growth of domain *A* is clearly visualized in Figs. 4.5 g-i. The

domain wall moved in one of the easy magnetization directions by about 7 μm upon application of -2000 Oe as compared to the without field condition. Nucleation of a lancet domain in domain *B* at its wall with domain *A* can be visualized in Fig. 4.5i upon application of -2000 Oe. The nucleation of the lancet domain is associated with formation of a kink at the wall to overcome a pinning site. The nucleated lancet domain is aligned along the easy axis. The locations corresponding to the nucleation point of the lancet domain are shown by circles in all the MFM and topography images. Corresponding to the same location, a lancet domain can also be observed in the MFM images obtained at 0-1200 Oe applied fields (Figs. 4.5 a-c). A small surface defect like feature is clearly observed corresponding to this location in Figs. 4.5 d-f and k. However, the AFM image did not reveal any topography feature at this location. A few other surface defects are observed in the topography image as identified by dotted ellipse in Fig. 4.5*l*. All these surface defects are also revealed in MFM images, as indicated in Fig. 4.5k, with similar appearance as the defect at the location of the lancet domain. The absence of defect feature in the AFM topography image may be attributed to better sensitivity in the MFM imaging due to the stray fields associated with these defects. The hindrance to the movement of domain wall and nucleation of lancet domains at the defect clearly demonstrate the influence of surface defects on the field dependent domain wall dynamics studied on the surface of a specimen. The reduction in the areas of domains *C* and *D* with respect to their area in the demagnetized states are plotted in Figs. 4.6 a and b, respectively, during the minor magnetic loop. With increasing applied field in the positive direction up to 2000 Oe, the area decreased almost linearly by about 60 % (80μm^2) for domain *C*. The linearity was maintained during the reduction in field up to -2000 Oe, indicating reversible domain wall movement.

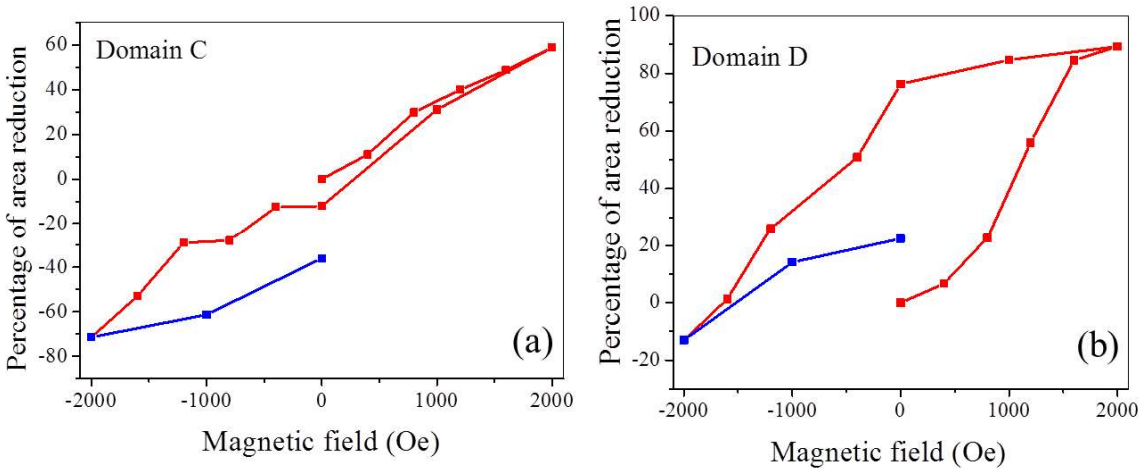

Figure 4.6: Change in the area of (a) domain C and (b) domain D with applied magnetic field. Domains C and D are indicated in Fig. 4.5a.

However, during the decrease in applied field from -2000 Oe to zero, a nonlinear behaviour is observed. On the other hand, domain *D* (a lancet spike domain at the grain boundary) exhibited irreversible domain wall movement with nonlinear hysteresis behaviour with reduction in the domain area by about 90% (6 μm^2) with increasing field to 2000 Oe. The remanence and coercivity effects are also seen clearly for this domain. The coercivity value is found to be about -1600 Oe, corresponding to the same size of the domain observed during reducing field as in the demagnetized state.

4.2.2.3 Bowing of a domain wall

Various magnetization effects can be visualized in a part of the domain wall between domains *A* and *E* marked with the dotted white arrow in Fig. 4.5. In the demagnetized state (Fig. 4.5a), the domain wall is straight, indicating stress free region [105].With the application of 400 Oe in-plane external field in the upward direction, bowing of the domain wall is observed along the direction of white dotted arrow, *i.e.* parallel to one of the easy axes, as the domain wall is pinned between the points separated by about 5.76 μm as seen in Fig. 4.5b. With further increase in the field up to about 1200 Oe, no further movement of the domain wall is observed which indicates the pinning of

the domain wall (Fig. 4.5c). Sudden jump of the domain wall is observed at 1600 Oe (Fig. 4.5d), and slight further bowing is observed at 2000 Oe field. The field induced domain wall dynamics can be clearly visualized in the trace of the domain wall shown in Figs. 4.7 a and b corresponding to increasing field from zero to 2000 Oe and reducing field from 2000 Oe to -1600 Oe, respectively. The variations in bowing distance (x, as indicated in Fig. 4.7c) with applied field are shown in Fig. 4.7d. The sudden jump (bowing) of domain wall at 400 Oe, with no further movement at 800 and 1200 Oe followed by a sudden jump at 1600 Oe are clear manifestations of the pinning effect (defect induced Barkhausen jump). The domain wall pinning happened specifically at two locations at 400 and 1600 Oe (Fig. 4.7a) during the increasing field. At the same locations, pinning of domain wall were observed during the reduction in the applied field also (Fig. 4.7b). This confirmed that the observed domain wall pinning were due to real defects present at those locations.

During decreasing field, no significant change at 1000 to -800 Oe, these images were not shown in Fig. 4.5. However, the trace of domain wall at 1000 and -800 Oe is shown in Fig. 4.7. After that, sudden reduction in bowing at -1200 Oe and reaching the initial state at -1600 Oe. This clearly shows irreversible movement during bowing of the domain wall. Remanence and coercivity phenomena of the minor loop can be seen clearly in Fig. 4.7. Bowing in the opposite direction is not observed upon application of negative field upto -2000 Oe, as domain *A* is sandwiched between domains *C* and *E* due to their expansion during the application of field in the negative direction (downwards). The coercivity value is found to be about -1600 Oe corresponding to the position of the domain wall as in the demagnetized state. This value is similar to that obtained for domain *D*, as described earlier. The apparent coercivity value of -1600 Oe is very large for pure iron. The coercivity values for pure iron are reported to be in the range of 1 – 10 Oe for bulk samples [1, 2]. For larger domain (domain *C* with ~130 μm^2 area), the

coercivity observed in the present study is in line with those reported earlier. However, the hysteresis observed on the surface in MFM results could be attributed more to the surface phenomena similar to those discussed to explain the higher value of domain wall energy density on the surface. The similar phenomenon is observed in case of thicker film of CoP specimen. In that case, bulk magnetization shows smaller coercivity and remanence as compared to the surface magnetization values [139]. It is evident from the analysis of field induced domain wall dynamics in Fig. 4.5 that depending upon the domain size and surrounding domain structure and microstructure, various domains within the same grain show different behaviour such as irreversible or reversible movement at similar field values.

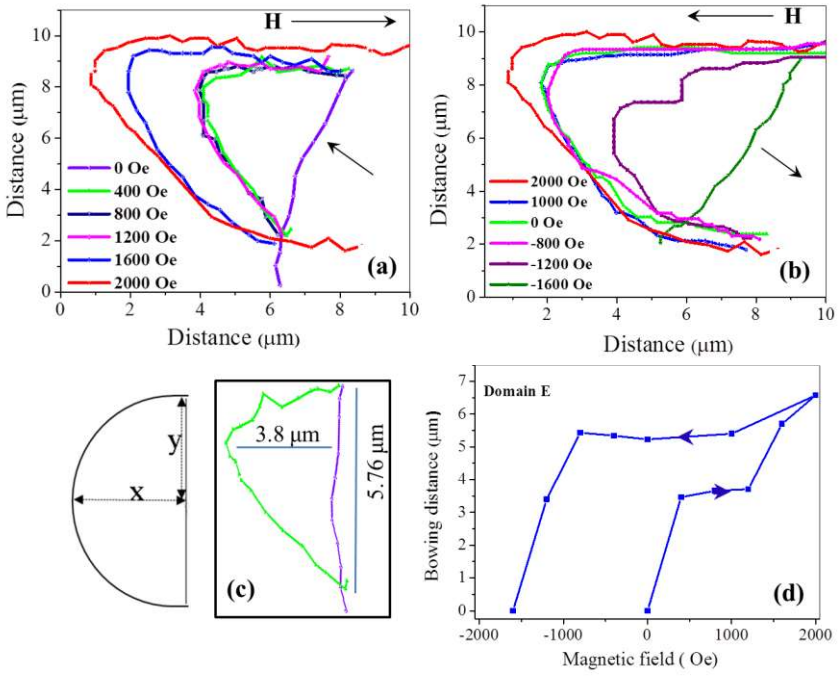

Figure 4.7: Trace of the bowing domain wall (shown in Fig. 4.5) during (a) increasing field from 0-2000 Oe and (b) decreasing field from 2000 Oe to -1600 Oe. The simplified schematic of the domain wall bowing defining the bowing distance *(x)* and distance between pinning points *(2y)* are shown in (c). (d) Shows the variations in bowing distance with applied magnetic field.

The extent of bowing of a domain wall *(x)*, pinned at two points separated by distance *(2y)*, under the influence of an external magnetic field *(H)* is related to the domain wall energy density *(E)* as shown in the simplified equation given below [5]:

$$\frac{x}{H} = \frac{y^2}{2}\frac{M_S}{E}\cos(\theta) \qquad (4.1)$$

The M_S value of 2 Tesla is obtained from Fig. 4.4. The applied field (*H*) of 400 Oe, the *x* value of 3.8 μm and *y* value of 2.88 μm are used (Fig. 4.7d). θ (= 40°) is the angle between the external field and the bowing direction. The value of surface energy density of the domain wall is calculated as 52 mJm^{-2}. The values are even larger if *x* values corresponding to 1600/ 2000 Oe are used. The domain wall energy density value obtained in the present study is higher than that reported for polycrystalline metallic materials (1-8 mJ m^{-2}) [2, 140] and thinfilms (3-15 mJ m^{-2}) [5, 32]. The higher value of domian wall energy density is also attributed to the presence of surface defects contributing to larger hindrance to the movement of surface domain walls. Considering that the hindrance to the movement of domain wall is much less inside the sample, the movement of domain wall is expected to be more inside the sample as compared to that on the surface at the same applied field. This would lead to pulling effect on the domain wall observed on the surface by the overall domain inside the sample.

4.2.2.4 Magnetic anisotropic influence in the micro-magnetization

Various micro-magnetization phenomena could be visualized by the MFM studies in presence of applied field in Grain I (Fig. 4.5a), which surface normal was oriented close to the cube axis with two easy axes of magnetization on the surface parallel to X_0 and Y_0 directions. In order to observe the magnetic anisotropy effect on the local micro-magnetization, another grain (Grain 'G' in Fig. 4.2) with <110> surface normal is selected

which exhibits easy axis of magnetization <001> along Y_0 direction and <110> along X_0 direction, as shown in Fig. 4.2.

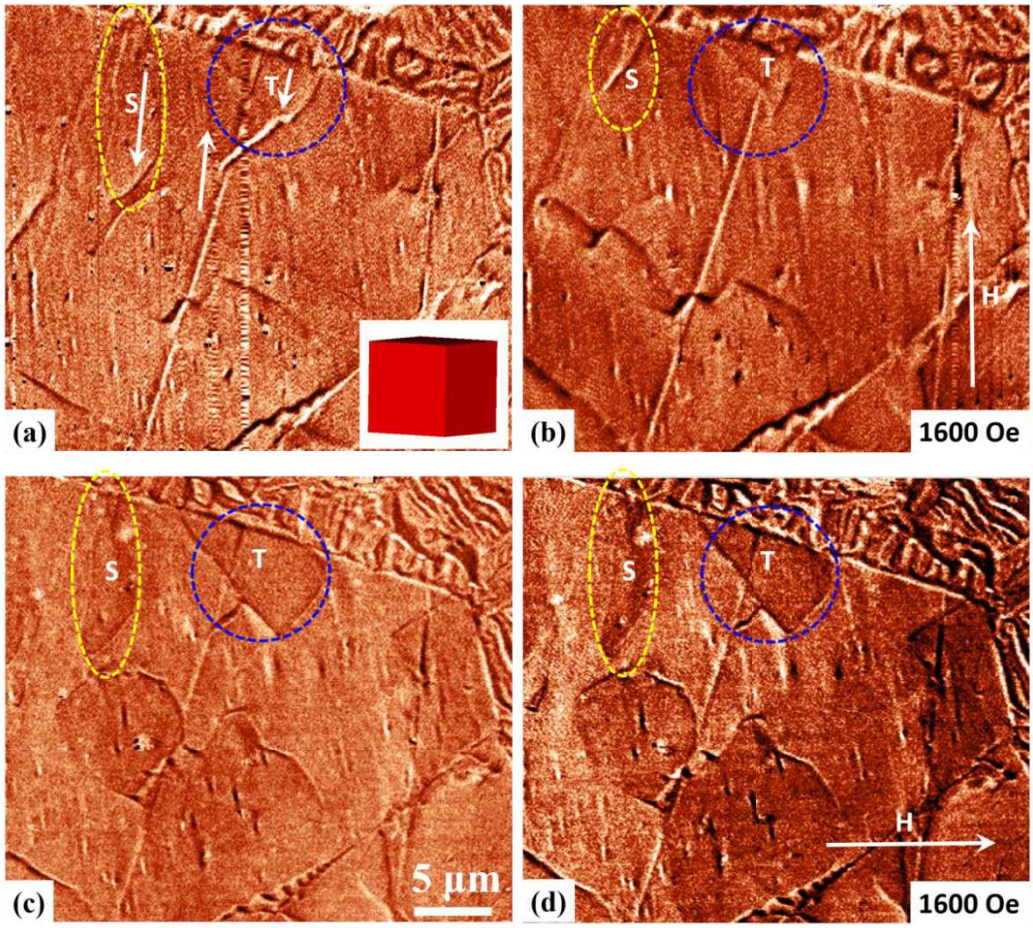

Figure 4.8: MFM phase maps obtained (a) without field and (b) in presence of 1600 Oe field applied in the vertical direction. The specimen was then rotated by 90° after completing one cycle of magnetization. MFM phase maps obtained (c) without and (d) in presence of 1600 Oe field in the horizontal direction. MFM images shown in (c) and (d) are rotated by -90° for direct comparison with (a) and (b). The 3D cube orientation of the grain is shown as inset in (a). The MFM phase range of (a) – (d) are [0.27°].

Figure 4.8a shows the MFM image obtained before the application of external field. The easy axis of magnetization for the grain is in the vertical direction (Y_0) as seen in the 3D orientation shown as inset in Fig. 4.8a. MFM images were obtained at different applied fields in the vertical direction (Y_0/ <001>) in the range of ± 1600 Oe during one magnetization cycle. Figure 4.8b shows the MFM image obtained in presence of 1600 Oe

external field. Reduction in the size of domains (*S* and *T* marked in Fig. 4.8) are clearly observed upon application of the external field. Based on the response of the domains to the external field, the directions of magnetization in different domains are indicated by arrows in Fig. 4.8. The reductions in the area for domains *S* and *T* as functions of the applied field are shown in Figs. 4.9 a and b, respectively. About 90% change in the domain area is observed for Domain *S* upon application of ± 1600 Oe field. Domain *T* exhibited about 40 % reduction in the area upon application of 1600 Oe and about 70% increase in the area upon application of -1600 Oe field. Changes are also observed in other domains in the grain. After completing one cycle of magnetization, the specimen was rotated by 90° and the acquired MFM images were also rotated by -90° for direct comparison with Figs. 4.8a and b. Figure 4.8c shows the MFM image in absence of external field. MFM images were obtained at different applied fields in the horizontal direction (X_0 / <110>) in the range of ± 1600 Oe during one magnetization cycle. Figure 4.8d shows the MFM image obtained in presence of 1600 Oe external field. The reductions in the areas of domains *S* and *T* as functions of the applied field are also shown in Figs. 4.9 a and b, respectively.

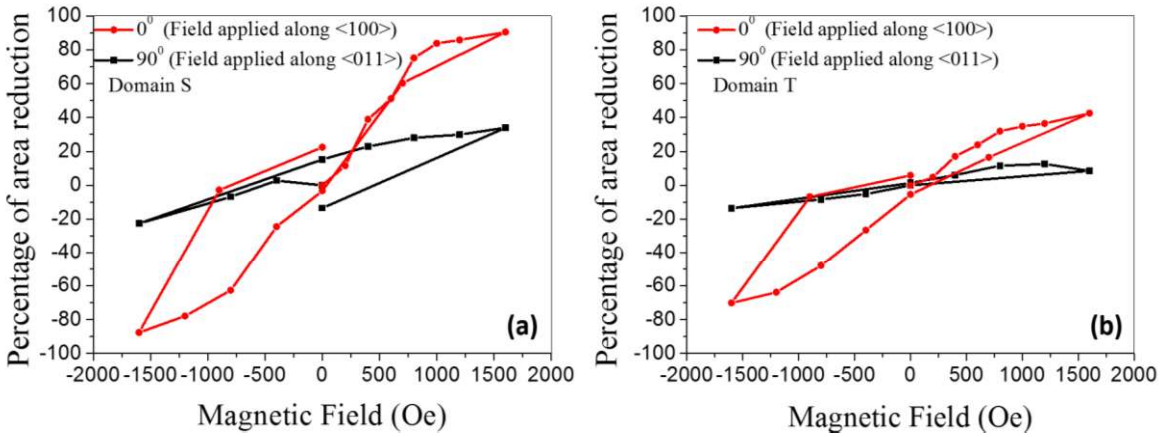

Figure 4.9: Change in the area of (a) domain *S* and (b) domain *T* with applied magnetic field along <100> and <011> direction. Domains *S* and *T* are indicated in Fig. 4.8a.

It can be clearly seen from Figs. 4.8 and 4.9 that the magnetic domain structures changed only marginally with the applied field in <110> direction as compared that in <001> direction *i.e.* along the easy magnetization direction. The field dependent domain dynamics studied in both the grains exhibited that the magnetization essentially progresses with large changes in lancet domains at the grain boundaries. This provides the experimental validation of the influence of grain boundaries on the magnetization process as proposed by Sakamoto et. al [141] and observed through enhanced magnetic Barkhausen emission in smaller grains by many authors [142].

4.3 CONCLUSIONS

The present chapter demonstrates the applicability of MFM in combination with EBSD to study the influence of crystallographic magneto anisotropy on the magnetic microstructure and field dependent domain wall dynamics on the surface of a polycrystalline iron specimen. MFM study in presence of external magnetic field provided clear visualization of various micro-magnetization phenomena such as reversible and irreversible domain wall movements, expansion and contraction of domains, Barkhausen jump, generation of a spike domain, and bowing of a pinned domain wall. The study indicates that depending upon the domain size and surrounding domain structure and microstructure, various domains within the same grain show different behaviour such as irreversible or reversible movement at similar field values. The higher coercivity and surface domain wall energy density values obtained for smaller domains in the present study are attributed to the presence of surface defects.

MFM STUDIES IN DUPLEX MAGNETIC STRUCTURE STEEL 5

5.1 INTRODUCTION

This chapter investigates the local micro-magnetization behaviour in duplex stainless steel (DSS) using MFM. The duplex microstructure of DSS has equal amount of austenite phase in ferrite matrix. The MFM imaging clearly differentiates ferrite phase (ferromagnetic) from the austenite phase (paramagnetic) due to the maze type or complex stripe magnetic domains present in the ferrite phase. The microstructure of DSS helps to study the influence of the interface (grain boundary) The magneto crystalline anisotropic effect on the domain structure is discussed with the support of EBSD measurements. MFM phase contrast and domain width are correlated with the orientation of surface normal with respect to the easy axis of magnetization (<100>). The influence of external magnetic field (±1600 Oe) application on the domain structure is studied as a function of the grain orientation and the leakage field at the grain boundaries is analyzed based on the mis-orientation between the grains.

5.2 RESULTS AND DISCUSSION

5.2.1 Influence of crystallographic orientation on domain structure

5.2.1.1 Domain structure in the three orthogonal planes

The polished and un-etched sample was probed with MFM to obtain the magnetic domain structure. Figure 5.1 depicts the topography and the MFM phase map of the DSS sample. The MFM phase map differentiates the ferrite from the austenite phase. The maze

type and striped domain patterns are observed on the surface of the ferrite phase region, and the paramagnetic austenite phase shows a homogeneous and uniform MFM phase distribution. The magnetic domain structures observed by MFM on the three orthogonal planes of the DSS specimen are shown in Fig. 5.2 as a 3D image. Similar, microstructures obtained with optical microscope (showing distribution of ferrite and austenite phases) have been reported for DSS specimens [114, 143].

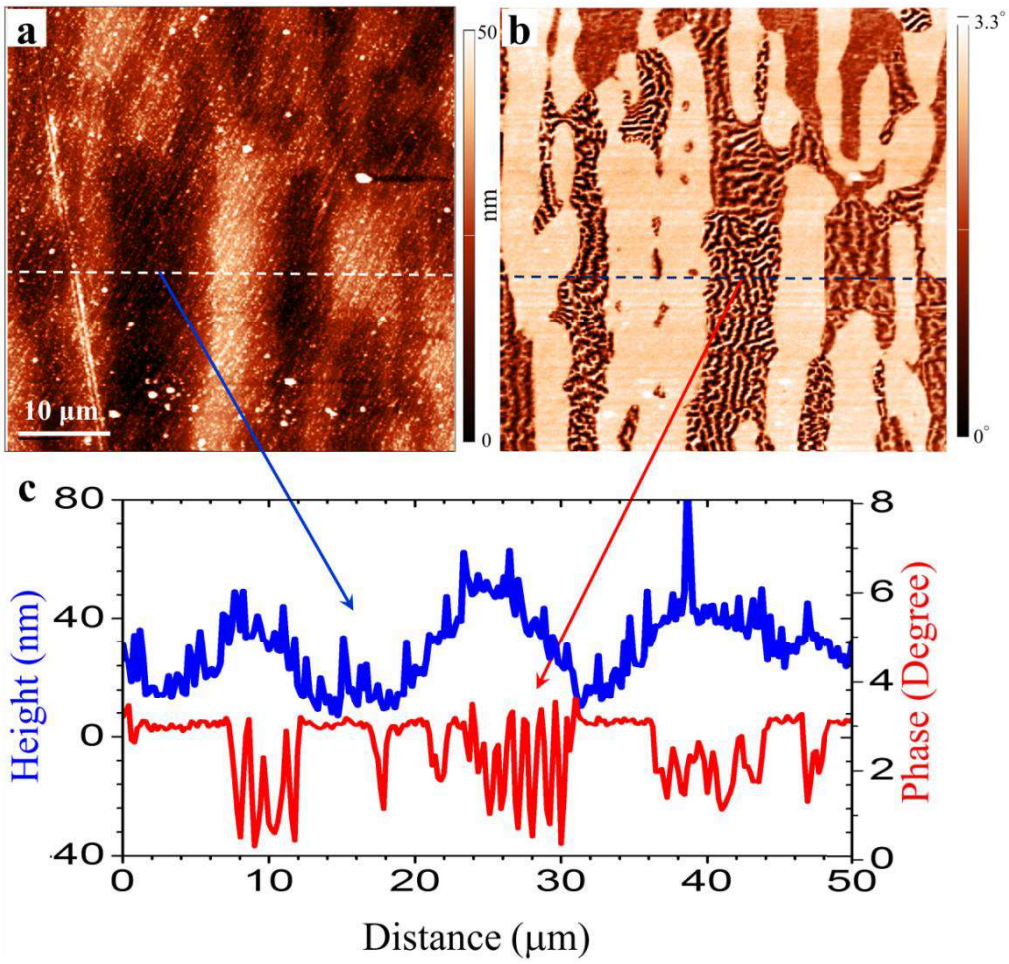

Figure 5.1: (a) AFM topography, (b) MFM phase map and (c) the line profiles of both topography and MFM phase maps obtained on the DSS sample.

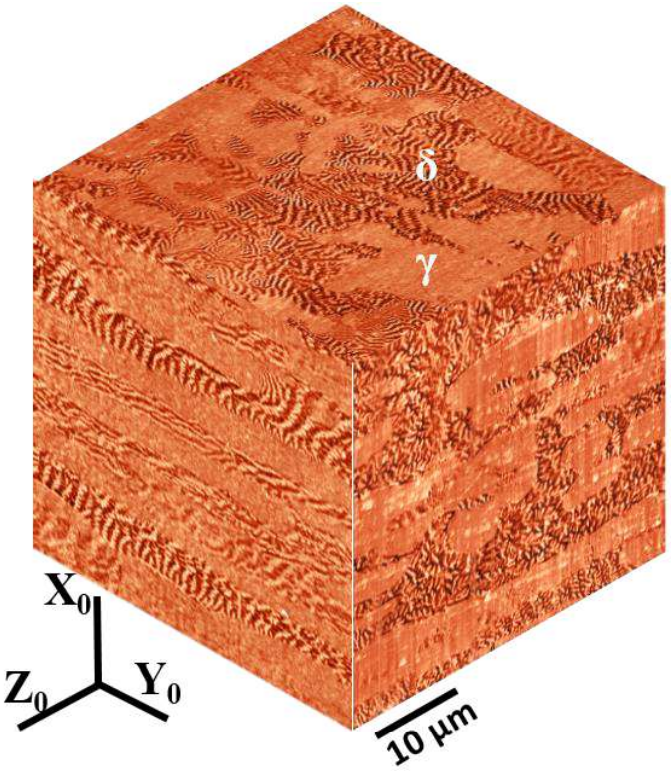

Figure 5.2: 3D magnetic microstructure of DSS sample obtained using MFM, X_0 - Normal direction, Y_0 - Rolling direction and Z_0 -Transverse direction.

The sandwich of elongated ferrite and austenite grain structure are seen in the rolling (Y_0) and transverse sections (Z_0). The microstructure in the normal section (X_0) plane shows austenite grain spread isotropically in the ferrite matrix. The observed magnetic domain structures in the ferrite grains on all the three surfaces of the specimen show similar striped / maze type domain patterns with strong magnetic contrast. In the present study, the detailed analysis of magnetic domain structure is performed on the transverse section (Z_0) of the specimen so that the effect of anisotropic microstructure (elongated grains) on magnetization behaviour could be studied in two perpendicular directions.

5.2.1.2 Grain orientation in the selected regions

Figures 5.3 a and b show the plane normal inverse pole figure (IPF) maps of austenite and ferrite phases, respectively, in an area of 200 × 200 μm^2 on the transverse

section (Z_0) of the specimen. The microstructure consists of two phases with similar frequency of occurrence and the recrystallization fractions for austenite (FCC) and ferrite (BCC) phases are 48.4% and 47.5% respectively. The grains are elongated in the Y_0 direction; however, no preferential crystallographic orientation is observed. The residual stress on the specimen was also measured using XRD technique along the rolling direction (Y_0) in the longitudinal section (X_0Y_0 plane in Fig. 2). Negligible values of -10 ± 30 MPa and -10 ± 25 MPa were observed in the ferritic and austenitic phases. For further detailed analysis of the MFM images and the corresponding crystallographic orientation image maps, the marked region in Fig. 5.3b is selected.

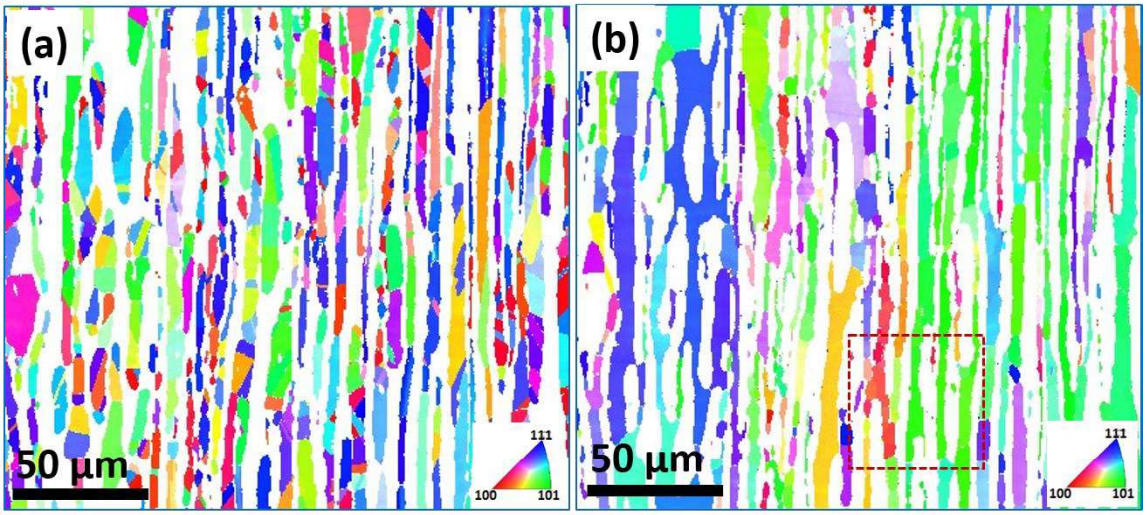

Figure 5.3: Z_0 direction inverse pole figure map of DSS sample for (a) austenite phase and (b) ferrite phase.

5.2.1.3 Influence of grain orientation on MFM contrast and width of domains

Figures 5.4 a-c show the IPF maps of ferrite phases corresponding to X_0, Y_0 and Z_0 directions, respectively, for the selected area of 50 x 50 μm^2 on the DSS surface. Figure 5.4d depicts the MFM image for the corresponding area after minor loop demagnetization (with the range of ±2000 Oe) in the X_0 (horizontal) direction. The bright and dark regions in ferrite phases clearly reveal that the magnetic domains are pointing out of the surface for the bright region and pointing into the surface for the dark region, as

per equation 3.1. Therefore, most of the visualized magnetic domains in the DSS specimen are perpendicularly magnetized to the surface and separated by 180° domain walls.

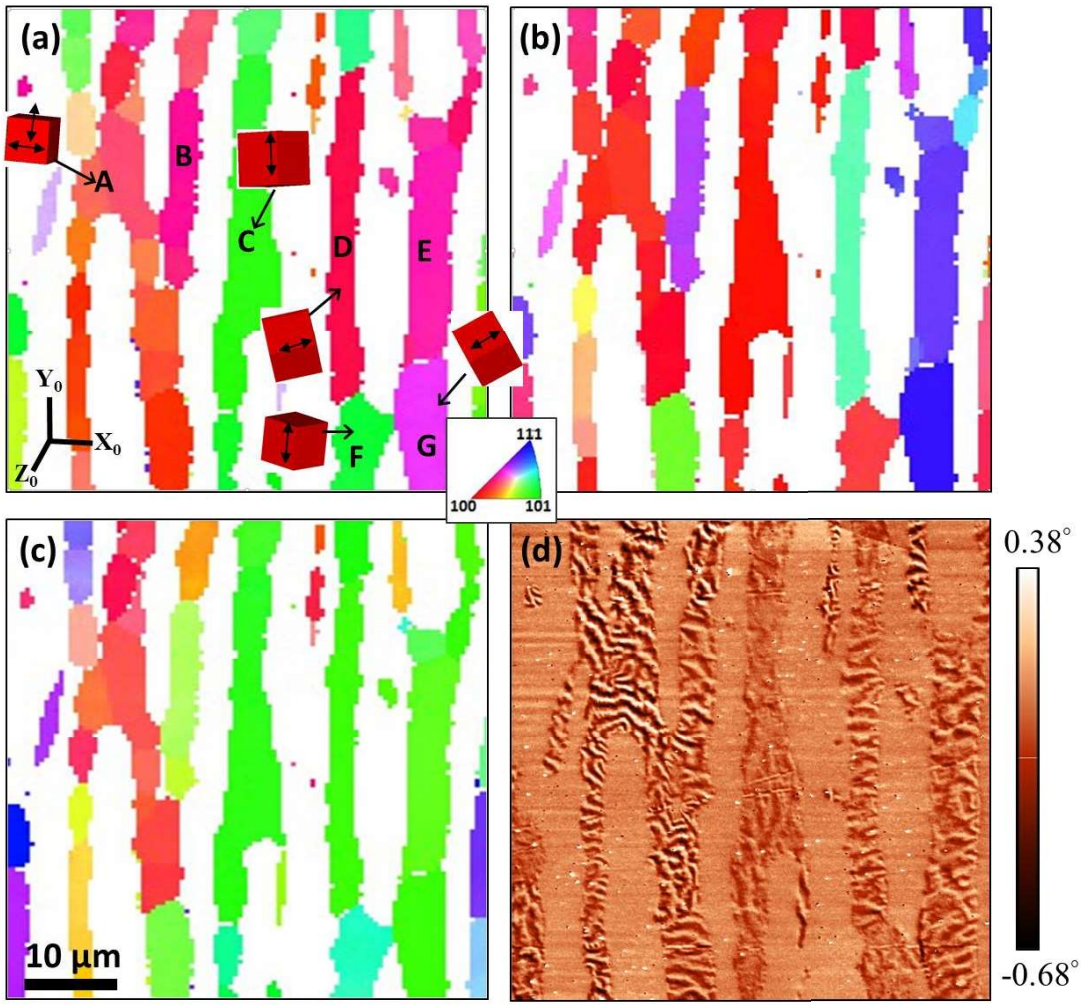

Figure 5.4: (a-c) Inverse pole figure maps of the ferrite phase for the area marked in Fig. 5.3b in X_0, Y_0 and Z_0 directions respectively and (d) the corresponding MFM image with the phase range of 1.06°.

The orientations of grains A, C, D, F and G are shown schematically in Fig. 5.4a. Interestingly, it has been noted that the grain orientation has a close relationship with the MFM phase contrast. Grain A with surface normal along <001> easy axis of magnetization (red in Z_0 IPF) shows a strong MFM contrast as compared to grains B-G with the surface normal along <110> direction (green in Z_0 IPF). In addition to the variations in the MFM phase contrast, the domain widths are also found to be different in

these grains. For better visualization of the effect of crystallographic orientation on the domain structure, the 16 grains observed in Fig. 5.4 are indicated on the IPF corresponding to the surface normal in Figs. 5.5 a and b.

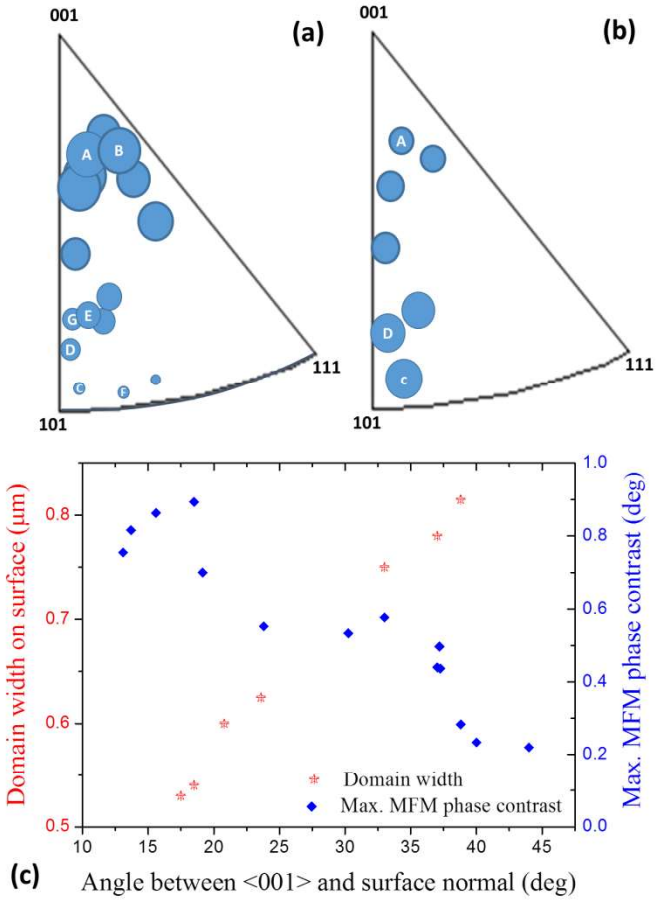

Figure 5.5: Influence of grain orientation on (a) maximum MFM phase contrast and (b) domain width. The sizes of the bubbles are proportional to the absolute values and the IPFs are shown corresponding to the surface normal. (c) shows the variations in maximum MFM phase contrast and domain width with the deviation of surface normal from the easy axis of magnetization (<100>).

The sizes of the bubbles in Figs. 5.5 a and b are proportional to the absolute values of the MFM phase contrast and domain width, respectively. It can be observed that the MFM phase contrast decreases and domain width increase with the increased deviation of surface normal from the easy axis of magnetization (<001>). The variations in the

maximum MFM phase contrast and domain width with angle between <001> and the surface normal are shown in Fig. 5.5c. The observed variations in the MFM phase contrast and domain width can be explained by considering out-of-plane magnetization, as shown schematically in Fig. 5.6.

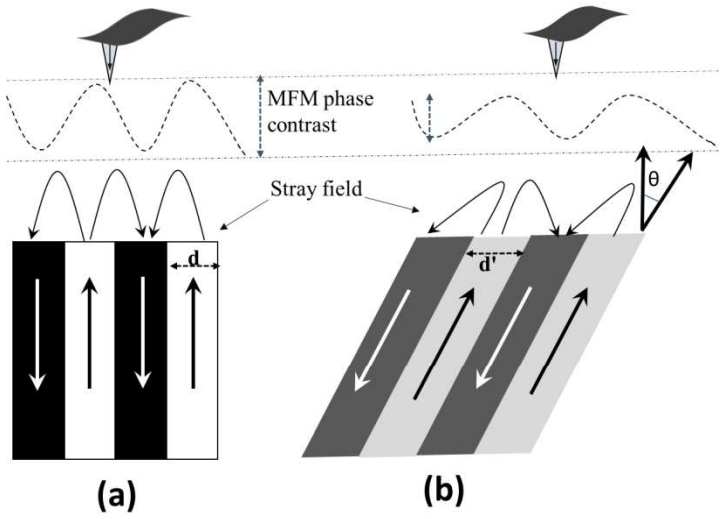

Figure 5.6: Schematic representation of the magnetic moments with their respective stray fields for a perfect orientation along easy [001] direction (Left) and with an angle ($\theta > 0°$) (Right).

The MFM tip is magnetized perpendicular to the surface and hence senses the component of the stray field emerging perpendicularly from the surface. In case of the surface normal parallel to the easy axis of magnetization (Fig. 5.6a), the stray fields are also normal to the surface and the maximum MFM phase contrat is observed. With increasing deviation of surface normal from the easy axis of magnetization (Fig. 5.6b), only a part of the stray field component that is perpendicular to the surface, influences the phase of the vibrating cantilever. This leads to decrease in the MFM phase contrast as observed in Fig. 5.5. The domain width is minimum if the domains are oriented parallel to the surface normal and increases with increasing deviation of surface normal from the easy axis of magnetization (Fig. 5.6). Increase in domain width with increasing angle

between easy magnetization and surface normal was also observed by Batista *et al.* [144] in perpendicularly magnetized cementite precipitates.

The alignment of the stripe domains are also observed to be governed by the crystallographic orientation. For the grains with surface normal along <110> direction, the domain stripes are found to be oriented along the easy axis of magnetization parallel to the surface, as seen in Fig. 5.4. For example, grains C and F with [001] parallel to the Y_0 direction (red in Fig. 5.4b) exhibit domain stripe alignment along the Y_0 axis; whereas, grains B, D and E with [001] parallel to the X_0 direction (red in Fig. 5.4a) exhibit domain stripe alignment along the X_0 axis. A grain with surface normal parallel to <100> direction, such as Grain A shown as red in all the three IPFs (Figs. 5.4a-c), can exhibit alignment along one of the two easy axes depending upon the previous magnetization. Because of the minor loop demagnetization (with the range of ±2000 Oe) performed in the horizontal direction (parallel to X_0 axis), the domains in Grain A are aligned along the X_0 axis.

5.2.2 Evolution of domain structure in presence of external field

5.2.2.1 Magnetization curve of the bulk specimen

Figure 5.7 shows the magnetization curve obtained for the DSS specimen at low temperature (2.2 K) and room temperature (300 K) by VSM measurements. The field required for complete saturation of the bulk specimen is ~ 5 kOe and the saturation magnetization at room temperature is about 0.98 T (99.9 emu/g). In VSM study, the average macroscopic magnetic properties of the specimen are measured. The bulk remanence and coercivity values obtained by VSM measurement of the DSS sample are similar to those reported in earlier studies [145, 146]. Both iron and DSS has negligible remanence and coercivity. Hence, the saturation magnetization obtained for DSS with ~50% ferrite is about half of that reported for a pure iron specimen [147].

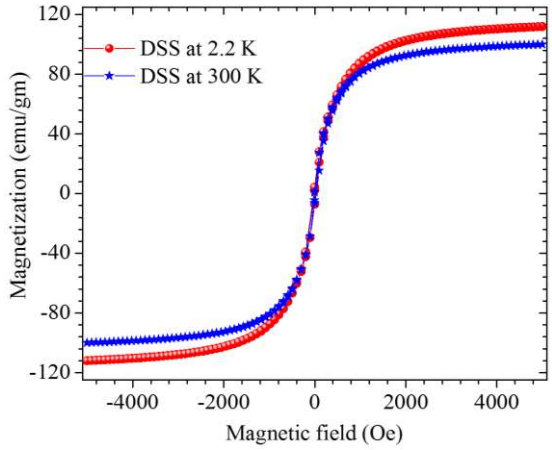

Figure 5.7: Magnetization curve for DSS at low temperature and room temperature.

5.2.2.2 Field induced domain dynamics

MFM image of the same area as shown in Fig. 5.4d was obtained in presence of in-plane external magnetic field in the complete cycle of ±1600 Oe. The field was increased in steps of 200 Oe up to 1600 Oe followed by decrease in 2 steps. Subsequently, the field direction was reversed, and the field was increased in steps of -200 Oe up to -1600 Oe followed by decrease in 2 steps. MFM images were obtained by holding the field at every step. At first, the complete cycle of in-plane magnetic field was applied parallel the Y_0 direction (Fig. 5.4a) *i.e*. along the vertical direction in Fig. 5.8. The typical MFM images corresponding to various applied fields viz 0 Oe, 800 Oe, 1600 Oe, 0 Oe, -1600 Oe and 0 Oe during one magnetization cycle are shown in Figs. 5.8 (a) through (f), respectively. The influence of applied field on the domain structure is analyzed in view of the direction of easy axis of magnetization on the surface with respect to the applied field. As discussed in the previous section, the grains with surface normal along <110> direction (Grains B-F) exhibit domain stripes oriented along the easy axis of magnetization parallel to the surface. For such grains with easy axis of magnetization orthogonal to the applied field direction (such as Grain D), no appreciable change in

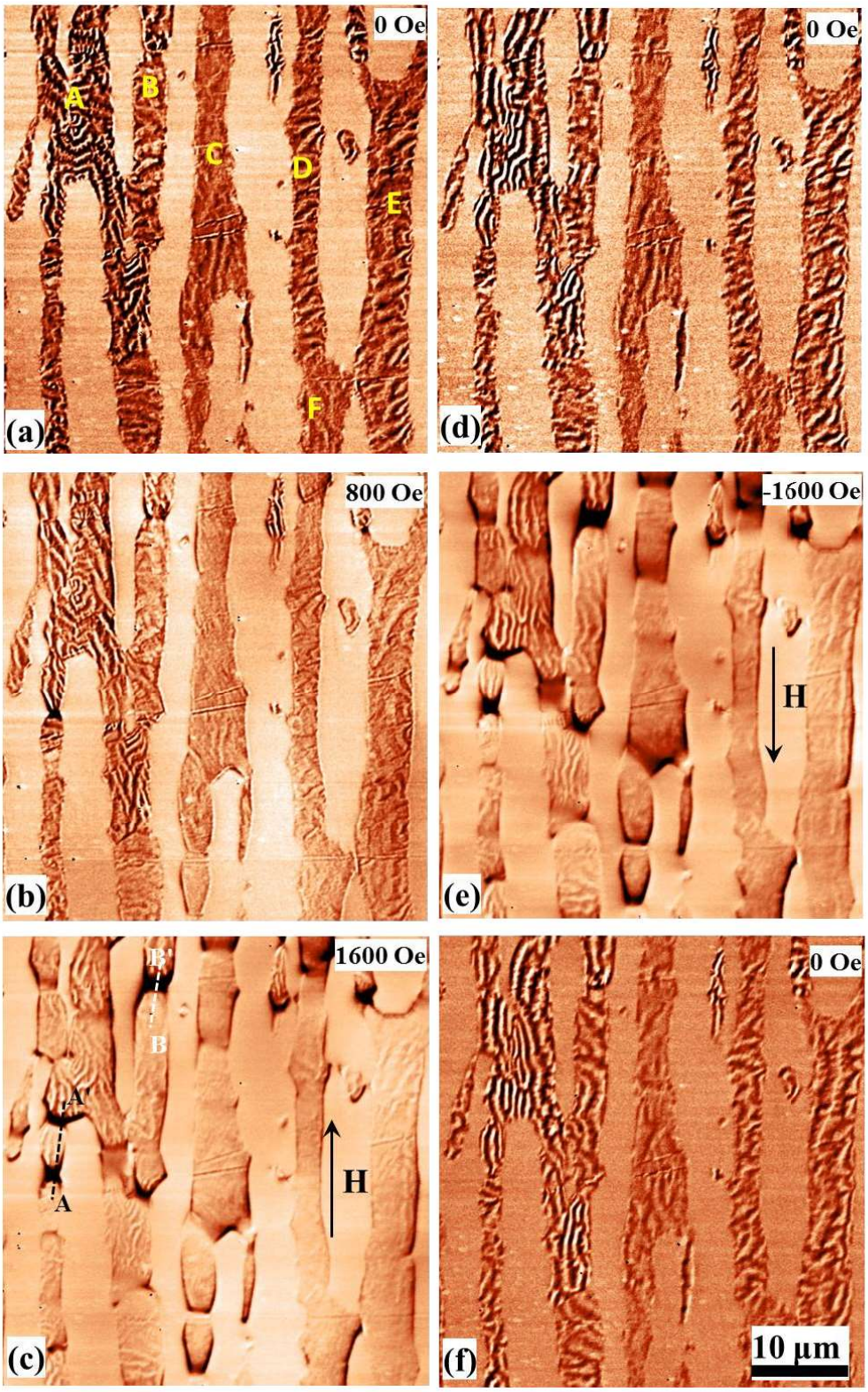

Figure 5.8: MFM phase maps obtained in presence of in-plane magnetic field of (a) 0 Oe [0.7°], (b) 800 Oe [1.03°], (c) 1600 Oe [2.8°], (d) 0 Oe [0.48°], (e) -1600 Oe [2.5°] and (f) 0 Oe [0.92°], The positive direction field is upwards and the negative direction is downwards. The values in [ ] indicate the range of MFM phase variation in the corresponding image.

domain structure is observed with applied field except for a small reduction in the domain contrast. For such grains with easy axis of magnetization along the applied field (Grains C and F), the domains were already aligned along the applied field direction. With the application of external field, a larger reduction in the domain contrast is observed in these grains as compared to the other grains. After the completion of the magnetic cycle, the domains with stripes aligned in the field direction are observed as in the initial condition. The study indicates that the grains with surface normal along <110> direction (Grains B-F) does not exhibit any appreciable change in the domian structure upon application of magnetic field in the direction parallel or perpendicular to the easy axis of magnetization in DSS upto the maximum field of ±1600 Oe applied in the present study. However, interesting results are observed for grain with surface normal along <100> direction (Grain A) for which two perpendicular easy axes of magnetization are present on the surface. Domain stripes aligned along X_0 axis is observed in the initial condition due to the application of field in the X_0 direction for demagnetization. After application of the magnetization cycle, the domain stripes are found to be aligned in the vertical (Y_0) direction *i.e.* along the direction of applied field. The evolution of magnetization in this grain can be visualized clearly in Figs. 5.9 a-*l* showing the magnified MFM phase maps of Grain A at smaller steps of applied field. It can be seen in Fig. 5.9a that even though the stripe domains seem to be aligned along X_0 direction, perpendicular domains are also observed branching from them as indicated within the rectangle in Fig. 5.9. Upon application of magnetic field in Y_0 direction, the small branching domains grow in the direction of applied field and join with the branching domains of the neighbouring stripes (Fig. 5.9c). At the same time, the stripe domains in the X_0 direction (perpendicular to the applied field) shrink. These lead to the final magnetic structure with domain stripes aligned in the direction of applied magnetic field *i.e.* vertical direction (Fig. 5.9e). With application of field in the opposite direction, further domain alignment parallel to the

magnetization direction is observed (Fig. 5.9*l*). In these case, the direction of the stripes is rotated along the field direction. Which is earlier identified as rotatable anisotropy in the CoP thick film by Oscar de Abril et. al. [139].

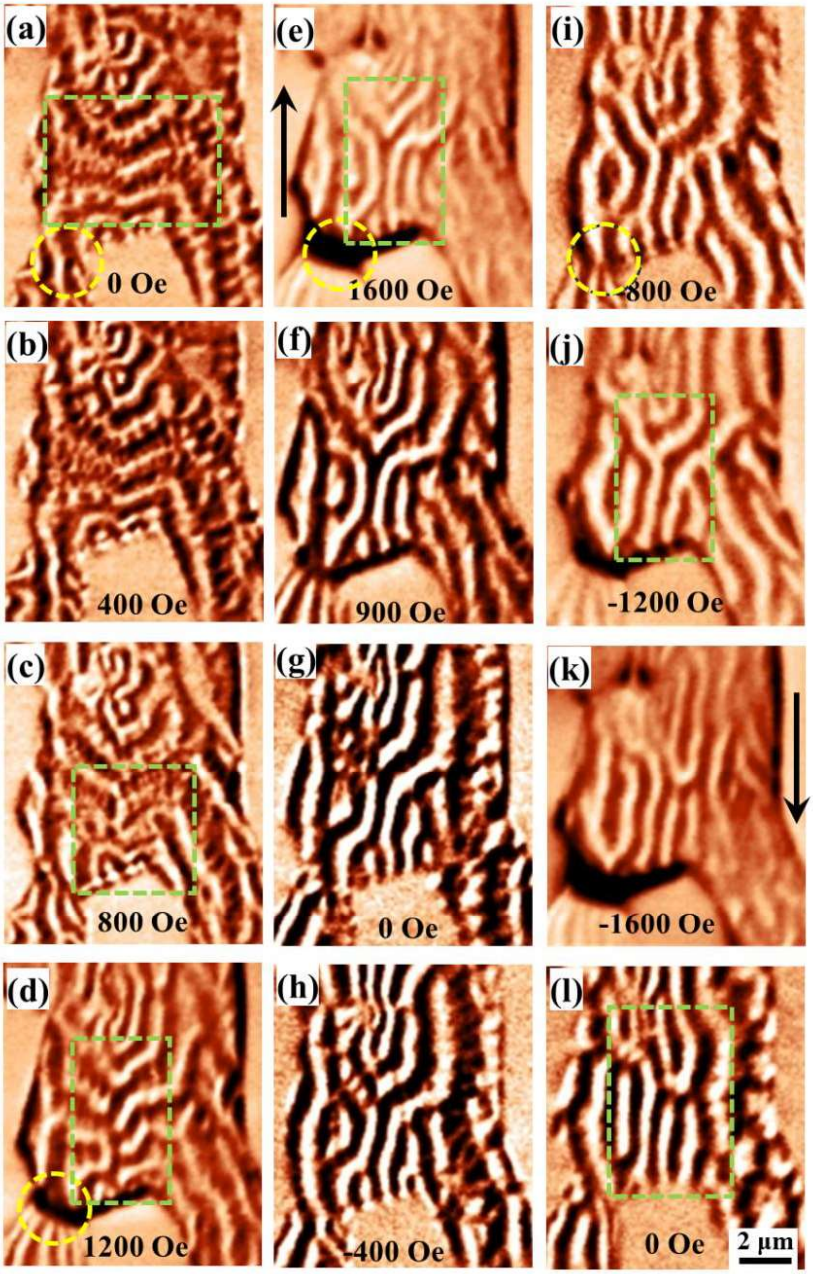

Figure 5.9: MFM phase maps obtained in presence of in-plane magnetic field of (a) 0 Oe [0.75°], (b) 400 Oe [1°], (c) 800 Oe [1.2°], (d) 1200 Oe [1.7°], (e) 1600 Oe [2.8°], (f) 900 Oe [0.93°], (g) 0 Oe [0.4°], (h) -400 Oe [0.46°], (i) -800 Oe [0.9°], (j) -1200 Oe [1.46°], (k) -1600 Oe [2.54°] and (*l*) 0 Oe [0.72°]. The positive direction field is upwards and the negative direction is downwards.

After subjecting the DSS specimen to a magnetization cycle in the Y_0 (vertical) direciton, the specimen was subjected to a magnetization cycle in the X_0 (horizontal) direction. Figure 5.10 shows the MFM phase maps obtained at different magnetic field values during the magnetization. Similar phenomena as observed during magnetization in the Y_0 direction are observed. For the grains with surface normal along <110> direction, no appreciable change in the domain structure has been observed. However, Grain A with surface normal along <100> direction exhibted change of stripe alignment from vertical to horizontal direction.

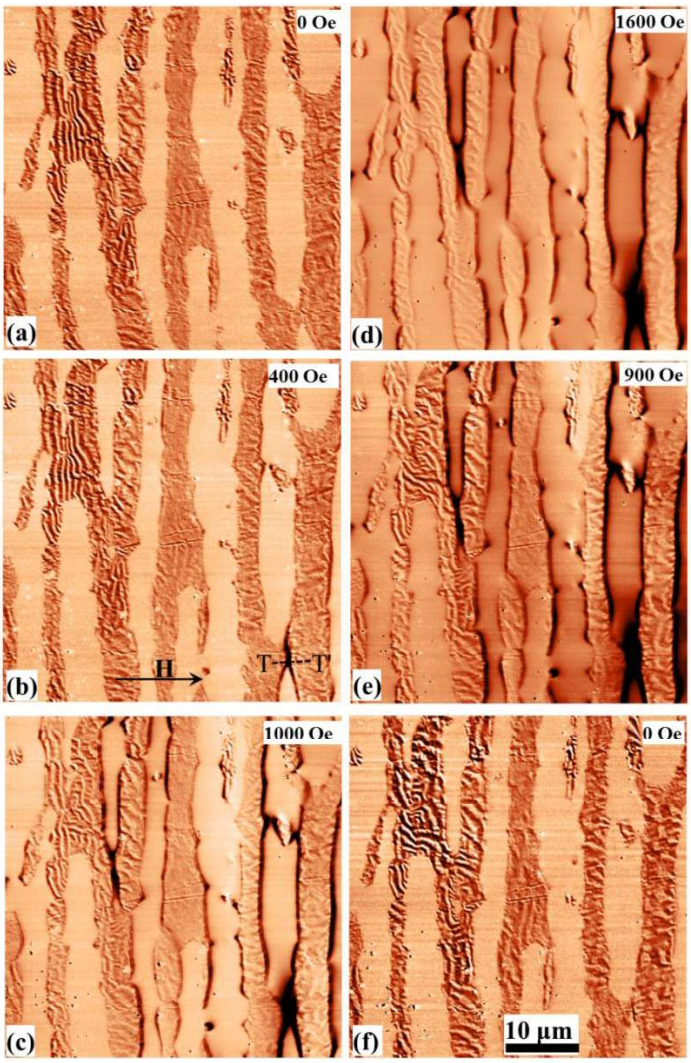

Figure 5.10: MFM phase maps obtained in presence of in-plane magnetic field of (a) 0 Oe [1.42°], (b) 400 Oe [2.3°], (c) 1000 Oe [2.7°], (d) 1600 Oe [8.8°], (e) 900 Oe [2.2°] and (f) 0 Oe [1°], The field direction is towards right.

5.2.2.3 *Role of grain orientation on field induced domain dynamics*

The role of grain anisotropy effect on magnetization can be summarized in Fig. 5.11 showing the MFM phase maps in Grains A, C and D in remnant conditions after application of in-plane magnetic fields in the orthogonal directions. Grains C (Figs. 5.11 b, e and h) and D (Figs. 5.11c, f and i) did not exhibit much variation in the domian structure, however the changing stripe alignments in Grain A (Figs. 5.11 a, d and g) with application of in-plane fields in the orthogonal directions can be clearly visualized. All MFM phase maps in Fig. 5.11 are shown with the same phase range values [1.4°] for ready qualitative comparision in the phase variaions. No change in phase contrast is observed in any of the three grains after the magnetization cycles.

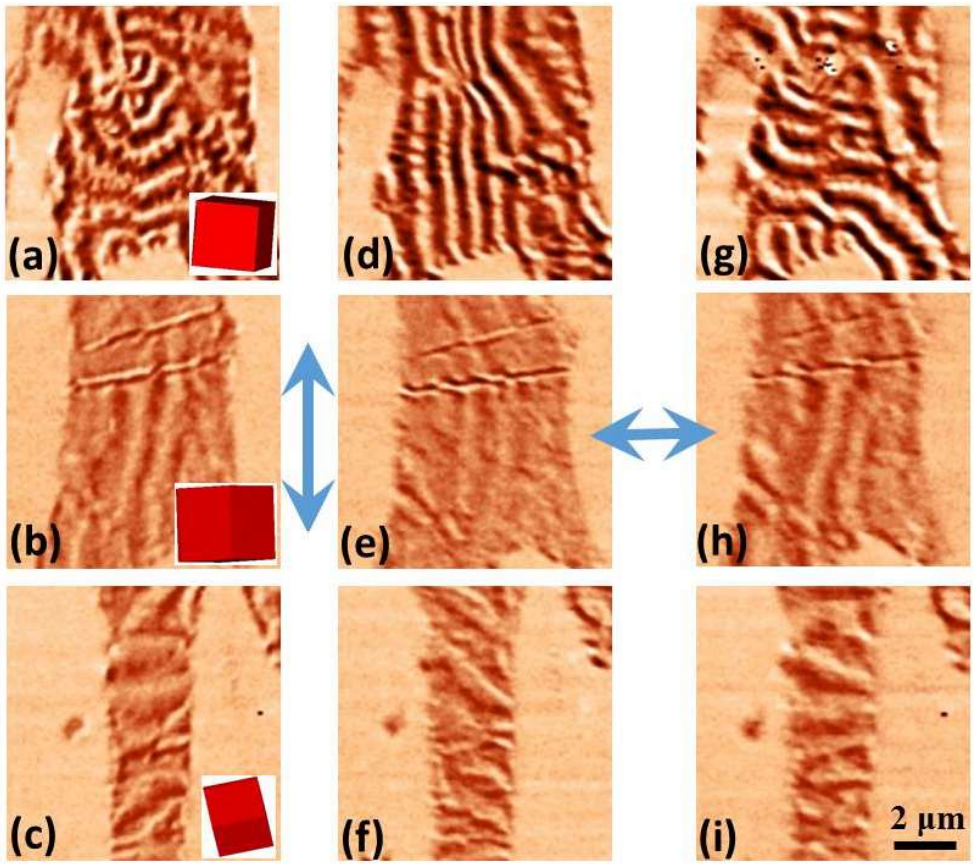

Figure 5.11: MFM phase maps [phase range = 1.4°] for three grains with different crystallographic orientations as indicated by the cube orientations in the insets obtained at remnant conditions after applying magnetic cycles (±1600 Oe) in the directions indicated by arrows.

5.2.2.4 Influence of grain mis-orientation on the stray field at the boundaries

In addition to the change in the domain structure within the ferrite grains, leakage of stray fields at their interfaces with neighbouring ferrtic grains are also observed at higher applid field values, as indicated with circle in Fig. 5.9. The leakage of stray fields are essentially observed for the grain boundaries perpendicular to the applied field direction (Figs. 5.8 and 5.10). The MFM phase across two grain boundaries along AA' (shown in Fig. 5.8c) and a grain boundary along TT' (Fig. 5.10b) are shown in Figs. 5.12 a and b, respectively for application of fields in vertical and horizontal directions. The variations in the maximum MFM phase values across the first grain boundary along AA' and across the grain boundaries along BB' (Fig. 5.8c) and TT' are shown in Fig. 5.12c. It can be seen that the leakage field is observed beyond a minimum (threshold) applied field and it increases almost linearly with further increase in the applied field upto 1600 Oe. For example, the leakage field starts to appear clearly at 400 Oe, 600 Oe and 1200 Oe for the grain boundaries across TT', first grain boundary across AA' and second grain boundary across AA', respectively. Further, the rate of change in the phase variations with the applied field and the extent of phase variations are also different at different boundaries. The leakage field at the grain boundaries are observed due to the surface free poles appearing at grain boundaries shared by grains with different magnetic orientations where the discontinuity (divergence) of saturation magnetization (M_s) across them leads to a divergence of magnetic field [148]. In view of this, an attempt is made to correlate the MFM phase contrast observed across the grain boundaries with the mis-orientations between the adjoining grains obtained by the EBSD study.

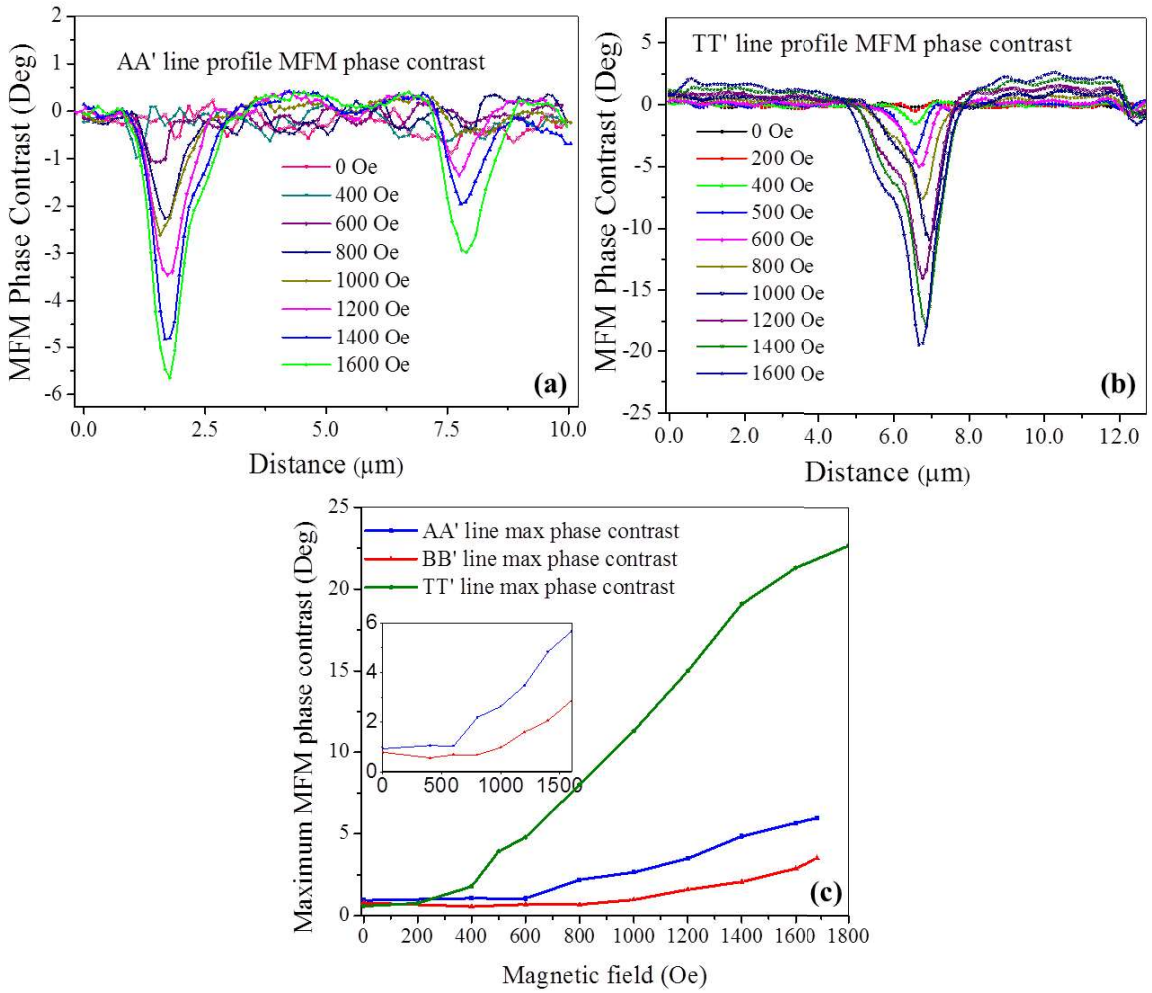

Figure 5.12: MFM phase variations along lines (a) AA' (Fig. 5.8) and (b) TT' (Fig. 5.10) at different field values. The maximum MFM phase contrast is plotted against field values in (c).

MFM phase contrast at the grain boundaries oriented close to the X_0 direction are considered during application of magnetic field in the Y_0 direction and vice versa. Figure 5.13 shows the variations in the maximum MFM phase contrast at 1600 Oe at all the grain boundaries in the area selected for MFM analysis (Fig. 5.4). It can be seen in Fig. 5.13 that the MFM phase contrast is very low for the grains with similar orientations across the boundary *i.e.* with small mis-orientation. A linear increase in the maximum MFM phase contrast is observed with increasing mis-orientation between the adjoining grains with the application of magnetic field in the X_0 direction. The extent of increase is found to be more for the grain boundaries parallel to the Y_0 direction (magnetization in

X_0 direction) as compared to that to the X_0 direction (magnetization in Y_0 direction). This could be attributed to the concentration of stray field at only a few available ferrite-ferrite grain boundaries during magnetization in X_0 direction. Further, at a few boundaries with large mis-orientations in the range of 55-60°, very low MFM phase contrast values are observed. These boundaries are associated with Grains D and F (Fig. 5.4) which exhibited very low MFM contrast within the ferrite grains also (Fig. 5.5a). This indicates that in addition to the mis-orientation between the two grains, their surface normal with respect to the easy magnetization axis also plays a role in governing the amount of leakage field.

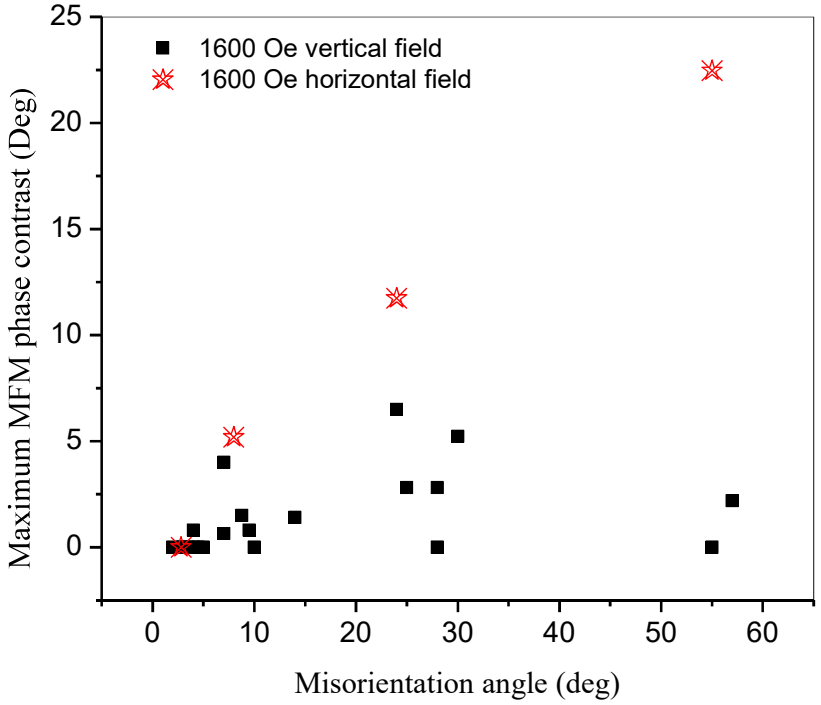

Figure 5.13: The variation in the maximum MFM phase contrast across the grain boundaries as a function of the mis-orientation between the adjoining grains.

5.3 CONCLUSIONS

The influences of crystallographic orientation and in-plane magnetic field on the domain structure in the ferrite phase of a DSS are studied in detail in the present paper using MFM. Most of the visualized magnetic domains in the DSS specimen are

perpendicularly magnetized to the surface. The width of the stripe domain increases linearly and the MFM phase contrast decreases almost linearly with the deviation of the surface normal from the easy axis (<100>) of magnetization. In the range of applied magnetic field of ±1600 Oe, no appreciable change in the domain structure is observed for the grains with plane normal close to <110> directions. However, alignment of the stripe domains in the direction of the applied field is clearly visualized for the grain with surface normal and applied field along <100> directions. The leakage of stray field at a grain boundary is found to appear at a threshold applied field perpendicular to the boundary and increases linearly with increasing applied field. Further, the stray field at a grain boundary is found to be the function of the mis-orientation between the adjoining grains and also depends upon the deviation of the surface normal from the easy axis of magnetization. The paper provides a better understanding of the domain structure and its field induced domain dynamics in a duplex structure with cubic ferromagnetic phase exhibiting out-of-plane magnetization.

MFM STUDIES IN FINE MARTENSITE PRECIPITATES IN AN AUSTENITE MATRIX

6

6.1 INTRODUCTION

The current chapter investigates magnetic domains and micromagnetic events in fine precipitates of the strain induced martensite (SIM) phase in a 47% cold worked AISI type 304 austenitic stainless steel (AUSS). In the earlier chapters, the micro-magnetization studies were carried out on the specimens having magnetic phases larger than a few micrometers. Conversely, the current chapter deals with the specimen having sub-micron sized magnetic structures in the paramagnetic austenitic matrix. Understandings of magnetic properties of sub-micron sized magnetic particles are important as such particles are candidates for various practical applications such as non-volatile magnetic random access memory, magnetic storage media and magnetic logic gates. The conventional method for fabrication of nano/micro sized domain structure are the electron beam lithography, laser lithography, scanning probe lithography, nanoimprints, radiation damage and multiple step growth methods [149]. However, in the present case, strain induced precipitation of martensite phase upon cold working of a meta-stable austenitic phase has been utilized for obtaining fine ferromagnetic structures. The extent of cold work is arrived at based on the prior studies of the evolution of size and distribution of martensite phase during cold work of the AUSS [150]. The 47% cold worked AISI 304 stainless steel is pragmatically chosen for having very fine ferromagnetic phases of dimensions smaller than about one micrometer but sufficiently

larger to be probed by MFM (a couple of hundreds of nanometer). The study demonstrates that MFM can be used to identify distribution of strain induced α'-martensite phases due to their magnetic domain structure and it can also be used for understanding of micro-magnetization behavior in very small ferromagnetic phases in a paramagnetic matrix. The influence of microstructural variations on the domain structure, its field dependent domain dynamics and magnetic properties in the three materials studied in the dissertation are also discussed at the end of the chapter.

6.1.1 Martensitic transformation

Generally, different kinds of martensite morphology can be formed by cold working (mechanically) [133], sub-zero cooling (thermally) [151], ion implantation and hydrogen charging [128-130] in AUSS. The SIM transformation is a direct consequence of the plastic deformation of the austenite phase, where dislocation networks and twins act as easy nucleation sites for the martensite. Two types of martensite phases (ε and α') can be formed from the austenite (γ) phase by the following sequences, *i.e.* $\gamma \rightarrow \varepsilon$, $\gamma \rightarrow \alpha'$ and $\gamma \rightarrow \varepsilon \rightarrow \alpha'$ [152, 153]. The hexagonal closed pack ε-martensite is paramagnetic and body center cubic α' martensite phase is ferromagnetic. The α' martensite phase is thermodynamically more stable than the ε-martensite. The ε-martensite forms at smaller strain and transforms into the α' martensite with the increasing strains. The α' martensite may also forms directly from the metastable austenite phase [153, 154]. The α'-martensite nucleates at the shear band intersections and growth occurs by the repeated nucleation of new embryos [155].

6.2 RESULTS AND DISCUSSION

6.2.1 Size effect on domain structure

6.2.1.1 Microstructure of cold worked 304 stainless steel

Figures 6.1 a-c depict the band contrast images obtained on the electro polished sample at different magnifications by the EBSD technique. The microstructure of the 47% cold worked AUSS sample contains highly deformed dislocation sites, twin bands and SIM phases. However, it is difficult to distinguish them in the band contrast images (Fig 6.1). Normally, the α'-martensite nucleates at intersections of twins or shear bands and grows in the form of a plate structure parallel to them.

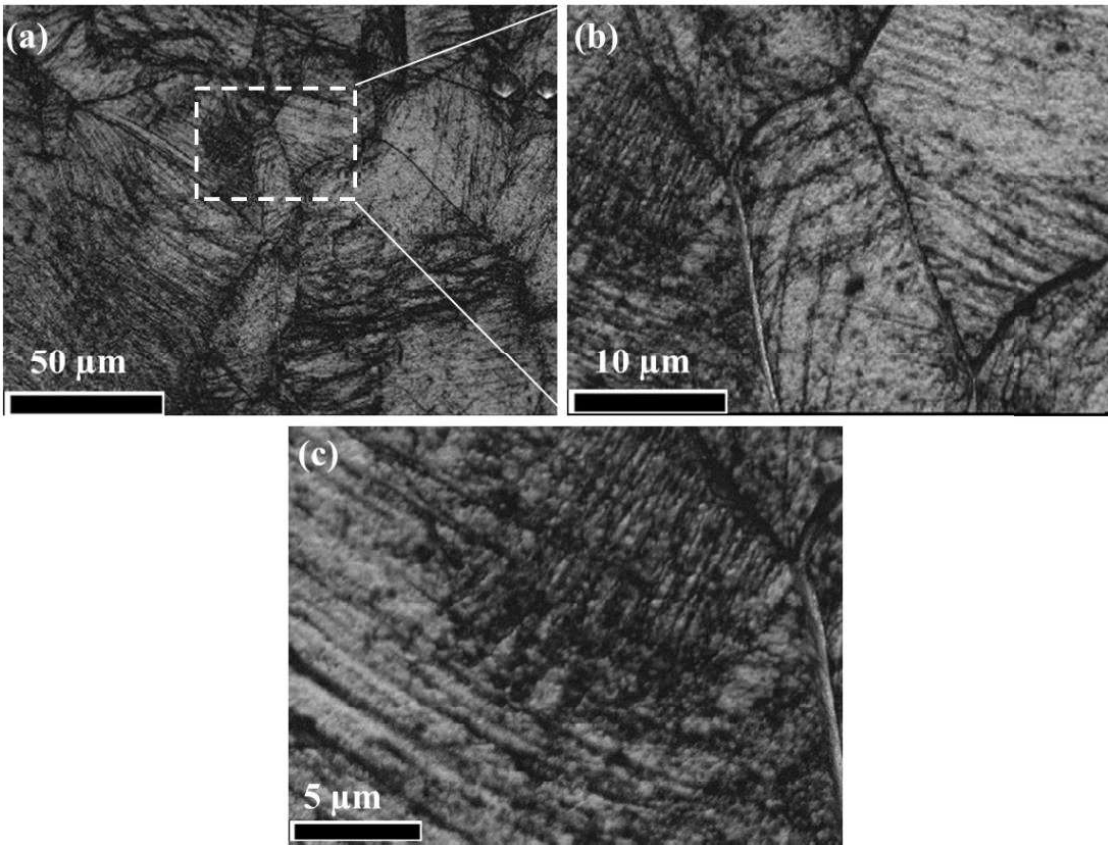

Figure 6.1: Band contrast images, obtained by the EBSD revealing microstructure in 47% cold worked AISI type 304 austenitic stainless steel.

The martensite precipitates could not be indexed reliably by EBSD due to their fine dimensions and deformed structure. Hence, it was difficult to obtain the orientation of the SIM phases in the cold worked sample. The SIM is expected to obey the Kurdjumov-Sachs orientation relationship with the austenite matrix [156].

6.2.1.2 Magnetic domains in α'-martensite phases

Figures 6.2 a and b show the AFM topography and the MFM phase map respectively, of the cold worked 304 SS sample. In the semi-contact mode, a clean surface image could not be obtained due to the presence of a few artifacts, possibly due to dust particles. Hence, the topography was obtained separately using a contact AFM cantilever in the contact mode. The martensite phases could still not be identified clearly in the topography image. However, distinct magnetic patterns in form of bright and dark contrasts are clearly visible in certain regions of the MFM images and the other regions (austenite matrix) did not exhibit any contrast. The distinct magnetic stray field detected regions are identified as the magnetic domains of the α'-martensite. Hence, the MFM phase map has an ability to detect α'-martensite in the austenite matrix (Fig. 6.2 b). The domains observed regions on the surface correspond to the cross sections of the plate or single rod shape structures of α'-martensite phases. The isolated and grouped lamellae structures of about 10 μm length and isolated dots of α'-martensite phases with diameter smaller than 1 μm can be clearly seen in Fig. 6.2b. Different MFM phase contrasts are observed for different precipitates depending upon the stray field. The white arrow marked region shows continuous linear structure in the topography image, but a discontinuous phase contrast in the MFM image. This may be attributed to in-plane and out-of-plane magnetizations in the domain structure at different regions of the same precipitate. The strong bright and dark MFM phase contrasts correspond to the magnetic

domains with out-of-plane magnetizations. The magnetic domains with in-plane magnetization are visible with lesser contrast.

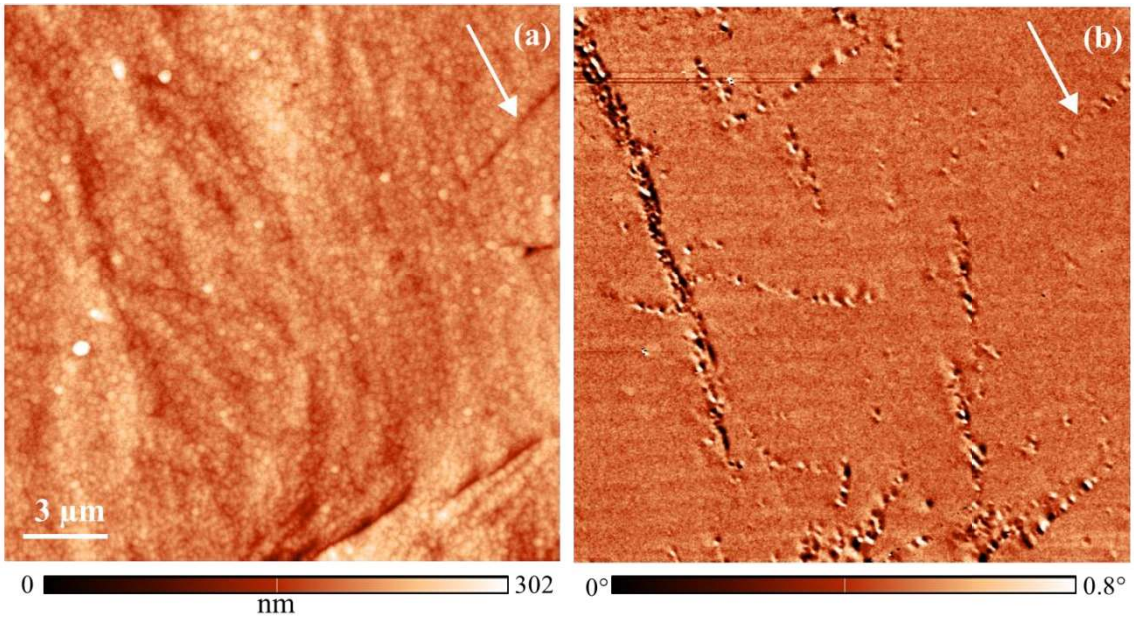

Figure 6.2: (a) Contact mode AFM topography image and (b) MFM Phase image (b) of 47 % cold worked AISI type 304 austenitic stainless steel.

The three orthogonal surfaces of the sample was prepared to obtain the distribution of α'-martensite in different planes. The MFM phase maps were obtained for a scan area of 30 × 30 μm^2 with the resolution of 60 nm on the three surfaces. These MFM phase maps arranged together in the form of a 3D image is shown in Fig. 6.3. The distribution of α'-martensite on the three surfaces depicts almost similar type of domain patterns. The top (normal direction) surface is taken for further investigations.

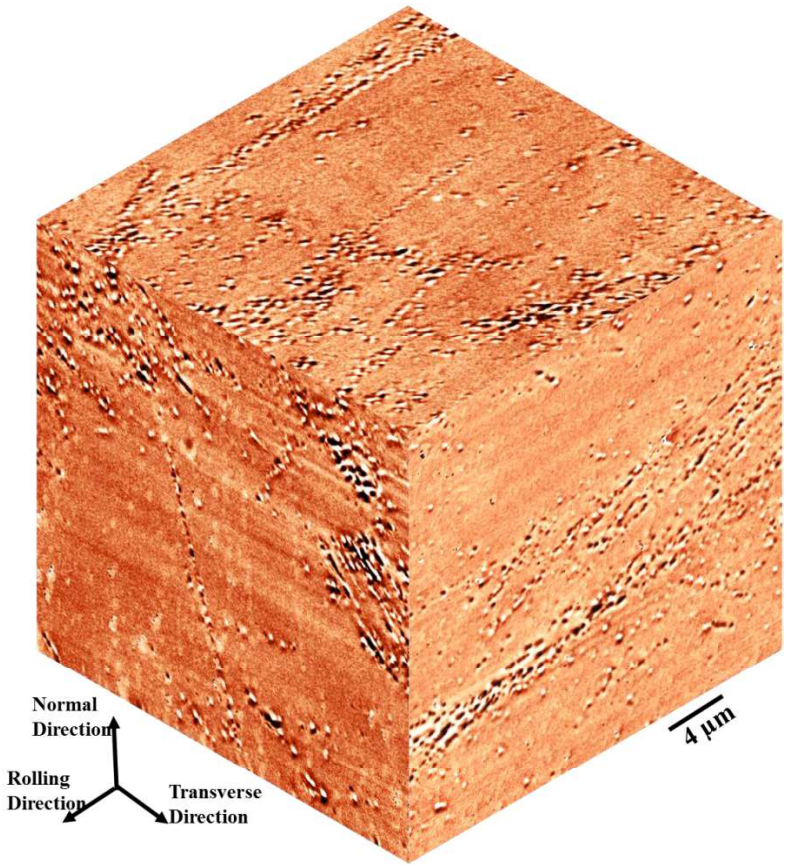

Figure 6.3: Magnetic structure observed in the three orthogonal planes of AUSS sample using MFM.

6.2.1.3 Area fraction of α'-martensite in 47% cold worked AUSS specimen

Figures 6.4 a-d show a few typical MFM images obtained on the surface of the well-polished sample. The distribution of the α'-martensite is observed to be different in different MFM images of area 40 × 40 μm^2, *i.e.* the area fraction of α'-martensite in each image is varying significantly. The difference in the distribution of the martensite phase may be attributed to the different orientations of the parent austenite grain and the SIM formation at different regions. For example, a large amount of martensite is formed near to the grain boundaries, twins and high dislocation density regions. The area fractions of the α'-martensite phase as observed in the MFM images are calculated using Image J© software.

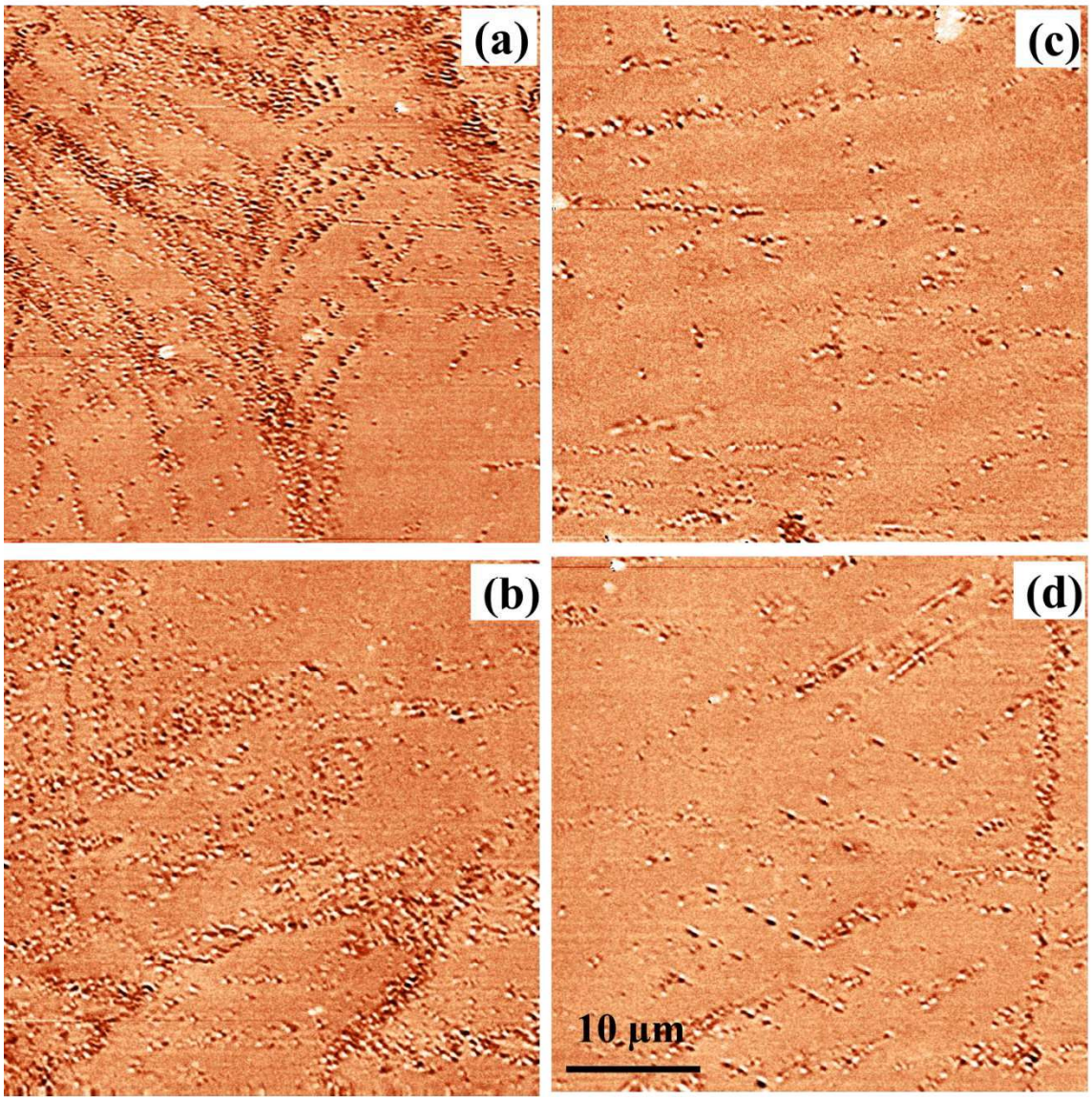

Figure 6.4: Typical MFM phase maps [phase range =1.3°] at four random locations in 47% cold worked specimen to estimate the martensite area fraction.

For example, the area fractions of α'-martensite in Figs. 6.4 a-d are approximately 31%, 27%, 10% and 11%, respectively. Likewise, the area fraction was measured at different randomly selected regions and the results are shown as a histogram in Fig. 6.5. The estimated average value is around 22%, which is very close to that obtained by the X-ray diffraction (21%) in the same sample [150].

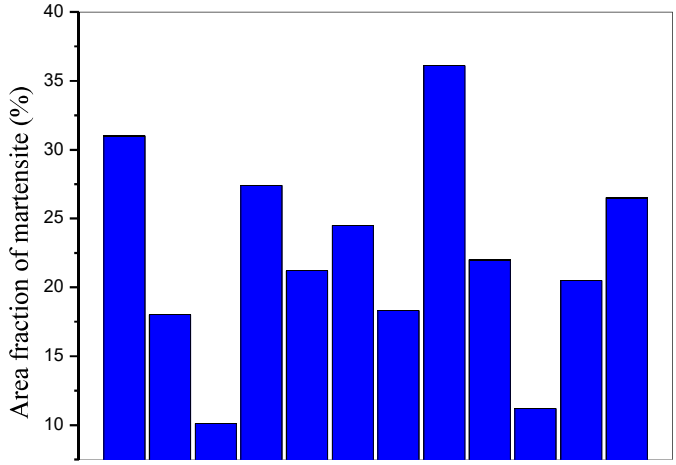

Figure 6.5: Histogram of area fraction of the α'-martensite at different locations.

6.2.1.4 Magnetization curve of the bulk specimen

Figure 6.6 shows the magnetic hysteresis curve obtained for the 47% cold worked 304 stainless steel. The 304 AUSS is basically paramagnetic in nature. However, the ferromagnetic hysteresis loop has been observed due to the presence of the α'-martensite phases. The saturation magnetization value (0.05 Tesla) is disproportionately less considering 21% volume fraction of a ferromagnetic phase which may be attributed to the discuntinuuos magnetic structure. The coercivity field of the sample is about 300 Oe.

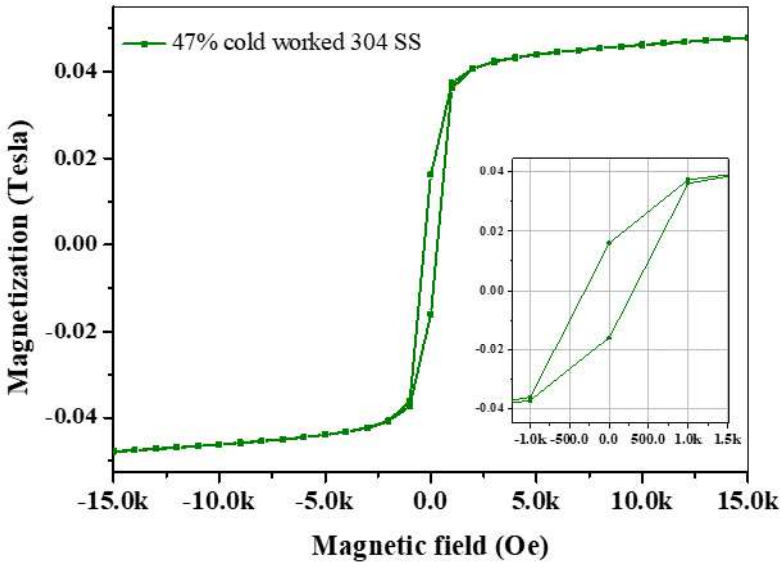

Figure 6.6: Hysteresis loop of 47% cold worked AISI type 304 austenitic stainless steel.

6.2.1.5. Interpretation of magnetic domains in fine α'-martensite precipitates

High resolution (30 nm) topography and MFM phase maps of a 10 x 10 μm^2 area obtained to clearly visualize the domain patterns in α'-martensite phases are shown in Fig. 6.7. Martensite phases of different shapes (round dots and lamellae of different thicknesses) and sizes can be observed in Fig. 6.7b. Further, different variants of martensite can be observed with different orientations within the same austenitic grain. It can be observed in Fig. 6.7 that the domain structure is essentially governed by the shape and size of the martensite phase. The martensite precipitates having apparent circular shape with diameter smaller than 1 μm on the cross-section surface (1-4 indicated with white circles in Fig. 6.7b) exhibited typical of single domain structures such as a dipole or a vortex structure. In 3D, they may be considered to be of a rod shape with closer domains on the top surface as shown schematically in Fig. 6.8a.

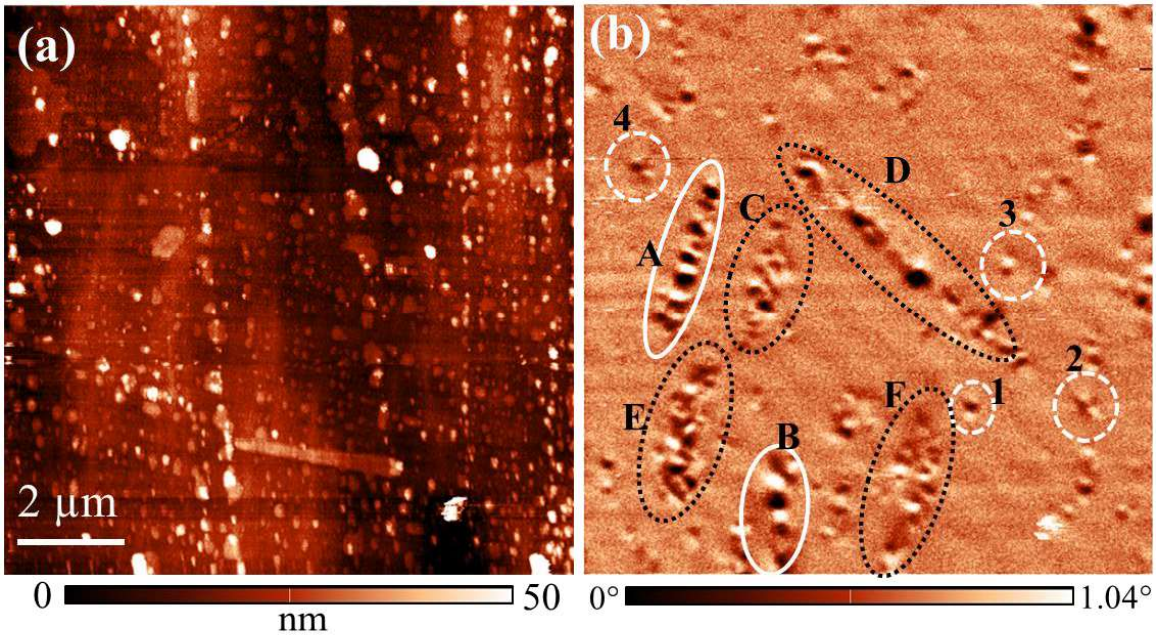

Figure 6.7: (a) Semi-contact AFM topography image and (b) MFM phase image of 47 % cold worked AISI type 304 austenitic stainless steel.

The thin lamellae type α'-martensite precipitates (A and B indicated with white ellipses in Fig. 6.7b) exhibit alternate bright and dark high MFM phase contrast along

their length. The thin stripe or lamellae shape observed on the cross-section surface may correspond to a plate shaped martensite phase in 3D. Based on the large phase contrast and the shape, this possible domain structure with out-of-plane magnetization is schematically illustrated in Fig. 6.8b. Similar domain structures were also observed in individual elongated magnetite lamellae by Frandsen et al. [157].

The thick lamellae type martensite precipitates (C-F indicated with black ellipses in Fig. 6.7b) exhibited complex multi-domain structure with both in-plane and out-of-plane magnetization on the cross-section surface. Similar complex domain structures have also been reported for thin Co stripes of ~2 μm width and 7 μm length [158]. The difference in the domain structure is most dominantly influenced by the thickness and the width of the plate structured phases. When the α'-martensite phase has larger width (*i.e.* two or more plates combined together), they are readily forming the closure domains on the surface with in-plane magnetization to reduce the overall energy. With decreasing width and increasing thickness of the precipitate, domains may tend to have out-of-plane magnetization.

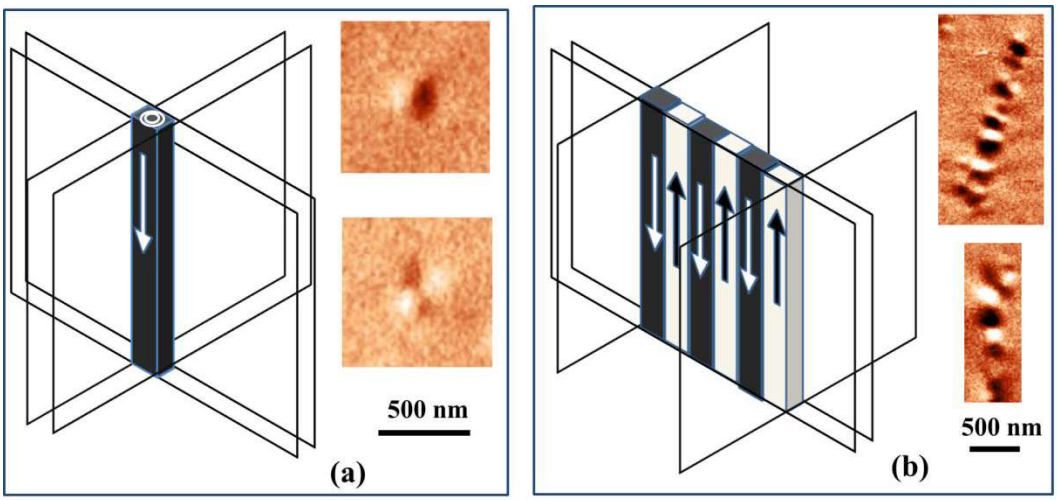

Figure 6.8: Schematic of α'-martensite precipitate at the shear bands: (a) single rod structure showing closure domains such as dipole or vortex domain and (b) plate type structure exhibiting domains with out-of-plane magnetization.

6.2.2 Field Induced domain dynamics in fine phases of α'-martensite.

MFM image of the same area as shown in Fig. 6.7 was obtained in presence of in-plane external magnetic field in the complete cycle of ±1600 Oe. The field was increased in steps of 100 Oe up to 1600 Oe followed by decrease in 3 steps. Subsequently, the field direction was reversed, and the field was increased in steps of -100 Oe up to -1600 Oe followed by decrease in 3 steps. MFM phase maps were obtained by holding the field at every step. After obtaining the MFM phase maps during the complete cycle of in-plane magnetization parallel to the horizontal direction, the sample was rotated by 90° and the MFM phase maps were obtained again for the same area with the applied field in the range of ±1600 Oe. It is a tedious process to obtain the same location of about 10 x 10 μm^2 in the sample after rotation. The intentionally made micro-hardness marks on the sample were found to be very useful to approach the respective locations and subsequently, the exact location was identified by obtaining a few MFM phase maps of larger areas. The MFM phase maps obtained after rotating the sample were rotated by -90° for direct comparison with the other MFM phase maps and are mentioned as magnetization in the vertical direction. A few typical MFM phase maps obtained during magnetization in the horizontal and vertical directions of the sample are shown in Figs. 6.9 and 6.10, respectively.

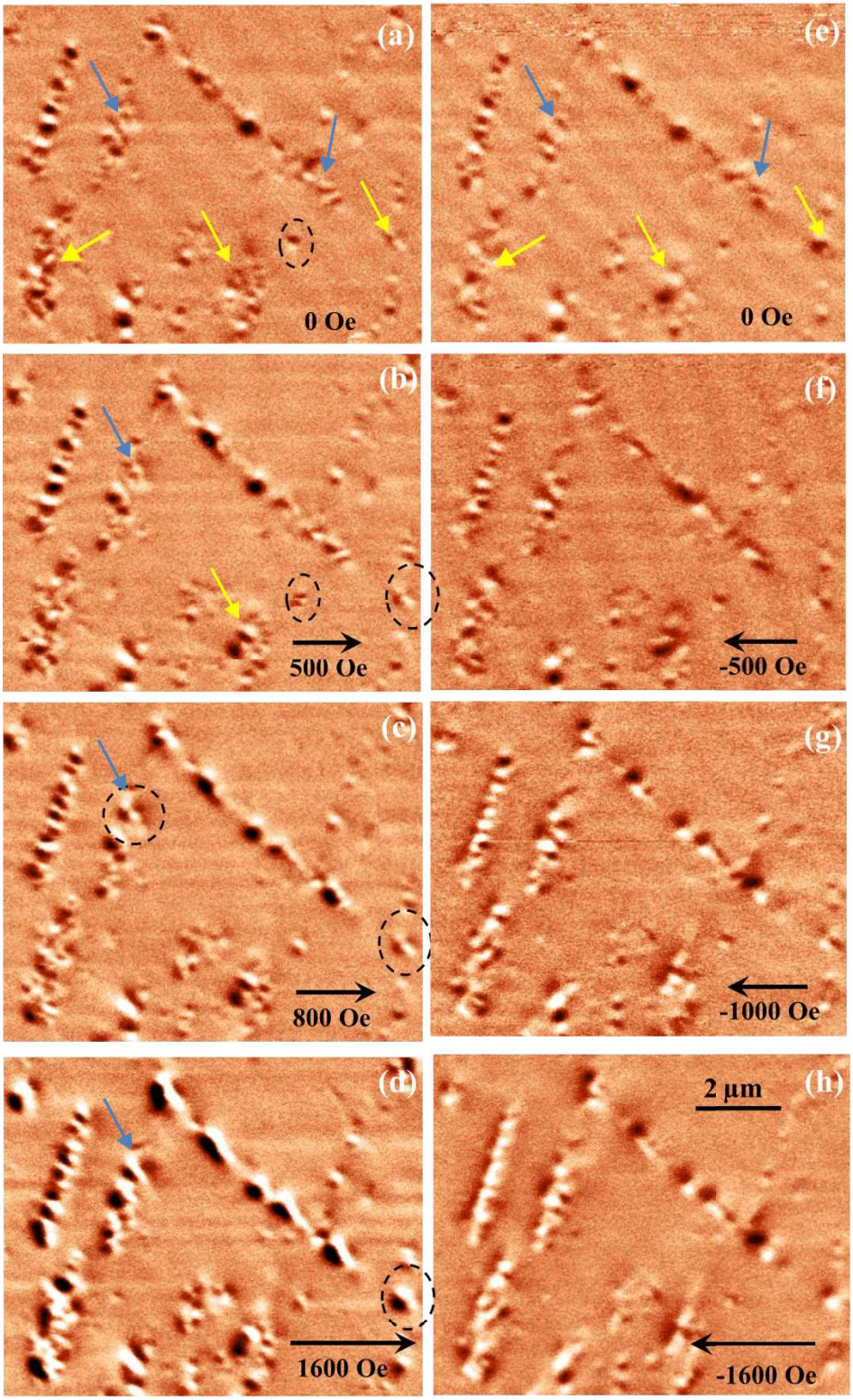

Figure 6.9: MFM phase maps obtained in presence of in-plane magnetic field of (a) 0 Oe [1.4°], (b) 500 Oe [1.4°], (c) 800 Oe [1.4°], (d) 1600 Oe [1.4°], (e) 0 Oe [1.26°], (f) -500 Oe [1.2°], (g) -1000 Oe [1°], and (h) -1600 Oe [1.4°]. Black arrows denote directions of the field. The value in [] indicates MFM phase range.

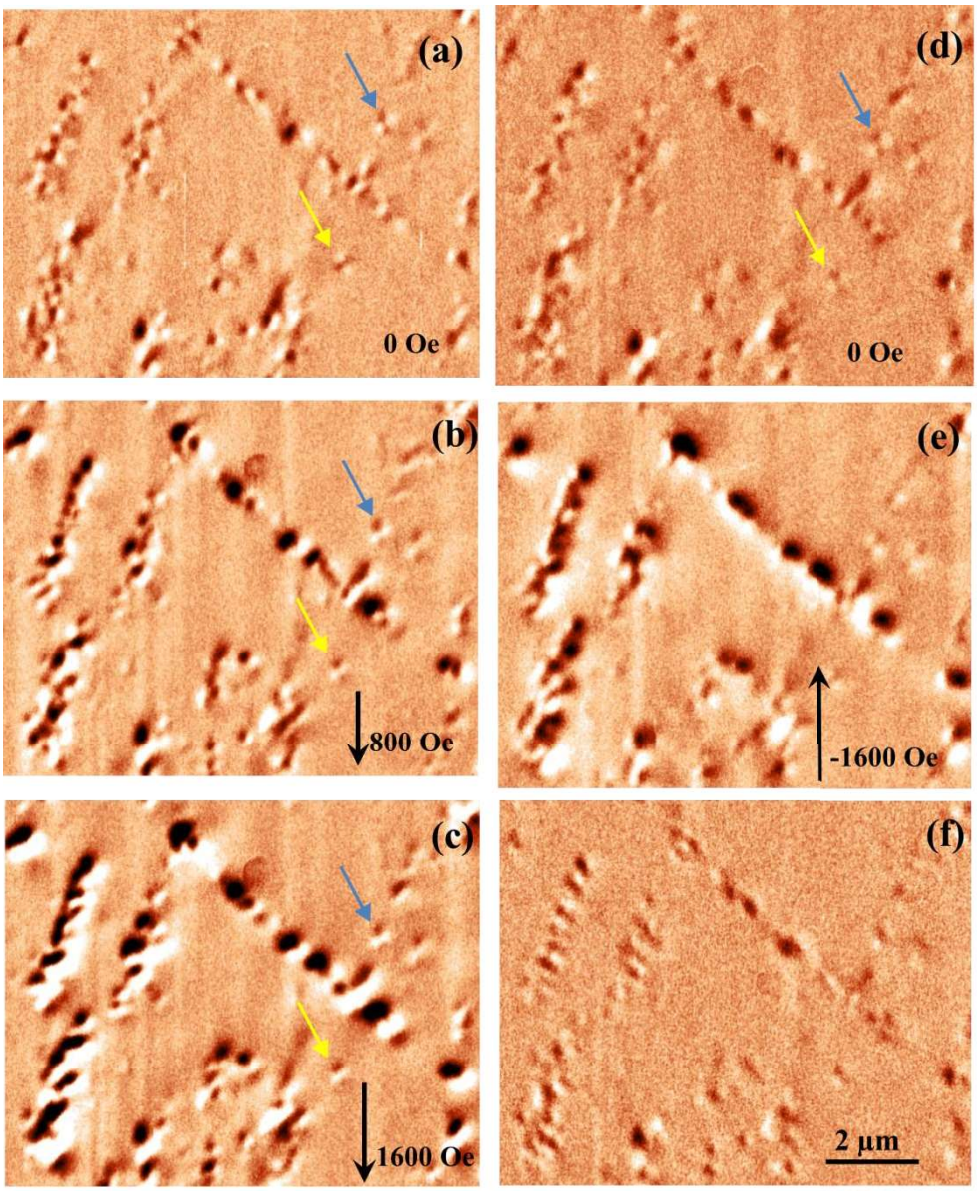

Figure 6.10: MFM phase maps obtained in presence of in-plane magnetic field of (a) 0 Oe [1.05°], (b) 800 Oe [1.05°], (c) 1600 Oe [1.05°], (d) 0 Oe [0.9°], (e) -1600 Oe [1.05°], and (f) 0 Oe [0.8°] after rotating the sample by 90°. The images are rotated by -90° for ready comparison with results shown in Fig. 6.9. The arrows represent the positive and the negative field direction.

Figure 6.9a shows the MFM image in the absence of magnetic field, which depicts various types of domains, as discussed earlier. Different domains exhibited different response to the applied magnetic field. Domain A with alternative high contrast (described as out-of-plane magnetization in Fig. 6.8b) didn't exhibit large variation in the structure or contrast of the domain up to about 1000 Oe. With further increase in the

applied field, slight increase in the contrast along the direction of the applied field is observed. However, obvious changes in structure and contrast are observed for many other domains exhibiting in-plane magnetization, *e.g*. a change in the structure of Domain C (parallel to Domain A *i.e.* having same crystallographic orientations) can be observed in the phase map obtained at 500 Oe. After applying 1600 Oe and removal of the field, a complete change in the structure is observed for domain C which exhibits a structure similar to that of Domain A (Fig. 6.9e).

After application of the complete cycle of magnetization, when the sample was rotated and the phase map was obtained, both Domains A and C exhibited similar in-plane magnetization (Fig. 6.10a). With the starting domain structure having in-plane magnetization, a large change in the structure and contrast of Domain A is observed at relatively low applied field itself (Fig. 6.10b). At the end of the magnetization cycle, Domain A exhibited again out-of-plane magnetization. The variations in the maximum relative MFM phase contrast within Domain A with the in-plane applied magnetic field in both horizontal and vertical directions are shown in Fig. 6.11. It can be clearly seen that the phase contrast within Domain A was influenced very marginally during the application of field in the horizontal direction *i.e.* when the domain exhibited out-of-plane magnetization. However, a systematic large variation is observed during the application of field in the vertical direction, when the domain exhibited in-plane magnetization.

The study indicates that the domain structures for fine (thin) precipitates are highly dependent upon the magnetic history. The same precipitate may exhibit out-of-plane or in-plane magnetization. However, precipitates E and F with larger width as compared to that of precipitates A and C, exhibited in-plane magnetization only with complex magnetic domain structure after the magnetization cycles. Other, noticeable

variations in the domain structure after one positive cycle of magnetization are indicated with arrows in Figs. 6.9 a and e.

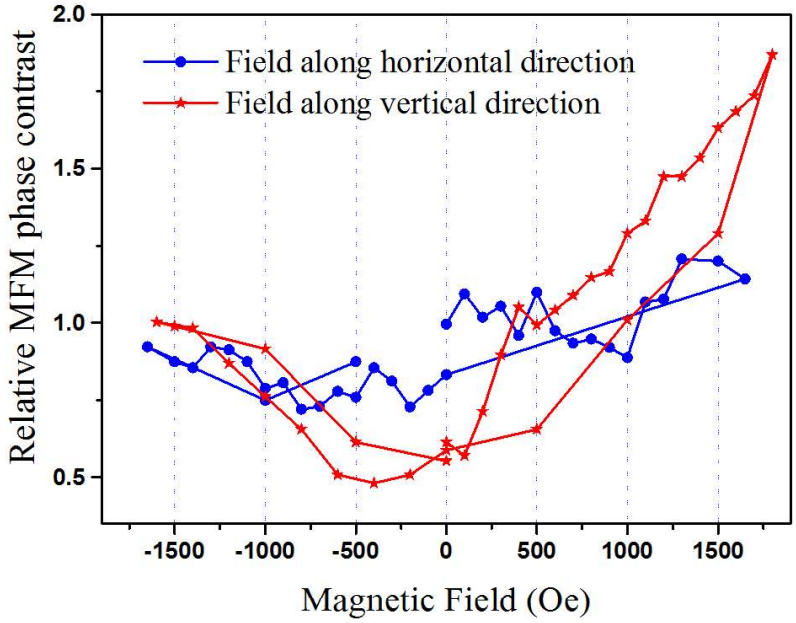

Figure 6.11: Variations in MFM phase contrast with the in-plane external magnetic field.

6.2.2.1 Rotation of vortex domains with applied field

As discussed in section 6.2.3.5., the martensite precipitates having apparent circular shape with diameter smaller than 1 μm on the cross-section surface (1-4 indicated with white circles in Fig. 6.7b) exhibited typical structure of a closure domain in form of a single domain such as a dipole or a vortex structure. In the demagnetized condition, two oppositely rotated vortex domains were identified in Fig 6.10a (denoted as Vortex A and Vortex B) to study their response to the external magnetic field. Vortex A exhibited clockwise magnetization (bright contrast on top left and bottom right quadrants), whereas Vortex B exhibited anticlockwise magnetization (bright contrast on top right and bottom left quadrants) (Fig 6.12a) [159]. With the application of field along the positive direction (direction marked with arrow), vortex A did not exhibit any change in the vortex

direction, rather it simply exhibited a dipole type of structure with large leakage field at higher field values (1000 Oe and 1600 Oe). However, Vortex B exhibited rotation at 500 Oe during application of field in the positive direction. Comparing the MFM phase maps of Vortex B obtained at 300 Oe and 500 Oe, it can be seen that the orientation of the top half of the domain flipped, however the bottom half is similar. The flipped orientation of bottom half can be seen in the MFM phase map acquired at 600 Oe. Beyond 500 Oe, the directions for both the vortices were found to be similar at all the field values. After removal of the field also, both the vortices exhibited clockwise magnetization.

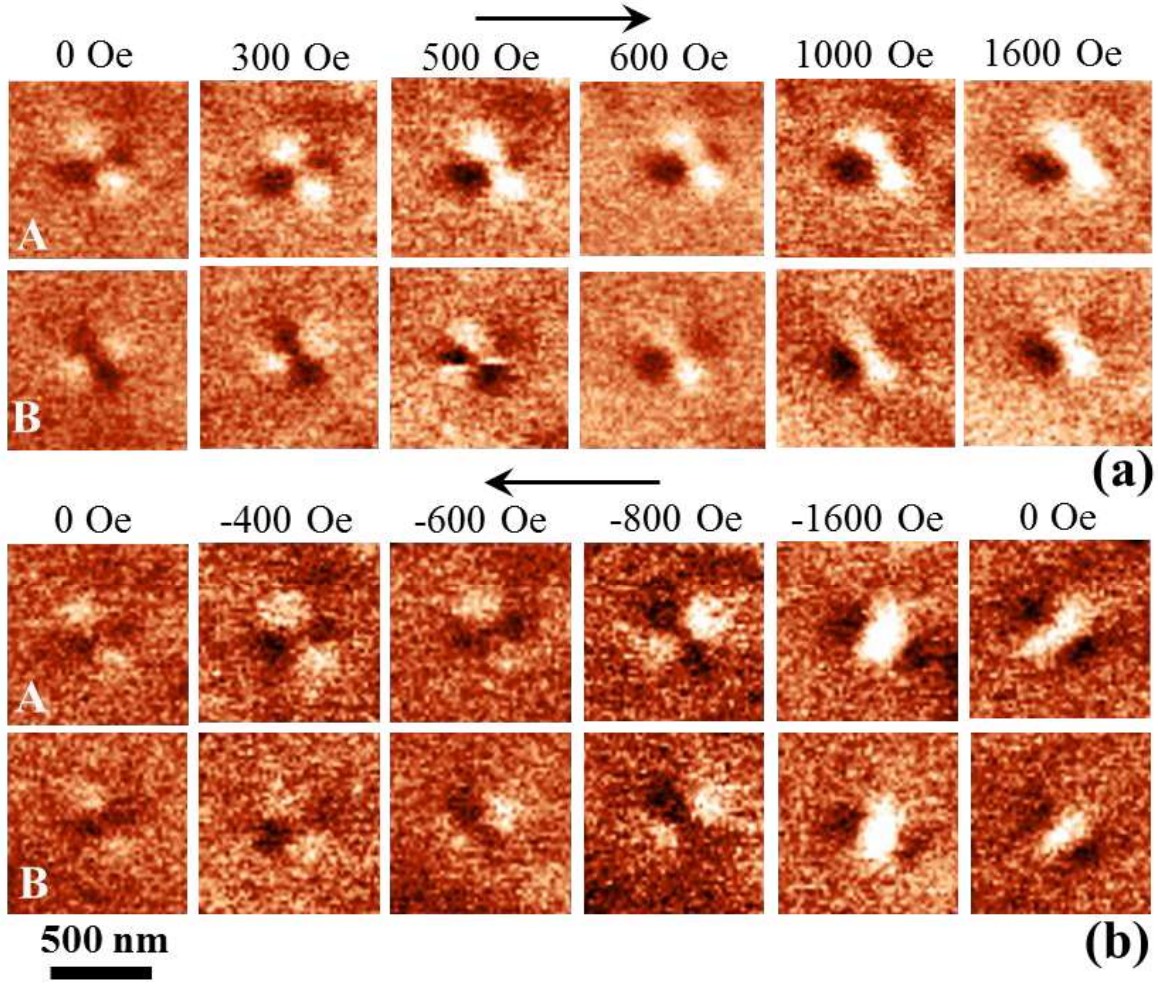

Figure 6.12: Rotation of two vortex domains (A and B) with opposite initial vortex directions upon application of in-plane magnetic field in (a) positive (rightwards) and negative (leftwards) directions as indicated by arrows.

During application of the field in the opposite direction, flipping of vortex direction is observed for Vortex B at -600 Oe. Vortex A also exhibited flipping in the MFM phase map acquired at -800 Oe applied field.

A micro-magnetization loop is generated based on the direction of the vortex as shown in Fig. 6.12. The values for clockwise and anticlockwise directions are taken as +1 and -1. It can be seen in Fig. 6.12. that the vortices may exhibit random orientations in the demagnetized condition. However, they get aligned in the direction of applied field, with almost similar coercivity values in both positive and negative directions of magnetization. The results demonstrate that the basic micro-magnetization studies for single and multiple domains in fine particles can be studied using naturally occurring ferromagnetic α'-precipitates in the paramagnetic austenite matrix.

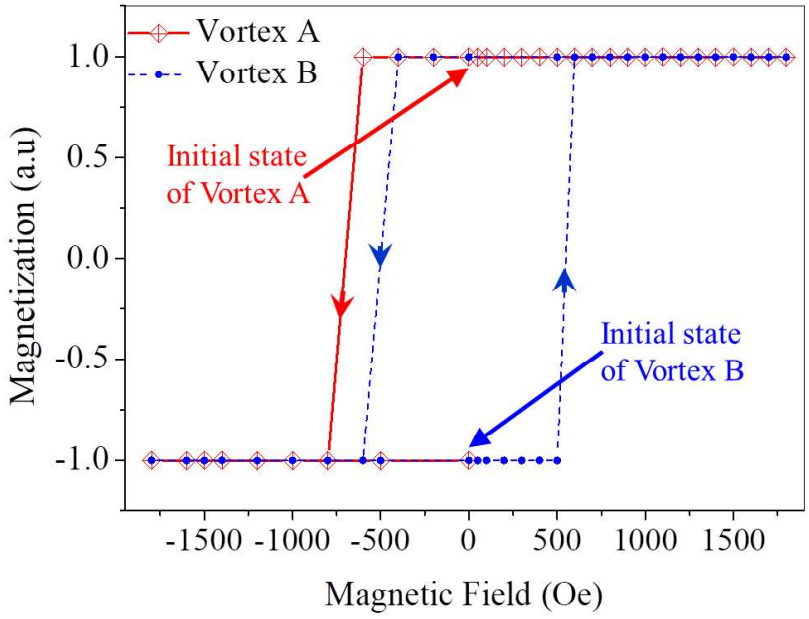

Figure 6.13: Micro-magnetization loop for two vortex domains with different initial vortex directions in the demagnetized condition.

6.3 COMPARISON STUDY OF MARTERIALS

A comparison of microstructure and magnetic properties of the three materials studied in the dissertation viz. polycrystalline pure iron (Chapter 4), duplex stainless steel (Chapter 5) and cold worked AUSS (Chapter 6) is made in Fig. 6.13.

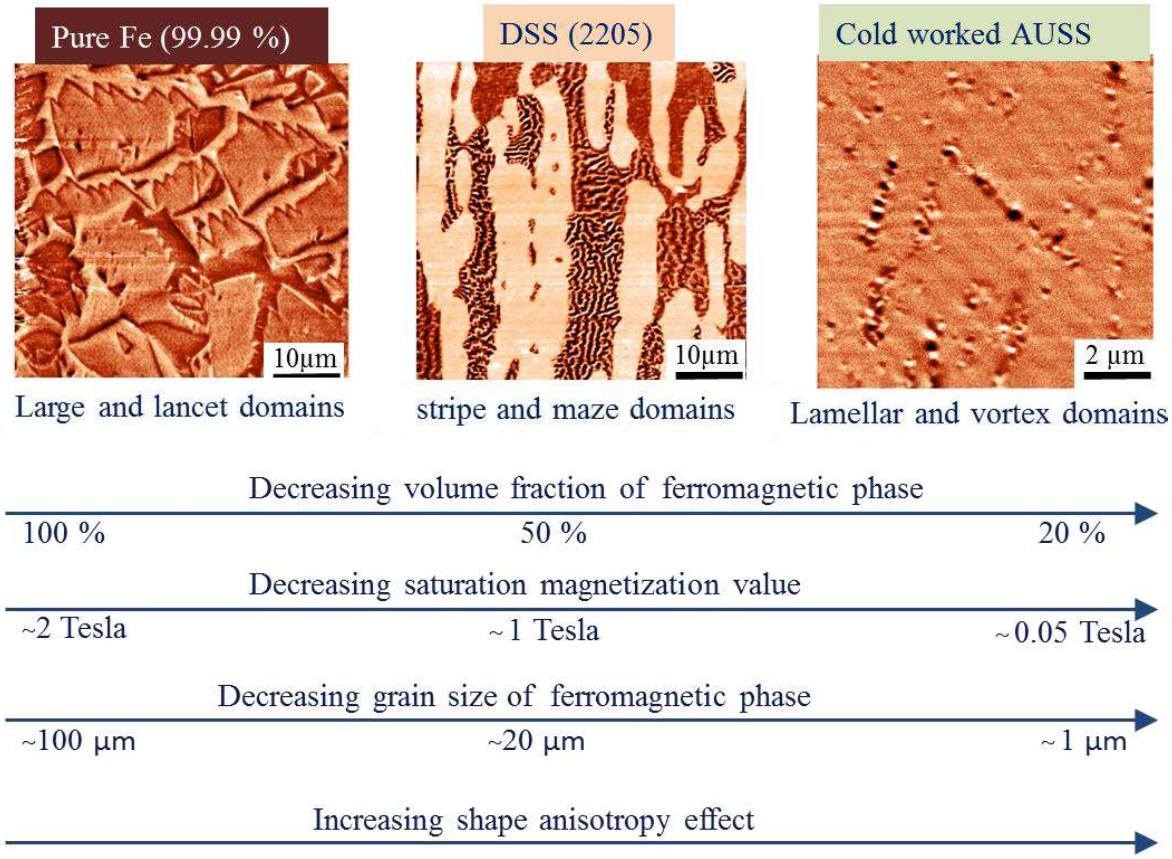

Figure 6.14: Comparison of magnetic properties of the materials studied in the Thesis.

The amount of ferromagnetic phase decreased from 100% in the polycrystalline pure iron to 50% and 20% in the duplex stainless steel and cold worked AUSS, respectively. The reduction in the amount of ferromagnetic phase is clearly evident in the saturation magnetization values of 2 T, 1 T and 0.05 T, respectively. A proportional 50 % lower value of saturation magnetization for 50 % reduction in ferromagnetic phase is observed for DSS sample as compared to the polycrystalline iron sample. However, disproportionately lower value of magnetization (0.05 T) in the cold worked AUSS may

be attributed to the discontinuous distribution of ferromagnetic martensite phase in the paramagnetic austenitic matrix.

The magnetic domains observed in the polycrystalline iron specimen are mostly in-plane magnetized, except for the domains in the {111} planes. This may be attributed to the alignment of reasonably larger size domains in the surface to reduce the stray filed energy and low perpendicular anisotropy in iron. In the case of DSS sample, the domains are mostly magnetized in the out-of-plane direction due to the high perpendicular anisotropy. In both iron and DSS specimens, the domain structures are primarily influenced by the crystallographic orientations, *i.e*. crystallography anisotropy govern the domain structure. However, in the case of cold worked 304 SS, both in-plane and out-of-plane magnetization are observed for the precipitates with the same crystallographic orientations but different sizes indicating strong effect of size or the shape anisotropy.

6.4 CONCLUSIONS

Magnetic domain structures and their field dependent domain dynamics in fine martensitic precipitates of cold worked 304 AUSS are studied in the present chapter using MFM. MFM imaging could clearly identify the martensitic precipitates in the austenitic matrix due to the presence of magnetic domains leading to phase contrast in MFM imaging. The average area fraction of the martensite phase estimated by MFM imaging at different locations over the sample is found to be in good agreement with that obtained by X-ray diffraction technique. Both in-plane and out-of-plane magnetized domains have been observed for the precipitates with the same crystallographic orientations indicating strong effect of size or the shape anisotropy. Micro-magnetization loops of two vortex domains with different initial orientations have also been studied. The study demonstrated that the shape anisotropy influences the magnetic domain structure in fine

isolated ferromagnetic phases, whereas the magnetocrystalline anisotropy governs the domain structure and its orientation in polycrystalline ferromagnetic materials with larger grains.

SUMMARY AND FUTURE DIRECTIONS

7

7.1 SUMMARY

- The present study demonstrates the applicability of MFM in combination with EBSD technique to study the influence of magneto crystalline anisotropy on the magnetic microstructure and field dependent domain wall dynamics on the surface of polycrystalline iron and iron based alloy steels.

- Three specimens having ferromagnetic phases of different size, shape and volume fraction viz polycrystalline pure iron, duplex stainless steel and cold worked AISI type 304 austenitic stainless steel are investigated.

- Domains with in-plane magnetization are observed on the surface of the polycrystalline iron specimen with at least one easy axis of magnetization lying on the surface. However, irrespective of the grain orientation, ferrite phase in DSS exhibited out of plane magnetization of stripe domains and the martensite phase in AUSS exhibited in-plane or out-of-plane magnetization depending upon its size and shape.

- The MFM phase contrast is higher for out of plane magnetized domains. In DSS, the width of the stripe magnetic domain increases linearly and the MFM phase contrast decreases almost linearly with increasing deviation of the grain surface normal from the easy axis of magnetization.

- MFM study in presence of external magnetic field provided clear visualization of various micro-magnetization phenomena such as reversible and irreversible domain wall movements, expansion and contraction of domains, Barkhausen jump, generation of a spike domain, bowing of a pinned domain wall, rearrangement in maze/ stripe type domains and rotation of vortex type domains.
- Domain wall energy density is estimated in pure iron from field dependent bowing of a surface domain wall pinned at two points.
- DSS containing equal proportion of ferromagnetic and paramagnetic phases, provided the effect of grain boundaries on micro-magnetization phenomena.
- The study on cold worked AUSS provided micro-magnetization characterization on naturally occurring micro / nano sized ferromagnetic structures in paramagnetic matrix.
- Local minor magnetic hysteresis loops are generated using suitable parameters from MFM measurements.
- The study demonstrates that the shape anisotropy effects become more prominent as compared to the crystalline anisotropy with decreasing size of the ferromagnetic phase.

7.2 FUTURE DIRECTIONS

- Micro-magnetic simulation of bulk polycrystalline ferromagnetic materials will complement the MFM studies performed in the thesis for better understanding of the bulk magnetic properties.
- A tip with known magnetic moment and resonance frequency based MFM imaging will provide better quantitative information about magnetic domains.

- Study with a volumetric magnetic domain visualization technique in presence of external magnetic field will provide a better understanding of correlation between surface and bulk domain structure and dynamics.
- The combination study of MFM with magnetic optical Kerr microscopy on bulk structural magnetic material could be useful to investigate temperature effect on the domain dynamics.

LIST OF ABBREVIATIONS AND SYMBOLS

AFM	Atomic Force Microscopy
AGM	Alternating Gradient Magnetometer
AUSS	Austenitic Stainless Steel
DSS	Duplex Stainless Steel
EBSD	Electron Backscatter Diffraction
IPF	Inverse Pole Figure
MFM	Magnetic Force Microscopy
MOKE	Magneto-Optical Kerr Microscopy
LTEM	Lorentz Transmission Electron Microscopy
SEM	Scanning Electron Microscopy
SEMPA	Scanning Electron Microscopy with Polarization Analysis
SHPM	Scanning Hall Probe Microscopy
SIM	Strain Induced Martensite
SP-STM	Spin Polarized Scanning Tunneling Microscopy
SPLEEM	Spin Polarized Low Energy Electron Microscopy
SQUID	Superconducting Quantum Interference Device
XMCD	X-Ray Magnetic Circular Dichroism
e	Electron charge
E_{aniso}	Magnetocrystalline anisotropy energy
E_{ex}	Exchange energy
E_{me}	Magnetostriction energy
E_{ms}	Magnetostatic energy
E_{wall}	Domain wall energy

f_0	Cantilever resonance frequency
H_d	Demagnetization Field
J_{ij}	Exchange energy constant
k	Cantilever spring constant
m_e	Mass of electron
M_s	Saturation magnetization
N_d	Demagnetization Factor
Q	Cantilever quality factor
μ_0	Permeability of free space

REFERENCES

1. B.D. Cullity, *Introduction to Magnetic Materials*. 1972, London: Addison Wesley.
2. C.-W. Chen, *Magnetism and metallurgy of soft magnetic materials*. 1977: North-Holland Publishing Company.
3. R.M. Bozorth, *Magnetic domain patterns.* . J. Phys. Radium,, 1951, . **12** (3): p. 308-321.
4. C. Kittel and J.K. Galt, *Ferromagnetic Domain Theory*, in *Solid State Physics*, S. Frederick and T. David, Editors. 1956, Academic Press. p. 437-564.
5. D.C. Jiles and D.L. Atherton, *Theory of ferromagnetic hysteresis.* J. Magn. Magn. Mater., 1986. **61**(1–2): p. 48-60.
6. G.Y. Chin and J.H. Wernick, *Soft magnetic metallic materials*, in *Handbook of Magnetic Materials* E.P. Wolhfarth, Editor. 1980, North-Holland Publishing company.
7. P. Langevin, *Magnétisme et théorie des électrons* Ann. Chim. Phys., 1905. **5**(8): p. 70-127.
8. P. Weiss, *L'hypothèse du champ moléculaire et la propriété ferromagnétique.* J. Phys. Theor. Appl., 1907. **6**(1): p. 661-690.
9. W. Heisenberg, *Zur Theorie des Ferromagnetismus.* Z. Phys., 1928. **49**(9): p. 619-636.
10. H. Barkhausen, *Zwei mit Hilfe der neuen Verstärker entdeckte Erscheinungen.* Phys. Z, 1919. **20**: p. 401.
11. I. Langmuir and K.J. Sixtus, *Regions of Reversed Magnetization in Strained Wires.* Phys. Rev., 1931. **38**(11): p. 2072-2072.
12. K.J. Sixtus and L. Tonks, *Further Experiments on the Propagation of Large Barkhausen Discontinuities.* Phys. Rev., 1932. **39**(2): p. 357-358.
13. K.J. Sixtus and L. Tonks, *Propagation of Large Barkhausen Discontinuities. II.* Phys. Rev., 1932. **42**(3): p. 419-435.
14. F. Bloch, *Zur Theorie des Austauschproblems und der Remanenzerscheinung der Ferromagnetika.* Z. Phys., 1932. **74**(5): p. 295-335.
15. J. Frenkel and J. Doefman, *Spontaneous and induced magnetisation in ferromagnetic bodies.* Nature, 1930. **126**(3173): p. 274.
16. R. Becker, *Zur Theorie der Magnetisierungskurve.* Z. Phys., 1930. **62**(3): p. 253-269.
17. W. Heisenberg, *Zur Theorie der Magnetostriktion und der Magnetisierungskurve.* Z. Phys., 1931. **69**(5): p. 287-297.
18. H.J. Williams, *Magnetic Properties of Single Crystals of Silicon Iron.* Phys. Rev., 1937. **52**(7): p. 747-751.
19. F. Bitter, *Experiments on the Nature of Ferromagnetism.* Phys. Rev., 1932. **41**(4): p. 507-515.
20. L.D.L. Landau, E, *On the theory of the dispersion of magnetic permeability in ferromagnetic bodies.* Phys. Z. Sowjet, 1935. **8**: p. 153.
21. D.J. Craik and R.S. Tebble, *Magnetic domains.* Rep. Prog. Phys., 1961. **24**(1): p. 116.
22. C. Kittel, *Theory of the Structure of Ferromagnetic Domains in Films and Small Particles.* Phys. Rev., 1946. **70**(11-12): p. 965-971.
23. C. Kittel, *Theory of the Formation of Powder Patterns on Ferromagnetic Crystals.* Phys. Rev., 1949. **76**(10): p. 1527-1527.
24. C. Kittel, *Physical Theory of Ferromagnetic Domains.* Rev. Mod. Phys., 1949. **21**(4): p. 541-583.
25. A. Hubert and R. Schäfer, *Magnetic domains - The analysis of magnetic microstructures*. 1999, Berlin: springer.
26. L. Batista., *Examination of micro and nanostructures of magnetic and piezoelectric materials in relation to their macroscopic properties by dynamic scanning force microscopy techniques* in *Naturwissenschaftlich-Technischen Fakultät III*. 2014, Universität des Saarlandes: Saarbrücken.
27. R.F.L. Evans, U. Atxitia and R.W. Chantrell, *Quantitative simulation of temperature-dependent magnetization dynamics and equilibrium properties of elemental ferromagnets.* Physical Review B, 2015. **91**(14): p. 144425.

28. A. AHARONI, *lntroduction to the Theory of Ferromagnetism*. Second ed. Vol. 109. 2000, USA: Oxford University Press.
29. W. Szmaja, *Recent Developments in the Imaging of Magnetic Domains*, in *Advances in Imaging and Electron Physics*, H. Peter, Editor. 2006, Elsevier. p. 175-256.
30. K. Honda, S. Kaya and Y. Masuyama, *On the Magnetic Properties of Single Crystals of Iron.* Nature, 1926. **117**: p. 753.
31. L. Néel, *Les lois de l'aimantation et de la subdivision en domaines élémentaires d'un monocristal de fer.* J. Phys. Radium, 1944. **5**(11): p. 241-251.
32. C.T. Hsieh, J.Q. Liu and J.T. Lue, *Magnetic force microscopy studies of domain walls in nickel and cobalt films.* Appl. Surf. Sci., 2005. **252**(5): p. 1899-1909.
33. D.C. Jiles, *Introduction to Magnetism and Magnetic Materials*. 1998: CRC Press.
34. G. van der Laan, K. Chesnel, M. Belakhovsky, A. Marty, F. Livet, S.P. Collins, E. Dudzik, A. Haznar and J.P. Attané, *Magnetic anisotropy of aligned magnetic stripe domains in FePd studied by soft x-ray resonant magnetic scattering, magnetic force microscopy and micromagnetic modeling.* Superlattices Microstruct., 2003. **34**(1–2): p. 107-126.
35. J. Miltat, *Domains and domain walls in soft magnetic materials, mostly* in *Applied Magnetism, NATO ASI Series(E: Applied Sciences)*, Richard Gerber, C. D. Wright, and G. Asti, Editors. 1994, Springer: Dordrecht.
36. A.W. Pacyna and K. Ruebenbauer, *General theory of a vibrating magnetometer with extended coils.* Journal of Physics E: Scientific Instruments, 1984. **17**(2): p. 141.
37. K. Gramm, L. Lundgren and O. Beckman, *SQUID Magnetometer for Mangetization Measurements.* Phys. Scr., 1976. **13**(2): p. 93.
38. P.J. Flanders, *An alternating-gradient magnetometer (invited).* J. Appl. Phys., 1988. **63**(8): p. 3940-3945.
39. A. Barman, T. Kimura, Y. Otani, Y. Fukuma, K. Akahane and S. Meguro, *Benchtop time-resolved magneto-optical Kerr magnetometer.* Rev. Sci. Instrum., 2008. **79**(12): p. 123905.
40. M.R. Freeman and B.C. Choi, *Advances in Magnetic Microscopy.* Science, 2001. **294**(5546): p. 1484.
41. M. Jeffrey, *Progress in magnetic domain observation by advanced magneto-optical microscopy.* J. Phys. D: Appl. Phys., 2015. **48**(33): p. 333001.
42. W. Kuch, *Magnetic Imaging*, in *Magnetism: A Synchrotron Radiation Approach*, E. Beaurepaire, et al., Editors. 2006, Springer Berlin Heidelberg: Berlin, Heidelberg. p. 275-320.
43. R.J. Celotta, J. Unguris, M.H. Kelley and D.T. Pierce, *Techniques to Measure Magnetic Domain Structures*, in *Characterization of Materials*. 2002, John Wiley & Sons, Inc.
44. W.L. June and M.S. Justin, *Magnetic nanostructures for advanced technologies: fabrication, metrology and challenges.* J. Phys. D: Appl. Phys., 2011. **44**(30): p. 303001.
45. H.J. Williams, *Direction of Domain Magnetization in Powder Patterns.* Phys. Rev., 1947. **71**(9): p. 646-647.
46. L.D. Livingston, *Magnetic domains in cobalt and iron borides.* J. Appl. Phys., 1981. **52**(3): p. 2506-2508.
47. F. Bitter, *On Inhomogeneities in the Magnetization of Ferromagnetic Materials.* Phys. Rev., 1931. **38**(10): p. 1903-1905.
48. W. Szmaja, *Improvements in Domain Study with the Conventional Bitter Method by Digital Image Processing System.* physica status solidi (a), 2002. **194**(1): p. 315-330.
49. D.J. Craik, *The magnetic domain structures of small crystals.* Contemporary Physics, 1970. **11**(1): p. 65-97.
50. D.E. Newbury, D.C. Joy, P. Echlin, C.E. Fiori and J.I. Goldstein, *Magnetic Contrast in the SEM*, in *Advanced Scanning Electron Microscopy and X-Ray Microanalysis*. 1986, Springer US: Boston, MA. p. 147-179.
51. L. Reimer, *Special Techniques in SEM*, in *Scanning Electron Microscopy: Physics of Image Formation and Microanalysis*. 1998, Springer Berlin Heidelberg: Berlin, Heidelberg. p. 289-328.

52. M.R. Scheinfein, J. Unguris, M.H. Kelley, D.T. Pierce and R.J. Celotta, *Scanning electron microscopy with polarization analysis (SEMPA).* Rev. Sci. Instrum., 1990. **61**(10): p. 2501-2527.
53. H.P. Oepen, G. Steierl and J. Kirschner, *Scanning electron microscope with polarization analysis: Micromagnetic structures in ultrathin films.* Journal of Vacuum Science & Technology B: Microelectronics and Nanometer Structures Processing, Measurement, and Phenomena, 2002. **20**(6): p. 2535-2538.
54. K.J. Kirk, J.N. Chapman and C.D.W. Wilkinson, *Lorentz microscopy of small magnetic structures (invited).* J. Appl. Phys., 1999. **85**(8): p. 5237-5242.
55. A. Masseboeuf, C. Gatel, P. Bayle-Guillemaud, Y. Lamy and B. Viala, *The use of Lorentz microscopy for the determination of magnetic reversal mechanism of exchange-biased Co30Fe70/NiMn bilayer.* J. Magn. Magn. Mater., 2009. **321**(19): p. 3080-3083.
56. L.A. Rodríguez, C. Magén, E. Snoeck, C. Gatel, L. Marín, L. Serrano-Ramón, J.L. Prieto, M. Muñoz, P.A. Algarabel, L. Morellon, J.M. De Teresa, and M.R. Ibarra, *Quantitative in situ magnetization reversal studies in Lorentz microscopy and electron holography.* Ultramicroscopy, 2013. **134**: p. 144-154.
57. A. Rogalev, F. Wilhelm, N. Jaouen, J. Goulon and J.-P. Kappler, *X-ray Magnetic Circular Dichroism: Historical Perspective and Recent Highlights*, in *Magnetism: A Synchrotron Radiation Approach*, E. Beaurepaire, et al., Editors. 2006, Springer Berlin Heidelberg: Berlin, Heidelberg. p. 71-93.
58. G. van der Laan and A.I. Figueroa, *X-ray magnetic circular dichroism—A versatile tool to study magnetism.* Coord. Chem. Rev., 2014. **277-278**: p. 95-129.
59. C. Grünzweig, C. David, O. Bunk, J. Kohlbrecher, E. Lehmann, Y.W. Lai, R. Schäfer, S. Roth, P. Lejcek, J. Kopecek, and F. Pfeiffer, *Visualizing the propagation of volume magnetization in bulk ferromagnetic materials by neutron grating interferometry (invited).* J. Appl. Phys., 2010. **107**(9): p. 09D308.
60. I. Manke, N. Kardjilov, R. Schäfer, A. Hilger, M. Strobl, M. Dawson, C. Grünzweig, G. Behr, M. Hentschel, C. David, A. Kupsch, A. Lange, and J. Banhart, *Three-dimensional imaging of magnetic domains.* Nature Communications, 2010. **1**: p. 125.
61. G. Shaw, R.B.G. Kramer, N.M. Dempsey and K. Hasselbach, *A scanning Hall probe microscope for high resolution, large area, variable height magnetic field imaging.* Rev. Sci. Instrum., 2016. **87**(11): p. 113702.
62. V.V. Khotkevych, M.V. Milošević and S.J. Bending, *A scanning Hall probe microscope for high resolution magnetic imaging down to 300 mK.* Rev. Sci. Instrum., 2008. **79**(12): p. 123708.
63. M.R. Koblischka and U. Hartmann, *Recent advances in magnetic force microscopy.* Ultramicroscopy, 2003. **97**(1–4): p. 103-112.
64. F.A. Ferri, M.A. Pereira-da-Silva and E. Marega Jr, *Magnetic Force Microscopy: Basic Principles and Applications, Atomic Force Microscopy - Imaging, Measuring and Manipulating Surfaces at the Atomic Scale*, in *Dr. Victor Bellitto (Ed.),InTech,*. 2012.
65. G. Binnig, H. Rohrer, C. Gerber and E. Weibel, *Surface Studies by Scanning Tunneling Microscopy.* Phys. Rev. Lett., 1982. **49**(1): p. 57-61.
66. G. Binnig, C.F. Quate and C. Gerber, *Atomic Force Microscope.* Phys. Rev. Lett., 1986. **56**(9): p. 930-933.
67. M.K. Phani, *Quantitative mapping of elastic properties in nickel and titanium base alloys at nanoscale using atomic force acoustic microscopy* in *Indira Gandhi Centre for Atomic Research*. 2015, HOMI BHABHA NATIONAL INSTITUTE Kalpakkam.
68. X. Li, W. Lu, Y. Song, Y. Wang, A. Chen, B. Yan, S. Yoshimura and H. Saito, *Quantitatively probing the magnetic behavior of individual nanoparticles by an AC field-modulated magnetic force microscopy.* Scientific Reports, 2016. **6**: p. 22467.
69. R.D. Gomez, E.R. Burke and I.D. Mayergoyz, *Magnetic imaging in the presence of external fields: Technique and applications (invited).* J. Appl. Phys., 1996. **79**(8): p. 6441-6446.
70. P. Grütter, D. Rugar and H.J. Mamin, *Magnetic force microscopy of magnetic materials.* Ultramicroscopy, 1992. **47**(4): p. 393-399.

71. A. Schwarz, M. Liebmann, U. Kaiser, R. Wiesendanger, T.W. Noh and D.W. Kim, *Visualization of the Barkhausen Effect by Magnetic Force Microscopy.* Phys. Rev. Lett., 2004. **92**(7): p. 077206.
72. G. Cordova, B. Lee and Z. Leonenko, *Magnetic Force Microscopy for Nanoparticle Characterization.* NanoWorld J, 2016. **2**(1): p. 10-14.
73. M. Jaafar, R. Yanes, A. Asenjo, O. Chubykalo-Fesenko, M. Vázquez, E.M. González and J.L. Vicent, *Field induced vortex dynamics in magnetic Ni nanotriangles.* Nanotechnology, 2008. **19**(28): p. 285717.
74. M. Jaafar, L. Serrano-Ramón, O. Iglesias-Freire, A. Fernández-Pacheco, M.R. Ibarra, J.M. De Teresa and A. Asenjo, *Hysteresis loops of individual Co nanostripes measured by magnetic force microscopy.* Nanoscale Research Letters, 2011. **6**(1): p. 407.
75. T.G. Sorop, C. Untiedt, F. Luis, M. Kröll, M. Rasa and L.J. de Jongh, *Magnetization reversal of ferromagnetic nanowires studied by Magnetic Force Microscopy.* Phys. Rev. B, 2003. **67**.
76. L. Yue and S.-H. Liou, *Magnetic Force Microscopy Studies of Magnetic Features and Nanostructures*, in *Scanning Probe Microscopy in Nanoscience and Nanotechnology 2*, B. Bhushan, Editor. 2011, Springer Berlin Heidelberg: Berlin, Heidelberg. p. 287-319.
77. D. Passeri, C. Dong, M. Reggente, L. Angeloni, M. Barteri, F.A. Scaramuzzo, F. De Angelis, F. Marinelli, F. Antonelli, F. Rinaldi, C. Marianecci, M. Carafa, A. Sorbo, D. Sordi, I.W.C.E. Arends, and M. Rossi, *Magnetic force microscopy.* Biomatter, 2014. **4**(1): p. e29507.
78. Y. Martin and H.K. Wickramasinghe, *Magnetic imaging by ''force microscopy'' with 1000 Å resolution.* Appl. Phys. Lett., 1987. **50**(20): p. 1455-1457.
79. H.J. Hug, B. Stiefel, P.J.A. van Schendel, A. Moser, R. Hofer, S. Martin, H.J. Güntherodt, S. Porthun, L. Abelmann, J.C. Lodder, G. Bochi, and R.C. O'Handley, *Quantitative magnetic force microscopy on perpendicularly magnetized samples.* J. Appl. Phys., 1998. **83**(11): p. 5609-5620.
80. M. Jaafar, A. Asenjo and M. VÁzquez, *Calibration of Coercive and Stray Fields of Commercial Magnetic Force Microscope Probes.* IEEE Transactions on Nanotechnology, 2008. **7**(3): p. 245-250.
81. R. Shaar and J.M. Feinberg, *Rock magnetic properties of dendrites: Insights from MFM imaging and implications for paleomagnetic studies.* Geochem. Geophys. Geosyst., 2013. **14**(2): p. 407-421.
82. S.J. May, A.J. Blattner, D.P. Eam and B.W. Wessels, *Direct observation of room temperature magnetism in (In,Mn)As thin films by magnetic force microscopy.* Appl. Surf. Sci., 2006. **252**(10): p. 3509-3513.
83. A. Maziewski, J. Fassbender, J. Kisielewski, M. Kisielewski, Z. Kurant, P. Mazalski, F. Stobiecki, A. Stupakiewicz, I. Sveklo, M. Tekielak, A. Wawro, and V. Zablotskii, *Magnetization states and magnetization processes in nanostructures: From a single layer to multilayers.* physica status solidi (a), 2014. **211**(5): p. 1005-1018.
84. W. Szmaja, *Investigations of the domain structure of anisotropic sintered Nd–Fe–B-based permanent magnets.* J. Magn. Magn. Mater., 2006. **301**(2): p. 546-561.
85. M.M. Yazid, S.H. Olsen and G.J. Atkinson, *MFM Study of a Sintered Nd–Fe–B Magnet: Analyzing Domain Structure and Measuring Defect Size in 3-D View.* IEEE Trans. Magn., 2016. **52**(6): p. 1-10.
86. A. Asenjo, D. García, J.M. García, C. Prados and M. Vázquez, *Magnetic force microscopy study of dense stripe domains in Fe-B/Co-Si-B multilayers and the evolution under an external applied field.* Physical Review B, 2000. **62**(10): p. 6538-6544.
87. A. de Lozanne, *Application of magnetic force microscopy in nanomaterials characterization.* Microsc. Res. Tech., 2006. **69**(7): p. 550-562.
88. J. Zabaleta, M. Jaafar, A. Asenjo, S. Agramunt-Puig, N. Del-Valle, C. Navau, A. Sanchez, T. Puig, X. Obradors and N. Mestres, *Magnetic vortex evolution in self-assembled La0.7Sr0.3MnO3 nanoislands under in-plane magnetic field.* APL Materials, 2014. **2**(7): p. 076111.

89. M. Jaafar, J. Gomez-Herrero, A. Gil, P. Ares, M. Vazquez and A. Asenjo, *Variable field magnetic force microscopy.* Ultramicroscopy, 2009. **109**.
90. A. Asenjo, M. Jafaar, D. Navas and M. Vázquez, *Quantitative Magnetic Force Microscopy analysis of the magnetization process in nanowire arrays.* J. Appl. Phys., 2006. **100**.
91. A. Alekseev, A. Popkov, A. Shubin, F. Pudonin and N. Djuzhev, *Effect of horizontal magnetization reversal of the tips on magnetic force microscopy images.* Ultramicroscopy, 2014. **136**: p. 91-95.
92. J.B. Wedding, M. Li and G.C. Wang, *Magnetization reversal of a thin polycrystalline cobalt film measured by the magneto-optic Kerr effect (MOKE) technique and field-dependent magnetic force microscopy.* J. Magn. Magn. Mater., 1999. **204**(1–2): p. 79-89.
93. H. Zhou, Z. Wang, Y. Hou and Q. Lu, *A compact high field magnetic force microscope.* Ultramicroscopy, 2014. **147**: p. 133-136.
94. J. Ramírez-Salgado, M.A. Domínguez-Aguilar, B. Castro-Domínguez, P. Hernández-Hernández and R.C. Newman, *Detection of secondary phases in duplex stainless steel by magnetic force microscopy and scanning Kelvin probe force microscopy.* Mater. Charact., 2013. **86**: p. 250-262.
95. S.M. Gheno, F.S. Santos and S.E. Kuri, *Probing the duplex stainless steel phases via magnetic force microscopy.* J. Appl. Phys., 2008. **103**(5): p. 053906.
96. N. Sathirachinda, R. Gubner, J. Pan and U. Kivisäkk, *Characterization of phases in duplex stainless steel by magnetic force microscopy/scanning Kelvin probe force microscopy.* Electrochem. Solid-State Lett., 2008. **11**(7): p. C41-C45.
97. A. Dias and M.S. Andrade, *Atomic force and magnetic force microscopies applied to duplex stainless steels.* Appl. Surf. Sci., 2000. **161**(1–2): p. 109-114.
98. L. Batista, U. Rabe, I. Altpeter, S. Hirsekorn and G. Dobmann, *On the mechanism of nondestructive evaluation of cementite content in steels using a combination of magnetic Barkhausen noise and magnetic force microscopy techniques.* J. Magn. Magn. Mater., 2014. **354**: p. 248-256.
99. G.V.K. Kishore, A. Kumar, G. Chakraborty, S.K. Albert, B.P.C. Rao, A.K. Bhaduri and T. Jayakumar, *Study of magnetism in Ni–Cr hardface alloy deposit on 316LN stainless steel using magnetic force microscopy.* J. Magn. Magn. Mater., 2015. **385**: p. 112-118.
100. K. Wieczerzak, A. Żywczak, J. Kanak and P. Bała, *Magnetic detection of chromium depleted regions in metastable Fe-Cr-C alloy.* Mater. Charact., 2017. **132**: p. 293-302.
101. A.D. Warren, R.L. Harniman, A.M. Collins, S.A. Davis, C.M. Younes, P.E.J. Flewitt and T.B. Scott, *Comparison between magnetic force microscopy and electron back-scatter diffraction for ferrite quantification in type 321 stainless steel.* Ultramicroscopy, 2015. **148**: p. 1-9.
102. M. Bramowicz and S. Kulesza, *A Magnetic Force Microscopy Study of Magnetic Domain Structure in Maraging steel* Solid State Phenomena 2011. **203-204**: p. 315- 318.
103. S. Takaya, T. Suzuki, Y. Matsumoto, K. Demachi and M. Uesaka, *Estimation of stress corrosion cracking sensitivity of type 304 stainless steel by magnetic force microscope.* J. Nucl. Mater., 2004. **327**(1): p. 19-26.
104. A. Miller, Y. Estrin and X.Z. Hu, *Magnetic force microscopy of fatigue crack tip region in a 316L austenitic stainless steel.* Scripta Mater., 2002. **47**(7): p. 441-446.
105. L. Batista, U. Rabe and S. Hirsekorn, *Magnetic micro- and nanostructures of unalloyed steels: Domain wall interactions with cementite precipitates observed by MFM.* NDT & E International, 2013. **57**: p. 58-68.
106. G.E. Fish, *Soft magnetic materials.* Proc. IEEE, 1990. **78**(6): p. 947-972.
107. H.J. Williams, R.M. Bozorth and W. Shockley, *Magnetic Domain Patterns on Single Crystals of Silicon Iron.* Phys. Rev., 1949. **75**(1): p. 155-178.
108. D. Küppers, J. Kranz and A. Hubert, *Coercivity and Domain Structure of Silicon-Iron Single Crystals.* J. Appl. Phys., 1968. **39**(2): p. 608-609.
109. K. Kawahara, Y. Yagyu, S. Tsurekawa and T. Watanabe, *Observations of Interaction Between Magnetic Domain Wall and Grain Boundaries in Fe-3wt%Si Alloy by Kerr Microscopy.* MRS Proceedings, 1999. **586**.

110. M. Gallaugher, N. Brodusch, R. Gauvin and R.R. Chromik, *Magnetic domain structure and crystallographic orientation of electrical steels revealed by a forescatter detector and electron backscatter diffraction.* Ultramicroscopy, 2014. **142**: p. 40-49.
111. S. Shin, R. Schafer and B.C.D. Cooman, *Grain Boundary Penetration by Lancet Domains in Fe-3%Si Grain-Oriented Steel.* IEEE Trans. Magn., 2010. **46**(9): p. 3574-3581.
112. S. Li, X. Ren and H. Hou, *The effect of thermal cycling in superplastic diffusion bonding of 2205 duplex stainless steel.* Materials & Design, 2015. **86**: p. 582-586.
113. P. Maj, B. Adamczyk-Cieślak, J. Mizera, W. Pachla and K.J. Kurzydłowski, *Microstructure and mechanical properties of duplex stainless steel subjected to hydrostatic extrusion.* Mater. Charact., 2014. **93**: p. 110-118.
114. K. Chandra, R. Singhal, V. Kain and V.S. Raja, *Low temperature embrittlement of duplex stainless steel: Correlation between mechanical and electrochemical behavior.* Materials Science and Engineering: A, 2010. **527**(16–17): p. 3904-3912.
115. S.S.M. Tavares, P.D.S. Pedrosa, J.R. Teodósio, M.R. da Silva, J.M. Neto and S. Pairis, *Magnetic properties of the UNS S39205 duplex stainless steel.* J. Alloys Compd., 2003. **351**(1–2): p. 283-288.
116. P.G. Normando, E.P. Moura, J.A. Souza, S.S.M. Tavares and L.R. Padovese, *Ultrasound, eddy current and magnetic Barkhausen noise as tools for sigma phase detection on a UNS S31803 duplex stainless steel.* Materials Science and Engineering: A, 2010. **527**(12): p. 2886-2891.
117. I. Mészáros and P.J. Szabó, *Complex magnetic and microstructural investigation of duplex stainless steel.* NDT & E International, 2005. **38**(7): p. 517-521.
118. C. Camerini, R. Sacramento, M.C. Areiza, A. Rocha, R. Santos, J.M. Rebello and G. Pereira, *Eddy current techniques for super duplex stainless steel characterization.* J. Magn. Magn. Mater., 2015. **388**: p. 96-100.
119. G. Fourlaris, M.G. Maylin and T. Gladman, *Magnetic Domain Imaging and Mechanical/Magnetic Property Characterisation of a 2507 Type Duplex Austenitic-Ferritic Stainless Steel*, in *Materials Science Forum* H. Hänninen, S. Hertzman, and J. Romu, Editors. 1999. p. 823-828.
120. K.R. Gadelrab, G. Li, M. Chiesa and T. Souier, *Local characterization of austenite and ferrite phases in duplex stainless steel using MFM and nanoindentation.* J. Mater. Res., 2012. **27**(12): p. 1573-1579.
121. L.Q. Guo, M. Li, X.L. Shi, Y. Yan, X.Y. Li and L.J. Qiao, *Effect of annealing temperature on the corrosion behavior of duplex stainless steel studied by in situ techniques.* Corros. Sci., 2011. **53**(11): p. 3733-3741.
122. A.D. Warren, R.L. Harniman, Z. Guo, C.M. Younes, P.E.J. Flewitt and T.B. Scott, *Quantification of sigma-phase evolution in thermally aged 2205 duplex stainless steel.* J. Mater. Sci., 2016. **51**(2): p. 694-707.
123. L.Q. Guo, X.M. Zhao, M. Li, W.J. Zhang, Y. Bai and L.J. Qiao, *Annealing effects on the microstructure and magnetic domain structures of duplex stainless steel studied by in situ technique.* Appl. Surf. Sci., 2012. **259**: p. 213-218.
124. K.H. Lo, *Magnetic domain characterisation of duplex stainless steel after different treatments.* Mater. Charact., 2012. **72**: p. 46-52.
125. B.H. Sencer, G.S. Was, M. Sagisaka, Y. Isobe, G.M. Bond and F.A. Garner, *Proton irradiation emulation of PWR neutron damage microstructures in solution annealed 304 and cold-worked 316 stainless steels.* J. Nucl. Mater., 2003. **323**(1): p. 18-28.
126. F. Baldenebro-Lopez, C. Gomez-Esparza, R. Corral-Higuera, S. Arredondo-Rea, M. Pellegrini-Cervantes, J. Ledezma-Sillas, R. Martinez-Sanchez and J. Herrera-Ramirez, *Influence of Size on the Microstructure and Mechanical Properties of an AISI 304L Stainless Steel—A Comparison between Bulk and Fibers.* Materials, 2015. **8**(2): p. 451.
127. A. Hedayati, A. Najafizadeh, A. Kermanpur and F. Forouzan, *The effect of cold rolling regime on microstructure and mechanical properties of AISI 304L stainless steel.* J. Mater. Process. Technol., 2010. **210**(8): p. 1017-1022.

128. T. Michler, K. Berreth, J. Naumann and E. Sattler, *Analysis of martensitic transformation in 304 type stainless steels tensile tested in high pressure hydrogen atmosphere by means of XRD and magnetic induction.* Int. J. Hydrogen Energy, 2012. **37**(4): p. 3567-3572.
129. M.L. Holzworth and M.R. Louthan, *Hydrogen-Induced Phase Transformations in Type 304L Stainless Steels.* CORROSION, 1968. **24**(4): p. 110-124.
130. T.C. Chen, S.T. Chen and L.W. Tsay, *The role of induced α'-martensite on the hydrogen-assisted fatigue crack growth of austenitic stainless steels.* Int. J. Hydrogen Energy, 2014. **39**(19): p. 10293-10302.
131. S.W. Yang and J.E. Spruiell, *Cold-worked state and annealing behaviour of austenitic stainless steel.* J. Mater. Sci., 1982. **17**(3): p. 677-690.
132. I.R. Souza Filho, M.J.R. Sandim, R. Cohen, L.C.C.M. Nagamine, J. Hoffmann, R.E. Bolmaro and H.R.Z. Sandim, *Effects of strain-induced martensite and its reversion on the magnetic properties of AISI 201 austenitic stainless steel.* J. Magn. Magn. Mater., 2016. **419**: p. 156-165.
133. M. Milad, N. Zreiba, F. Elhalouani and C. Baradai, *The effect of cold work on structure and properties of AISI 304 stainless steel.* J. Mater. Process. Technol., 2008. **203**(1–3): p. 80-85.
134. S.H. Lee, J.Y. Choi and W.J. Nam, *Hardening Behavior of a 304 Stainless Steel Containing Deformation-Induced Martensite during Static Strain Aging.* Materials transactions, 2009. **50**(4): p. 926-929.
135. J. Sort, A. Concustell, E. Menéndez, S. Suriñach, M.D. Baró, J. Farran and J. Nogués, *Selective generation of local ferromagnetism in austenitic stainless steel using nanoindentation.* Appl. Phys. Lett., 2006. **89**(3): p. 032509.
136. V.L. Mironov, *Fundamentals of Scanning Probe Microscopy* 2004, Nizhniy Novgorod NT-MDT
137. V.Y. Igor and M.T. Aleksandr, *Magnetic force microscopy.* Russian Chemical Reviews, 1999. **68**(3): p. 165.
138. H. Danan, A. Herr and A.J.P. Meyer, *New Determinations of the Saturation Magnetization of Nickel and Iron.* J. Appl. Phys., 1968. **39**(2): p. 669-670.
139. Oscar de Abril, María del Carmen Sánchez and C. Aroca, *The effect of the in-plane demagnetizing field on films with weak perpendicular magnetic anisotropy.* J. Appl. Phys., 2006. **100**(6): p. 063904.
140. A. John and Baldwin Jr, *A Method for the Measurement of Domain-Wall Energy Density in Thin Magnetic Films.* J. Appl. Phys., 1969. **40**(1): p. 432-433.
141. H. Sakamoto, M. Okada and M. Homma, *Theoretical analysis of Barkhausen noise in carbon steels.* IEEE Trans. Magn., 1987. **23**(5): p. 2236-2238.
142. S. Yamaura, Y. Furuya and T. Watanabe, *The effect of grain boundary microstructure on Barkhausen noise in ferromagnetic materials.* Acta Mater., 2001. **49**(15): p. 3019-3027.
143. M. ElMassalami, I. Palatnik-de-Sousa, M.C.L. Areiza, J.M.A. Rebello and A. Elzubair, *On the magnetic anisotropy of superduplex stainless steel.* J. Magn. Magn. Mater., 2011. **323**(18–19): p. 2403-2407.
144. L. Batista, U. Rabe and S. Hirsekorn, *Determination of the easy axes of small ferromagnetic precipitates in a bulk material by combined magnetic force microscopy and electron backscatter diffraction techniques.* Ultramicroscopy, 2014. **146**: p. 17-26.
145. D. Fofanov and I.S. Riedner, *Magnetic properties of stainless steels: applications, opportunities and new developments.*
146. R.W. Gregorutti, J.E. Grau, F. Sives, C.I.J.M.S. Elsner and Technology, *Mechanical, electrochemical and magnetic behaviour of duplex stainless steel for biomedical applications.* Mater. Sci. Technol., 2015. **31**(15): p. 1818-1824.
147. J. Abuthahir and A. Kumar, *Magnetic force microscopy studies in bulk polycrystalline iron.* J. Magn. Magn. Mater., 2018. **448**: p. 107-116.
148. J.H. Espina-Hernández, J.A. Pérez-Benítez, F. Caleyo, T. Baudin, A.L. Helbert and J.M. Hallen, *Barkhausen noise measurements give direct observation of magnetocrystalline anisotropy energy in ferromagnetic polycrystals.* J. Phys. D: Appl. Phys., 2013. **46**(39): p. 392001.

149. J.I. Martín, J. Nogués, K. Liu, J.L. Vicent and I.K. Schuller, *Ordered magnetic nanostructures: fabrication and properties.* J. Magn. Magn. Mater., 2003. **256**(1): p. 449-501.
150. A. Viswanath, B.P.C. Rao, S. Mahadevan, P. Parameswaran, T. Jayakumar and B. Raj, *Nondestructive assessment of tensile properties of cold worked AISI type 304 stainless steel using nonlinear ultrasonic technique.* J. Mater. Process. Technol., 2011. **211**(3): p. 538-544.
151. I. Mészáros and J. Prohászka, *Magnetic investigation of the effect of α'-martensite on the properties of austenitic stainless steel.* J. Mater. Process. Technol., 2005. **161**(1-2): p. 162-168.
152. K. Spencer, M. Véron, K. Yu-Zhang and J.D. Embury, *The strain induced martensite transformation in austenitic stainless steels: Part 1 – Influence of temperature and strain history.* Mater. Sci. Technol., 2009. **25**(1): p. 7-17.
153. J.A. Venables, *The martensite transformation in stainless steel.* Philos. Mag., 1962. **7**(73): p. 35-44.
154. G. Olson and M. Cohen, *A mechanism for the strain-induced nucleation of martensitic transformations.* Journal of the Less Common Metals, 1972. **28**(1): p. 107-118.
155. J. Huang, X. Ye and Z. Xu, *Effect of Cold Rolling on Microstructure and Mechanical Properties of AISI 301LN Metastable Austenitic Stainless Steels.* Journal of Iron and Steel Research, International, 2012. **19**(10): p. 59-63.
156. A.K. De, J.G. Speer, D.K. Matlock, D.C. Murdock, M.C. Mataya and R.J. Comstock, *Deformation-induced phase transformation and strain hardening in type 304 austenitic stainless steel.* Metallurgical and Materials Transactions A, 2006. **37**(6): p. 1875-1886.
157. C. Frandsen, S.L.S. Stipp, S.A. McEnroe, M.B. Madsen and J.M. Knudsen, *Magnetic domain structures and stray fields of individual elongated magnetite grains revealed by magnetic force microscopy (MFM).* Physics of the Earth and Planetary Interiors, 2004. **141**(2): p. 121-129.
158. Ó.I. Freire, *Advances in Magnetic Force Microscopy*, in *Departamento de Física de la Materia Condensada*. 2014, Universidad Autónoma de Madrid p. 176.
159. T. Okuno, K. Shigeto, T. Ono, K. Mibu and T. Shinjo, *MFM study of magnetic vortex cores in circular permalloy dots: behavior in external field.* J. Magn. Magn. Mater., 2002. **240**(1): p. 1-6.